# Strojniški vestnik

# Journal of Mechanical Engineering

no. 3
year 2017
volume 63

# Strojniški vestnik – Journal of Mechanical Engineering (SV-JME)

**Aim and Scope**
The international journal publishes original and (mini)review articles covering the concepts of materials science, mechanics, kinematics, thermodynamics, energy and environment, mechatronics and robotics, fluid mechanics, tribology, cybernetics, industrial engineering and structural analysis.
The journal follows new trends and progress proven practice in the mechanical engineering and also in the closely related sciences as are electrical, civil and process engineering, medicine, microbiology, ecology, agriculture, transport systems, aviation, and others, thus creating a unique forum for interdisciplinary or multidisciplinary dialogue.
The international conferences selected papers are welcome for publishing as a special issue of SV-JME with invited co-editor(s).



**Editorial Office**
University of Ljubljana, Faculty of Mechanical Engineering
SV-JME, Aškerčeva 6, SI-1000 Ljubljana, Slovenia
Phone: 386 (0)1 4771 137
Fax: 386 (0)1 2518 567
info@sv-jme.eu, http://www.sv-jme.eu

**Print:** Grafex, d.o.o., printed in 310 copies

**Founders and Publishers**
University of Ljubljana, Faculty of Mechanical Engineering, Slovenia
University of Maribor, Faculty of Mechanical Engineering, Slovenia
Association of Mechanical Engineers of Slovenia
Chamber of Commerce and Industry of Slovenia, Metal Processing Industry Association



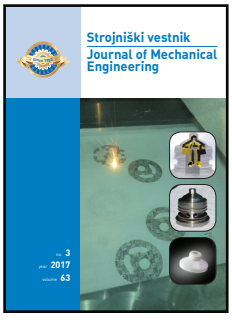


**Cover:** The cover shows the application of selective laser melting of injection mould tooling (insert). Conformal cooling channels of moulding insert are presented on upper small picture. Middle small picture shows moulding insert produced by hybrid manufacturing which include selective laser melting and machining. The final product of injection moulding, tube shoulder is presented on bottom small picture.

*Image Courtesy:*
David Homar, Laboratory for Machining, Faculty of Mechanical Engineering, University of Ljubljana, Askerceva 6, 1000 Ljubljana, Slovenia,
e-mail: david.homar@fs.uni-lj.si
http://lab.fs.uni-lj.si/labod/

**ISSN 0039-2480**



**General information**
Strojniški vestnik – Journal of Mechanical Engineering is published in 11 issues per year (July and August is a double issue).

Institutional prices include print & online access: institutional subscription price and foreign subscription €100,00 (the price of a single issue is €10,00); general public subscription and student subscription €50,00 (the price of a single issue is €5,00). Prices are exclusive of tax. Delivery is included in the price. The recipient is responsible for paying any import duties or taxes. Legal title passes to the customer on dispatch by our distributor.

Single issues from current and recent volumes are available at the current single-issue price. To order the journal, please complete the form on our website. For submissions, subscriptions and all other information please visit: *http://en.sv-jme.eu/.*

You can advertise on the inner and outer side of the back cover of the journal. The authors of the published papers are invited to send photos or pictures with short explanation for cover content.

We would like to thank the reviewers who have taken part in the peer-review process.



The journal is subsidized by Slovenian Research Agency.

Strojniški vestnik - Journal of Mechanical Engineering is available on http://www.sv-jme.eu, where you access also to papers' supplements, such as simulations, etc.

# Contents

**Strojniški vestnik - Journal of Mechanical Engineering**
**volume 63, (2017), number 3**
**Ljubljana, March 2017**
**ISSN 0039-2480**

**Published monthly**

**Papers**

Strojniški vestnik - Journal of Mechanical Engineering 63(2017)3, 151-160

DOI:10.5545/sv-jme.2016.3924 Original Scientific Paper
Received for review: 2016-08-01
Received revised form: 2016-10-25
Accepted for publication: 2016-12-21

# The Development of a Recognition Geometry Algorithm for Hybrid – Subtractive and Additive Manufacturing

David Homar* – Franci Pušavec
University of Ljubljana, Faculty of Mechanical Engineering, Slovenia

*In the last decade additive manufacturing of metal components has experienced enormous development. One of the most important achievements in this sector is the fact that nowadays it is possible to produce fully dense metal parts. Generally, additive manufacturing technologies are able to produce very complex geometries but are time and cost consuming for manufacturing of massive components. Machining technology, on the other hand, has the opposite characteristics. Both technologies, additive and subtractive, have advantages and disadvantages depending on the amount of material that need to be added or subtracted. The combination of these two technologies (i.e. hybrid manufacturing) results in a process where advantages of both technologies can be expected (cost, material consumption, etc.). Thus a novelty, the paper presents a development and analysis of software that analyzes the CAD model with geometry of the model and declares which part of model will be manufactured with machining and which will be produced by additive manufacturing. The software is evaluated on an industrial case from the field of injection mould inserts. Results show that such an automated algorithm decreases cost, better efficiency and nevertheless offer possibility to implement technology in industrial environment to improve manufacturing processes, i.e. in current case injection moulding process/technology.*

**Keywords: hybrid manufacturing, additive manufacturing, subtractive manufacturing, machining, conformal cooling channels**

**Highlights**

- *Description of hybrid manufacturing as combination of additive and subtractive technologies has been described.*
- *Hybrid manufacturing of injection mould tooling with conformal cooling channels has been analyzed.*
- *Newly developed geometry recognition algorithm to determine manufacturing technology has been presented and described in detail.*
- *Algorithm has been evaluated on an industrial injection moulding case.*
- *Conformal cooled injection mould insert improves the productivity and quality of injection moulded plastic parts.*

## 0 INTRODUCTION

Product design is significantly dependent on its manufacturing processes. Machining, which is one of the subtractive processes, has a number of limitations related to the complexity of the product geometry [1]. Design of most products, which are to be produced by machining, is adapted to the technology itself [2].

In the last decade, techniques that combine two or more manufacturing processes, such as subtractive and additive technologies, are gaining significant attention. This has resulted in many researches on the combination of subtractive and additive technologies. As a contribution to the field, in this paper an algorithm, which was developed for the purpose of being used with a hybrid manufacturing cell, is presented. The hybrid manufacturing cell was developed at institute SINTEF [3] to [5], where two manufacturing machines have been used/combined. The first machine is a Deckel-Maho 5-axis CNC milling center and the other is ConceptLaser M2 for selective laser melting of metal powders. The aim of the hybrid manufacturing cell is to automate the hybrid manufacturing process as much as possible, for the production of different products. The developed algorithm presented in this paper is a significant part of this automation chain. The desired operation of the control system in the hybrid manufacturing cell is to analyze the intended product CAD model with the mentioned algorithm and determine which parts are c be manufactured by the additive and which by the subtractive process.

The first attempt to combine benefits of additive and subtractive manufacturing was the low cost integration of an arc welding unit on a 3-axis CNC milling center, presented in [6] and [7]. The main purpose of this research was to manufacture the near-net shape of the product by weld-deposition of material directly on the CNC machine table and then improve the quality of the product surface by milling. The idea is good, however, due to the rough nature of the welding process, the researched process demonstrates limited benefits of other additive manufacturing processes.

Several researchers have published work on the methodology for the evaluation of manufacturing complexity for both additive and machining manufacturing [8] and [9], specifying

*Corr. Author's Address: University of Ljubljana, Faculty of Mechanical Engineering, Aškerčeva 6, 1000 Ljubljana, Slovenia, david.homar@fs.uni-lj.si

the manufacturability index and possible desired manufacturing technology. The manufacturability index has been specified to be dependent on the material and geometry, as well as other detailed specifications. In papers [8] and [9] the calculation of the manufacturability index from a CAD model was constructed basing on an octree decomposition. In the paper [10], researchers presented a new design for the manufacturing approach with machining and additive manufacturing combined. The methodology was illustrated on two industrial examples. The manufacturability index on the second example, taken from automotive industry, was calculated first for machining and then for additive manufacturing. Analyses show that additive and subtractive technologies have to be combined, while the CAD model has to be imaginarily split into two parts: a first module for machining and a second for additive technology, added directly onto the first module.

In the last years, researchers introduced newly developed hybrid manufacturing process planning methods to synthesize subtractive, additive and inspection processes [11] to [13]. With these methods, products can be manufactured from existing part material and be remanufactured into new products with new identities. The basis for hybrid manufacturing is the decomposition of the 3D CAD model into two or more subparts which are manufactured in sequence by machining and additive manufacturing. One of the main disadvantages of introducing additive manufacturing into a machining process is the manufactured part distortion which was therefore thoroughly investigated. Part distortion is the result of residual stresses that are a consequence of non-uniform heating and cooling. Authors have identified parameters influencing part distortion using the developed mathematical model and incorporated these parameters in an experimental design by employing the Taguchi design of experiments strategy. Layer thickness, height and length of the parts were found to have the most significant effect on part distortion.

Yamazaki published a paper [14], in which a newly developed Hybrid Multi-tasking machine named MAZAK INTEGREX i-400 AM is presented along with an experiment of adding Inconel 718 features on a Stainless Steel shaft. INTEGREX i-400 AM is basically a 5 axis milling machine with two different heads for laser metal deposition (LMD) integrated. The first one is a fine LMD head delivering a bead size of 1 mm × 0.5 mm ($w \times h$), intended for additive manufacturing processes, where high accuracy is demanded. The second one is a high speed LMD head which enables higher deposition rate with a consequently reduced accuracy, delivering a bead size of 3 m × 1 m ($w \times h$). The presented experiment consists of manufacturing an example shaft for oil-energy industry purposes, where the substrate shaft material is Stainless Steel alloy 316S31 and the added material is Inconel 718 powder. The presented hybrid application results in a significant reduction in tool consumption and material cost.

The group of researchers [15] developed a part complexity evaluation model for application in subtractive and additive technologies. STereoLithography (STL) models of different parts were taken for evaluation of manufacturing complexity. Manufacturing complexity was defined by the number of triangles in the model surface and the model square block volume. Additionally, manufacturing complexity, defined in this way, was compared to the manufacturing complexity, based on their own experiences with manufacturing processes. Based on that, guidelines for selecting appropriate manufacturing procedures were defined. Production is significantly dependent on the complexity of the product, especially when comparing subtractive and additive technologies. Even more, both technologies could/should be combined on one/same part/product. Therefore, hybrid manufacturing is inevitable.

## 1 HYBRID MANUFACTURING

Subtractive and additive manufacturing technologies have their advantages and disadvantages [16]. Hybrid manufacturing indicates a process, where one part is produced by two or more completely different manufacturing technologies and the advantages of each technology are used, while the disadvantages are eliminated [17]. In our case, good is to use subtractive and additive technologies on one part/product.

Machining is one of the few subtractive manufacturing technologies (milling, turning, etc.). Parts are manufactured by removing material from the workpiece with a sharp cutting tool with defined cutting geometry [18]. In current case 5-axis milling is going to be tested.

In case of additive technology the computer-aided design (CAD) model is sliced into cross section layers using a specific software and a computer numerical control (CNC) code or pictures of cross sections are then generated, depending on the type of additive technology being used. The most common additive technologies for metal products are electron beam melting (EBM), laser deposition technology (LDT) and selective laser melting (SLM). In current case focus is on SLM. SLM is a technology in which

the high power laser beam is used to build metal parts by selectively melting the metallic powder layer after layer. At the beginning of the process, before the metallic powder is melted, it is spread in a thin layer above the emerging manufactured part. For this reason SLM technology is also known as one of the powder bed technologies.

### 1.1 Hybrid Manufacturing - Benefits and Limitations of Both Technologies

Each manufacturing process has some advantages and disadvantages. The aim of hybrid manufacturing is combining both processes in order to eliminate as much disadvantages as possible.

The machining process is able to produce products with a high surface quality and very good accuracy [19], as well as to achieve high production speeds. On the other hand, products with a complex geometrical structure are very difficult or sometimes impossible to machine because the cutting tool cannot reach some geometry on the part (internal channels, etc.). The reason for this limitation is that the shape of the cutting tool itself prevents access to some places where metal has to be removed.

SLM is the exact opposite to the machining processes. Every kind of geometrical shape can be manufactured by SLM as the manufactured part is built by adding material layer by layer. The biggest disadvantage of SLM, as well as other additive manufacturing processes, is bad surface roughness [20]. There are two main reasons for this. First is common to all additive manufacturing processes and it is known as the stair-stepping phenomenon. Because the product is created layer by layer, all this processes leave a stair on the surface for each layer. The second reason is the generated melt pool, where many complex physical phenomena are involved. The behavior of the melt pool depends on thermo-capillary forces, melt pool dynamics, currents of chemical diffusion, wetting conditions, convective heat conduction, diffusive heat conduction, gravity and so forth. Another big disadvantage of SLM is that production times are very long.

From the economic point of view SLM is not suitable for manufacturing bigger parts with relatively simple geometry, because, in comparison to machining, this kind of geometry is too time-consuming and expensive to produce.

Fig. 1 shows a graph of machined product costs dependence on the amount of subtracted material and additive manufacturing product costs dependence on the amount of added material to produce the final geometry. The cost of a machined product also increases with increasing shape complexity. However complexity of product shape does not affect the cost of product manufactured by SLM. From the graph it can be summarized that it is more economical to manufacture a larger proportion of the part by machining, followed by additive process.

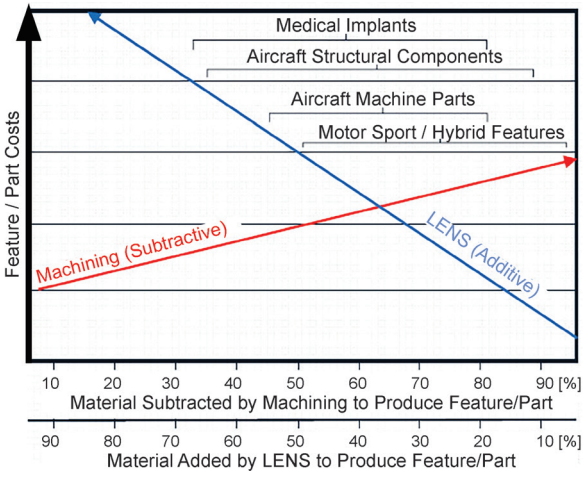


**Fig. 1.** *The cost of production for a part produced by machining or additive manufacturing* [21]

### 1.2 Case Study - Injection Moulding Tool Insert with Conformal Cooling Channels

In the last decade, in injection moulding industry is facing more and more frequently with the need for tools with conformal cooling channels. Conformal cooling channels are channels which are designed to adopt the shape of the injection mould tool cavity and core as much as possible, to improve and control the cooling process of the mould.

With conformal cooling, a tool or tool insert cooling efficiency, the uniformity of cooling and mechanical properties of moulded material are increased. These means that the cycle time and the cost of injection moulding are reduced and better product quality can be achieved. Cooling cycle time can be reduced up to 50 % [22]. On Figs. 2 and 3 the difference between conventional and conformal cooling management is presented. Conformal cooling tool or tool inserts cannot be produced by conventional technologies, such as machining, because the cutting tool cannot reach the complex shape of the conformal cooling channels. SLM, on the other hand, is able to produce almost any shape, even complex internal shapes such as conformal cooling channels. However, the question that is raised is, can a portion of the part

be produced on conventional and wich part. Therefore an algorithm has been developed for defining the portion of geometry for their sequential production (subtraction > additive).

## 2 DEVELOPED GEOMETRY SEPARATION ALGORITHM

Optimized manufacturing operation sequence (OMOS) is a newly developed and proposed option in the automatization of hybrid manufacturing. The aim of the OMOS algorithm, which is implemented in the CAD computer software, is to analyze the geometric design of a product and to determine which part of the product cannot be manufactured by machining due to the complexity of the product geometry. This part is then separated from the initial CAD model and is meant to be produced by additive manufacturing. The remaining part of the initial CAD model is meant to be produced by machining [23] and [24].

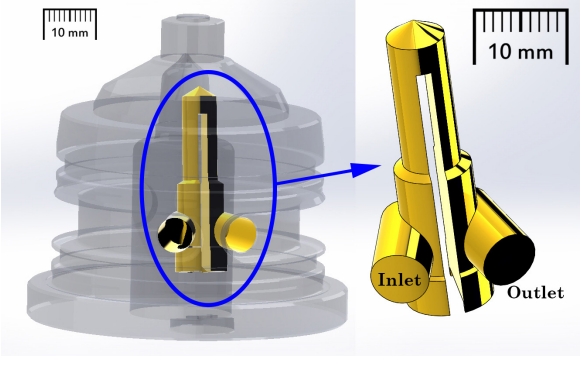


**Fig. 2.** *Case study - conventional cooling management*

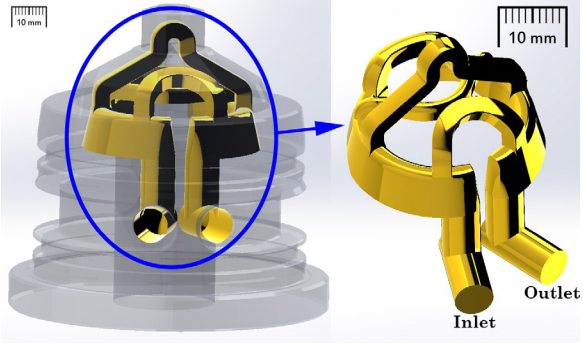


**Fig. 3.** *Case study - conformal cooling management*

The methodology for analyzing a geometric design is presented on Fig. 4 as a flowchart. The OMOS algorithm bases on the assumption that machining is basically a faster and a more economical technology than SLM. Therefore, the aim is to determine the biggest part of the product that can be produced by machining.

This algorithm has been developed and incorporated into the CAD software (SolidWorks). Besides finding the portion of the part that can be produced by subtractive technology, algorithm checks and implements also the limits and constraints of the additive manufacturing process.

SLM technology is one of the powder bed fusion (PBF) technologies which is significantly more accurate than the direct energy deposition technology that is usually used in machines for hybrid manufacturing. PBF technology allows to add material only on straight and horizontal surfaces of the part and demands a lot of time for preparation of the workpiece on the machine before performing the additive manufacturing process. Therefore, the complexity of dealt with additive manufacturing processes (PBF), limits the flexibility and determines constraints of this methodology.

For the verification and presentation of the OMOS algorithm a CAD model, which imitates an injection moulding tool insert with conformal cooling channels, was used. The CAD model is presented on Fig. 5. Fig. 5a presents the outer shape of the model. The transparent model, where the shape of the cooling channels is shown, is presented on Fig. 5b. The bottom part of the CAD model has straight cooling channels which can be manufactured by machining but the upper part has helix shaped channels which cannot be done by machining because the cutting tool cannot reach these faces of the cooling channels.

Vectors which represent cutting tools are a major element of the OMOS algorithm. At the start, the algorithm takes two points which are the boundary points of the CAD model. These two points are presented on Fig 6. The first point represents the minimum $x$, $y$ and $z$ coordinates of the analyzed part. The second point represents the maximum $x$, $y$ and $z$ coordinates. These two points are the key data for further analysis, because vectors are generated in the part's bounding box. The starting points of the vectors are 1 mm below the bottom or base face of the tool insert. All vectors are parallel and their direction is (0, 0, 1), as it is shown on Fig. 7. The starting point of the first vector is $(x_{\min}, y_{\min}, z_{\min}-1)$ mm. The next vector has its $x$ coordinate increased for $\Delta l$ and so on. The distance between adjacent vectors, $\Delta l$, is 0.1 mm. Our analyses have shown that the distance 0.1 mm is small enough to get the correct height for splitting the part. If $\Delta l$ is reduced, the number of inserted vectors is increased and the analysis is more accurate, but it is done in a greater amount of time. For a better

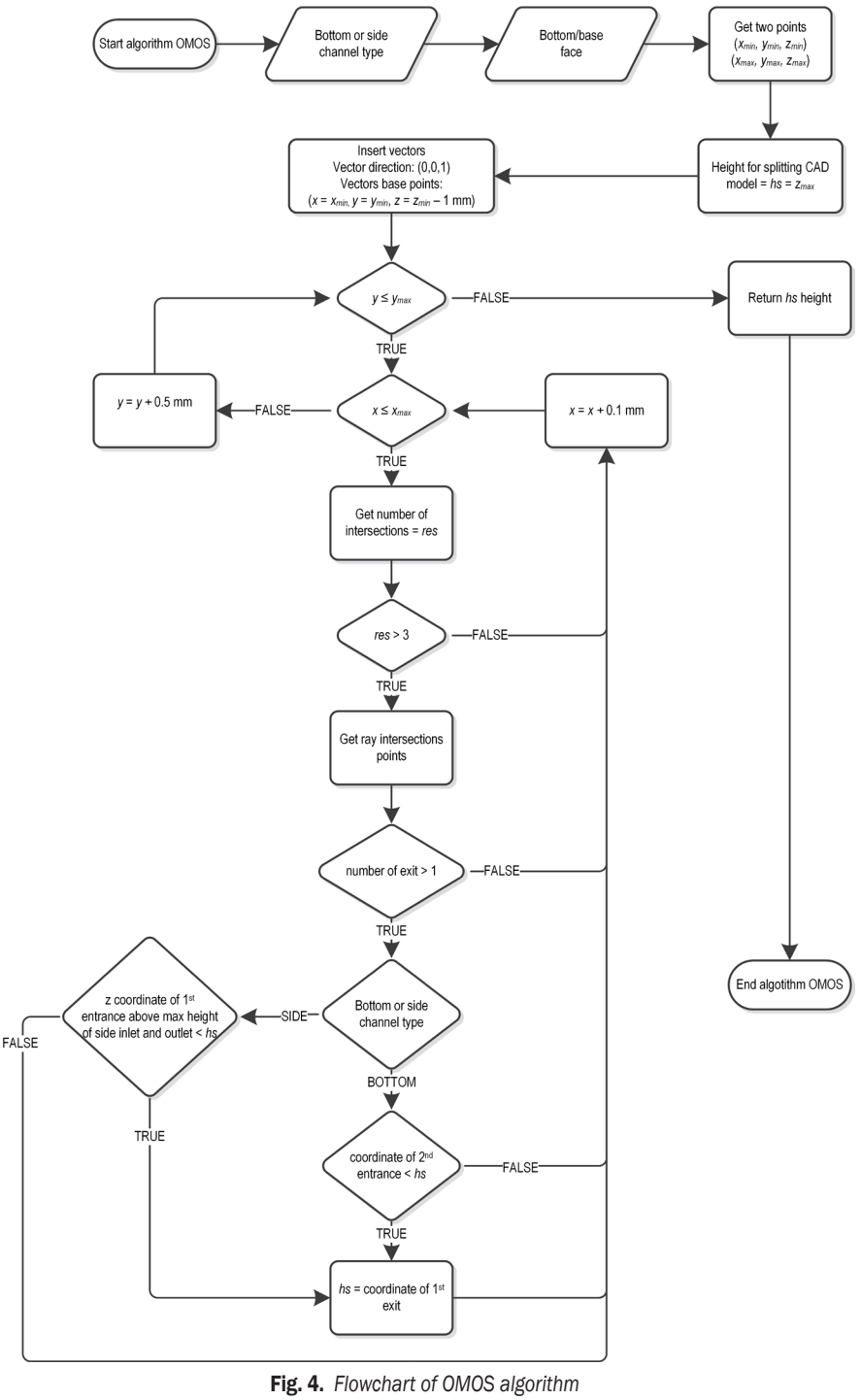


**Fig. 4.** *Flowchart of OMOS algorithm*

presentation $\Delta l$ on figure is bigger than 0.1 mm which was the value used in the case.

The program calculates the intersection points of vectors with the analyzed CAD model surfaces. Only vectors which have more than 3 intersections and more than 2 exits with CAD model surfaces are used for further analyze. The A-A crosssection of the CAD model in Fig. 6 is presented along with the inserted vectors in Fig. 8. The vectors that intersect the CAD model more than three times and exit the CAD model at least two times are presented in orange-dashed line and are used for further analysis. The algorithm

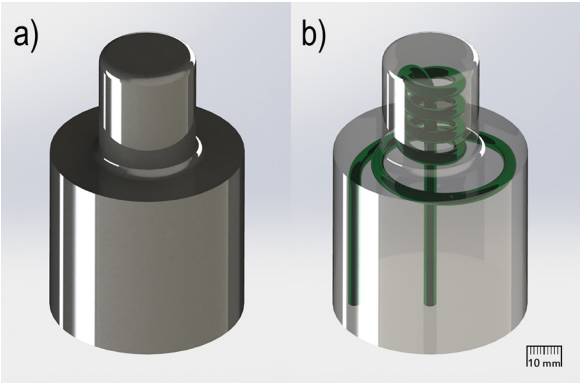


**Fig. 5.** *CAD model of injection moulding tool insert with conformal cooling channels; a) the solid model and b) the transparent model*

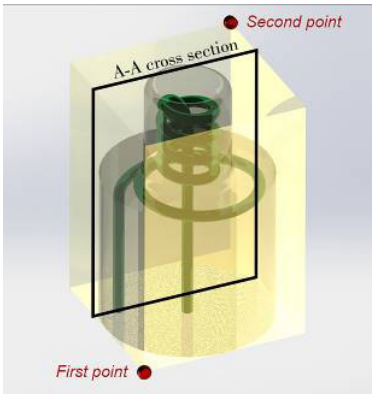


**Fig. 6.** *Developed algorithm - boundary box of the CAD model with marked A-A cross section*

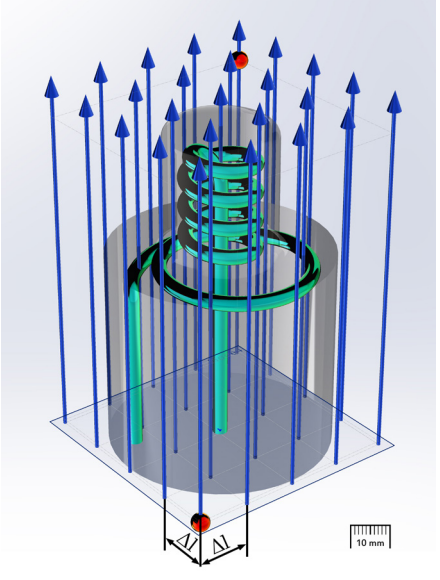


**Fig. 7.** *Developed algorithm - inserted vectors*

calculates the splitting height, *hs,* as the lowest of the *z* coordinates of the first exit points of the analyzed

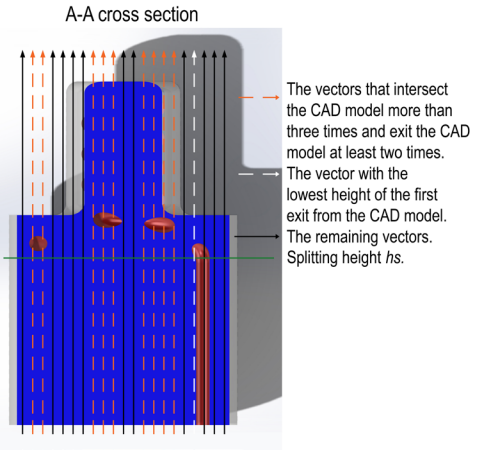


**Fig. 8.** *Developed algorithm - A-A cross-section of the CAD model presented along with the inserted vectors*

vectors in that case where the inlet and outlet channels are on the bottom face. In this case, the splitting height *hs* is determined by the white-dashed vector in Fig. 8, as the height of the first exit from the CAD model is the lowest of the analyzed (orange-dashed) vectors, and is marked with the green horizontal line.

In the case, where the inlet and outlet channels are on the side face, the algorithm calculates hs as the lowest z coordinate of the first entrances of the analyzed vectors above the highest z coordinate of the side inlet and outlet channels.

## 3 INCORPORATION OF OMOS ALGORITHM INTO CAD SOFTWARE

The developed OMOS algorithm was implemented in SOLIDWORKS software package by Dassault Systems with the application programming interface (API) tool. With SOLIDWORKS API it is possible to automate and personalize software. That can be done from different programing languages. C# was used in this work. The order of operations to be carried out when the OMOS software is started is shown in the flowchart on Fig. 9.

The CAD model of the injection moulding tool insert or another similar product, which is to be analyzed, has to be open in SolidWorks software where OMOS software was preinstalled. In software the user selects between choices of inlet and outlet channels being on the bottom or on the side face. User selects also the bottom face in the graphics area. Upon confirmation of selected face, the OMOS algorithm is executed. The OMOS algorithm returns the height to which the CAD model can be manufactured by

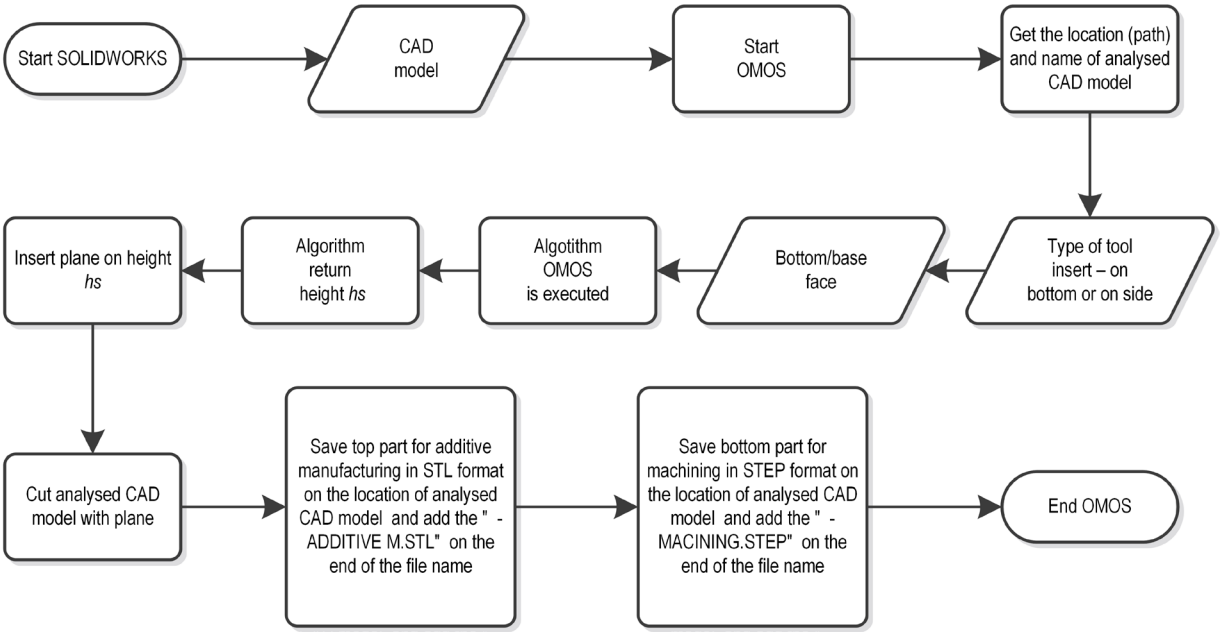


**Fig. 9.** *Flowchart of developed algorithm and software OMOS*

machining, *hs*. After that, a new plane which is parallel to the bottom face is generated on height *hs*. Thus, the part is split in two parts by the new plane. The bottom part is intended for machining and the upper part is intended to be manufactured by additive manufacturing.

Subsequently, the OMOS software automatically saves the bottom part as STEP, while this format is most often used for preparation of CNC tool path code. However, the upper part is saved as STL file that is a hollow CAD model where the surface of the model consists of only triangles. STL file format is standard for transferring CAD geometry between design programs and additive manufacturing equipment. These two files are saved in the same folder as the initially analyzed CAD model and can be directly used for both parts of hybrid manufacturing.

## 4 USE OF THE SOFTWARE OMOS ON THE INDUSTRIAL CASE STUDY

The OMOS software was used and evaluated on an industrial case of producing an injection mould tool insert for the mass production of tube shoulders. The CAD model of the mould insert with conformal cooling channels, which was already presented on Fig. 3, has been analyzed. The distance between adjacent vectors was set to 0.1 mm. The entrance and the exit of cooling channels were placed on rather on the side of the part than on the bottom face of the part. Thus, in the geometry recognition algorithm, the side channel type of tool insert was selected in window form (Fig. 10).

After the analysis, the CAD model was automatically split on the height of 27.88 mm. Fig. 11 shows in cross section view where the CAD model of tool insert is split on the right height, because bottom part of the model can be manufactured by machining.

If the height of the splitting plane was just slightly greater, the bottom part could not be manufactured by machining, because the drill bit would not be able to reach the vertical holes. The resulting split CAD model, as an output from developed algorithm, is presented on Fig. 12. Based on this, the tooling insert was successfully manufactured by hybrid manufacturing. The final product, had to be finished by finishing subtractive process, and is presented on Fig. 13.

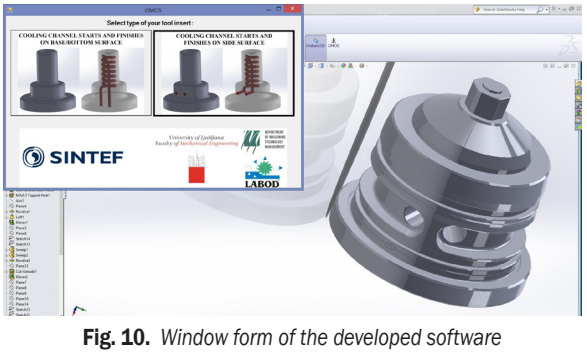


**Fig. 10.** *Window form of the developed software*

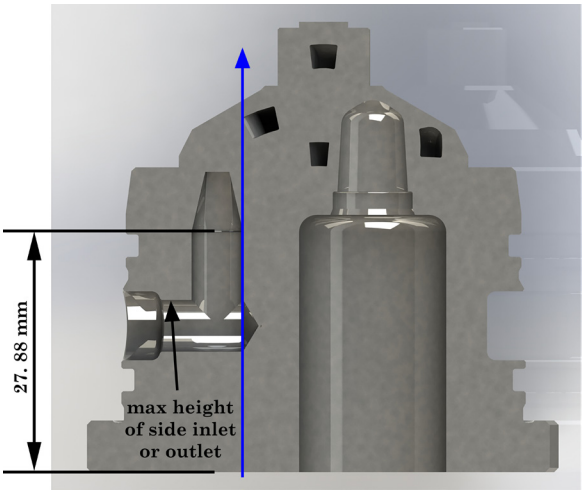


**Fig. 11.** *Height of splitting*

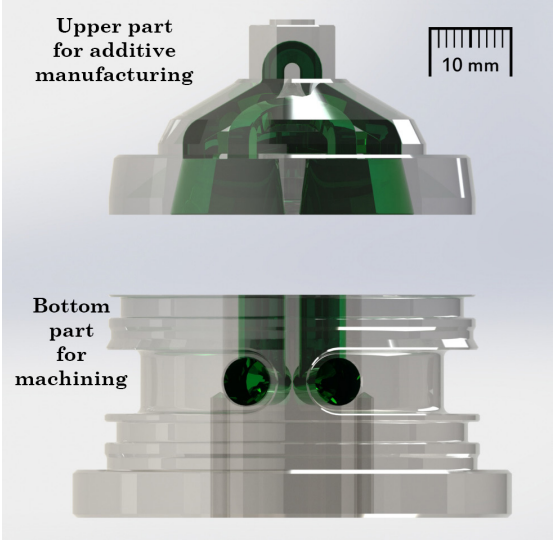


**Fig. 12.** *Split part*

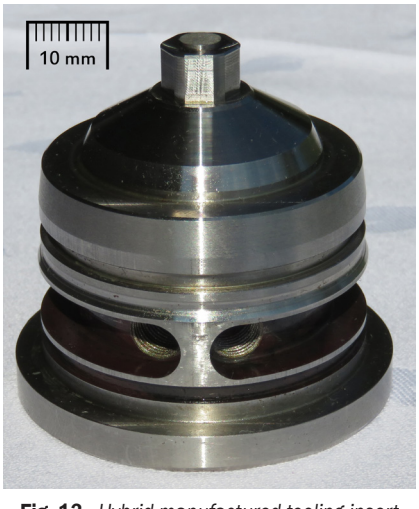


**Fig. 13.** *Hybrid manufactured tooling insert*

## 5 VERIFICATION OF THE DEVELOPED OMOS ALGORITHM AND SOFTWARE

Verification of the developed algorithm and software was carried out by analyzing production times and costs for injection moulding tool inserts, manufactured by additive and by hybrid manufacturing. The manufacturing of five injection moulding tool inserts that are needed for one complete injection tool, was analyzed. Following, the comparison of the production times and costs, comparing both manufacturing techniques, was performed.

Related to production times, the effective machining time was calculated for full additive manufacturing and hybrid manufacturing technique. The full subtractive method cannot be compared here, while it does not offer a possibility to manufacture such a geometrical characteristics of the products (channels). Table 1 presents the results for five injection moulding tool inserts, for both manufacturing techniques. The presented production times indicate the total time for manufacturing all five injection tool moulds that were manufactured simultaneously. In the case, where the inserts are manufactured only by additive manufacturing, the production time for 5 products is 86 h. However, production time in the case of hybrid manufacturing, where the developed OMOS algorithm and software were used, is 42 h. It can be seen that hybrid manufacturing is decreasing production times for more than 50 %. Therefore, the use of the hybrid manufacturing technique and the OMOS algorithm with software, significantly reduces production time, especially while the methodology is automated.

**Table 1.** *Production time of the five injection moulding tool inserts using different techniques*

| | Additive manufacturing | Hybrid manufacturing |
|---|---|---|
| Production time [h] | 86 | 42 |

Besides production times, crucial are also production costs. Fig. 14 shows the material and production cost comparison between both manufacturing techniques in the form of column charts. The blue columns show the comparison of material costs. The material cost for parts, manufactured by additive manufacturing, was more than 150 percent higher compared to the material cost for parts manufactured by the hybrid technique. The reason for that is that the price of the metal powder for SLM is 20 times higher than the price

of the material in metal bars (400 €/kg vs. 20 €/kg). However, less material is used in additive process. For five injection moulding tool inserts a total of 2.2 kg of metal powder is needed when manufacturing only by additive manufacturing. However, in the case of the hybrid technique, 0.62 kg of metal powder and 4.57 kg of material for lower part, was needed. The reason for that is that the OMOS algorithm and software determined the smallest possible upper part, which has to be done by additive manufacturing, but the bottom part was manufactured by machining, where it has to be emphasized that raw material is significantly cheaper.

The orange columns in the chart present the comparison of production cost between additive and hybrid manufacturing of the five injection moulding tool inserts. The technology of SLM is a highly time consuming process. For the manufacture of the entire inserts by additive manufacturing, a total of 86 h is needed, what brings the production cost to 2580 € (30 €/h). However, in the case of the hybrid manufacturing and the use of the OMOS algorithm and software, only 33 h were consumed for the additive manufacturing process. In this case nine hours of the machining was performed before additive manufacturing. The total production cost of machining and additive manufacturing, in case of hybrid manufacturing, was 1440 €. Verification of the developed algorithm was confirmed by fully functional parts in both dealt with technologies. Results highlight the improvements of such technology in sense of costs and cycle times. Reduced production cost justifies the use of the developed OMOS algorithm and software.

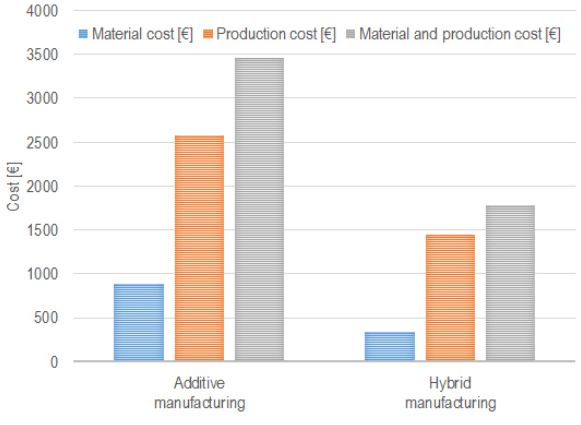


**Fig. 14.** *The comparison of the material and production costs for additive and hybrid manufacturing*

## 6 CONCLUSIONS

The implementation of additive technologies into current industry can bring gain in possibility for production of high complex parts (conformal cooling channels, etc.). However, problematic issues of such technologies are high costs and long production cycles.

Therefore, in this paper, the concept of hybrid manufacturing process, combining subtractive and additive process on single final part, is analyzed. For evaluation and characterization of the portion of geometry that can be made with subtractive/ additive manufacturing process, novel algorithm with belonging software OMOS is developed. Developed OMOS algorithm was thus introduced for automated recognition of manufacturing possibility of a specific part geometry. The algorithm determines the most advantageous division between which parts and features should be produced by either of the manufacturing principles. The OMOS algorithm is developed for a hybrid manufacturing cell where additive and subtractive technologies are used to produce especially injection mould tooling inserts. The algorithm was implemented in a commercial CAD software, and verified on industrial case study.

An industrial example has been taken from the field of tooling for injection moulding. The conventional manufacturing process has been compared with hybrid one, on production of injection moulding tooling. Results show that hybrid manufacturing can assure all the desired geometrical characteristics. Even more, the hybrid process can optimize the additive manufacturing process and produce functional features (cooling channels for conformal cooling of injection mould).

The OMOS algorithm and software viability wasadditionally verified by the analysis of the material and production costs, as well as the production (cycle) times. Saving time and production costs are the results of the OMOS algorithm and software, whose development was based on the assumption that machining is a faster and a more economical production technology than SLM.

Overall, the results of this work show the need for combining potential of additive manufacturing technologies with conventional (machining) technologies, and with it assure quality improvement, costs reduction, as well as possibility to produce high complex workpieces and with those improve the mass productivity and quality of final products.

## 7 REFERENCES


[1] Sandberg, M. (2007). *Design for Manufacturing: Methods and Applications Using Knowledge Engineering*. PhD thesis, Lulea University of Technology, Lulea.

[2] Poli, C. (2001). *Design for Manufacturing: A Structured Approach*. Butterworth-Heinemann, Boston.

[3] Brotan, V., Bovie, K.M., (2012). The hybrid manufacturing cell: Determining key parameters in the integration of powder bed fusion with high speed milling. *IEEE International Conference on Industrial Engineering and Engineering Management*, p. 583-587, **DOI:10.1109/IEEM.2012.6837806**.

[4] Boivie, K., Dolinsek, S. Homar, D. (2011). Hybrid manufacturing; integration of additive technologies for competitive production of complex tools and products. *15th International Research/Expert Conference: Trends in the Development of Machinery and Associated Technology*, p. 53-56, Prague.

[5] Boivie, K., Karlsen, R., Ystgaard, P. (2012). The concept of hybrid manufacturing for high performance parts. *The South African Journal of Industrial Engineering*, vol. 23, no. 2, p. 106-115, **DOI:10.7166/23-2-334**.

[6] Karunakaran, K.P., Suryakumar, S., Pushpa, V., Akula, S. (2010). Low cost integration of additive and subtractive processes for hybrid layered manufacturing. *Robotics and Computer-Integrated Manufacturing*, vol. 26, no. 5, p. 490-499, **DOI:10.1016/j.rcim.2010.03.008**.

[7] Karunakaran, K.P., Suryakumar, S., Pushpa, V., Akula, S. (2009). Retrofitment of a CNC machine for hybrid layered manufacturing. *The International Journal of Advanced Manufacturing Technology*, vol. 45, no. 7, p. 690-703, **DOI:10.1007/s00170-009-2002-2**.

[8] Kerbrat, O., Mognol, P., Hascoet, J.Y. (2010). Manufacturability analysis to combine additive and subtractive processes. *Rapid Prototyping Journal*, vol. 16, no. 1, p. 63-72, **DOI:10.1108/13552541011011721**.

[9] Kerbrat, O., Mognol, P., Hascoët, J.Y. (2010). Manufacturing complexity evaluation at the design stage for both machining and layered manufacturing. *CIRP Journal of Manufacturing Science and Technology*, vol. 2, no. 3, p. 208-215, **DOI:10.1016/j.cirpj.2010.03.007**.

[10] Kerbrat, O., Mognol, P., & Hascoët, J.-Y. (2011). A new DFM approach to combine machining and additive manufacturing. *Computers in Industry*, vol. 62, no. 7, p. 684-692, **DOI:10.1016/j.compind.2011.04.003**.

[11] Newman, S.T., Zhu, Z., Dhokia, V., Shokrani, A. (2015). Process planning for additive and subtractive manufacturing technologies. *CIRP Annals - Manufacturing Technology*, vol. 64, no. 1, p. 467-470, **DOI:10.1016/j.cirp.2015.04.109**.

[12] Zhu, Z., Dhokia, V., Newman, S.T., Nassehi, A. (2014). Application of a hybrid process for high precision manufacture of difficult to machine prismatic parts. *The International Journal of Advanced Manufacturing Technology*, vol. 74, no. 5, p. 1115-1132, **DOI:10.1007/s00170-014-6053-7**.

[13] Zhu, Z., Dhokia, V., Nassehi, A., Newman, S.T. (2016). Investigation of part distortions as a result of hybrid manufacturing. *Robotics and Computer-Integrated Manufacturing*, vol. 37, p. 23-32, **DOI:10.1016/j.rcim.2015.06.001**.

[14] Yamazaki, T. (2016). Development of a hybrid multi-tasking machine tool: integration of additive manufacturing technology with CNC machining. *Procedia CIRP, 18th CIRP Conference on Electro Physical and Chemical Machining*, vol. 42, p. 81-86, **DOI:10.1016/j.procir.2016.02.193**.

[15] Valentan, B., Brajlih, T., Drstvenšek, I., Balič, J. (2011). Development of a part-complexity evaluation model for application in additive fabrication technologies. *Strojniški vestnik - Journal of Mechanical Engineering*, vol. 57, no. 10, p. 709-718, **DOI:10.5545/sv-jme.2010.057**.

[16] Daneshmand, S., Aghanajafi, C. (2012). Description and modeling of the additive manufacturing technology for aerodynamic coefficients measurement. *Strojniški vestnik - Journal of Mechanical Engineering*, vol. 58, no. 2, p. 125-133, **DOI:10.5545/sv-jme.2010.238**.

[17] Liou, F., Slattery, K., Kinsella, M., Newkirk, J., Chou, H.-N., Landers, R. (2007). Applications of a hybrid manufacturing process for fabrication of metallic structures. *Rapid Prototyping Journal*, vol. 13, no. 4, p. 236-244, **DOI:10.1108/13552540710776188**.

[18] Krolczyk, G.M., Krolczyk, J.B., Maruda, R.W., Legutko, S., Tomaszewski, M. (2016). Metrological changes in surface morphology of high-strength steels in manufacturing processes. *Measurement*, vol. 88, p. 176-185, **DOI:10.1016/j.measurement.2016.03.055**.

[19] Wojciechowski, S., Twardowski, P., Pelic, M., Maruda, R. W., Barrans, S., Krolczyk, G.M. (2016). Precision surface characterization for finish cylindrical milling with dynamic tool displacements model. *Precision Engineering*, vol. 46, p. 158-165, **DOI:10.1016/j.precisioneng.2016.04.010**.

[20] Galeta, T., Kljajin, M., Karakasic, M. (2008). Geometric accuracy by 2-D printing model. *Strojniški vestnik - Journal of Mechanical Engineering*, vol. 54, no. 10, p. 725-733.

[21] Boivie, K.M. (2013). Metals: An Overview of Processes and Materials. *Proceedings AM–DAGEN*, Kista.

[22] Dalgarno, K., Stewart, T. (2001). Manufacture of production injection mould tooling incorporating conformal cooling channels via indirect selective laser sintering. *Proceedings of the Institution of Mechanical Engineers, Part B: Journal of Engineering Manufacture*, vol. 215, no. 10, p. 1323-1332, **DOI:10.1243/0954405011519042**.

[23] Gibson, I., Rosen, D.W., Stucker, B. (2010). *Additive Manufacturing Technologies: Rapid Prototyping to Direct Digital Manufacturing*. Springer, New York, **DOI:10.1007/978-1-4419-1120-9**.

[24] Gardan, J. (2016). Additive manufacturing technologies: state of the art and trends. I*nternational Journal of Production Research*, vol. 54, no. 10, p. 3118-3132, **DOI:10.1080/00207543.2015.1115909**.

Strojniški vestnik - Journal of Mechanical Engineering 63(2017)3, 161-170

DOI:10.5545/sv-jme.2016.3859 Original Scientific Paper
Received for review: 2016-07-06
Received revised form: 2017-01-05
Accepted for publication: 2017-01-31

# Dynamic Model and Analysis of Nonlinear Vibration Characteristic of a Curve-Face Gear Drive

Zhiqin Cai – Chao Lin*
[1] Chongqing University, The State Key Laboratory of Mechanical Transmission, China

*To study the nonlinear dynamic characteristics of curve-face gear drive, a generalized nonlinear dynamic model based on Lagrange Bond-graphs was presented. The model considered the effects of the basic parameters of curve-face gear, such as meshing frequency, eccentricity k and the order number $n_1$ of non-cylindrical gears. Utilizing this simulation model, the vibration characteristics of curve-face gears were analysed. It is indicated that the vibration response of the curve-face gear is more complex than that of the face gear due to the influence of external excitation. These characteristics determine that this gear pair cannot be applied directly to a transmission system with high speed. Finally, a related experiment was proposed to present the validation of the numerical model.*
**Keywords: curve-face gear, vibration response, limited speed, Lagrange bond-graphs, time-varying characteristics**

**Highlights**
- *A nonlinear dynamic model based on a Lagrange bond-graph was presented. The proposed method not only applies to the dynamic analysis of curve-face gears but also can be applied to face gears.*
- *The research results show that $rb_1$ and R are the main factor affecting the vibration response of curve-face gear, and reducing the eccentricity k and raising the order $n_1$ will improve the dynamic characteristics.*
- *Due to the influence of external excitation, which will exacerbate the vibration, the limited meshing frequency of curve-face gears is lower than face gears. These characteristics determine that the gear cannot be applied to a transmission system with high speed.*

## 0 INTRODUCTION

As a new type of face gear, curve-face gear combines the common characteristics of non-cylindrical gear, bevel gear, and face gear [1]. It can be used in engineering machinery, agricultural machinery, textile machinery and high-powered spacecraft, etc. [2], and will be developed towards high speeds and heavy loads [3]. Therefore, the research on the dynamic characteristics of curve-face gear has increasingly become prominent.

The research of the nonlinear vibration characteristics of gears mainly focuses on the bevel gear, spur gear, face gear and planetary gear drive; the analytical approach of the system generally uses finite element method (FEM), and the Runge-Kutta method is applied to solve the differential equations of the system. For the simulation and vibration-based condition monitoring of a geared system, a system with an appropriate number of degrees of freedom (DOFs) was modelled [4]. An investigation of the performance of statistical fault detection indicators for three different series of crack propagation scenarios was presented [5]. From the vibration signal, the numbers of teeth on all gears, the calculation of tooth mesh frequencies and rotational speeds of all shafts were determined [6]. The dynamic behaviour of a single-stage spur gear reducer in a transient regime was studied [7]. However, for the rotary system with mass eccentricity, the Lagrange equation with generalized coordinates expression is over FEM, as it only relates to the kinetic energy and the potential energy of the system. Therefore, for the mechanical system composed of particles and rigid bodies, the system equation can be obtained quickly by using the Lagrange equation. However, due to the differential calculation of Lagrange function $L$, its simulation process is complex. To overcome the disadvantage of this modelling method, a new modelling method combined Lagrange equation and bond-graph is proposed. When the generalized coordinates, the parameter equation, the force input, and the velocity conversion matrix are determined, the mathematical simulation of the system can be obtained. Compared with the classical method, the modelling process of the Lagrange bond-graph is more regular, and the solving process is more efficient [8].

Recently, few studies were available for the curve-face gear drive. Due to the time-varying characteristics of non-circular gears, the vibration response of this type of gear is much complex than that of normal gears. For general gears, the excitations of the vibration response are mainly time-varying mesh stiffness, tooth transmission error, and meshing impact, etc. The dynamic model of a spur gear pair, considering the backlash, time-varying stiffness,

*Corr. Author's Address: The State Key Laboratory of Mechanical Transmission, Chongqing University, Chongqing, China, linchao@cqu.edu.cn

and static transmission error, was established [9]. Using standard methods for nonlinear systems, the dynamics of gear systems with various faults in meshing stiffness was examined [10]. Considering time-varying mesh stiffness, mesh damping, tooth error, tooth friction, backlash and bearing clearance, a bending-torsion coupled nonlinear dynamic model of a face-gear drive system was established [11]. A nonlinear dynamic model of a face gear system was presented by the concentrated parameters, gear clearances, transmission error, meshing stiffness, meshing damping, brace stiffness, support damping and exciting frequency [12]. However, for a non-circular gear, in addition to the above factors, the regular external excitation, caused by the basic parameters of the non-circular gear, such as meshing frequency, eccentricity $k$ and the order $n_1$ of the non-cylindrical gear, is one of the main influencing factors. For the vibration response of the non-circular gear, a dynamic model of a non-cylindrical gear based on the Lagrange bond-graphs theory was established [13]. A virtual experimental model of the non-cylindrical gear was established, and the corresponding dynamic response was obtained [14]. Considering the time-varying meshing stiffness, a tensional vibration model of a non-circular gear was developed [15]. Bearing in mind input shaft and output shaft excitation, the time-varying meshing stiffness, static transmission error, gear backlash, a nonlinear dynamic model of the twisting vibration of the curve-face gear was established [16]. However, the systematic analysis of the effect of the basic parameters of curve-face gear on the vibration response remain unknow, and the phenomenon of the limited speed of curve-face gear is not yet analysed.

In this paper, a generalized nonlinear dynamic model of curve-face gear based on Lagrange bond-graph was proposed, and the related vibration responses were analysed using bond-graph theory. With the change of meshing frequency, eccentricity $k$ and the order $n_1$ of non-circular gear, different vibration responses were shown in the "time history chart" and "phase diagram". Finally, a related experiment was proposed to verify the correctness of the theoretical mode.

## 1 VIBRATION MODEL REVIEW

The meshing process of the curve-face gear pair is illustrated as shown in Fig. 1. Coordinates $S_1$ ($X_1Y_1Z_1$) and $S_2$ ($X_2Y_2Z_2$) are fixed on the frame of the non-cylindrical gear and the curve-face gear. The non-cylindrical gear and the curve-face gear rotate along their own axis $O_1Z_1$ and axis $O_2Y_2$ with rotation angles $\theta_1$ and $\theta_2$, respectively.

According to the characteristics of the curve-face gear, the meshing force can be decomposed into forces along the direction of axis $X_2$ and axis $Y_2$, and there is no radial force. Compared with the bevel gear, the supporting structure of the curve-face gear pair is relatively simple, and the DOFs of vibration are less.

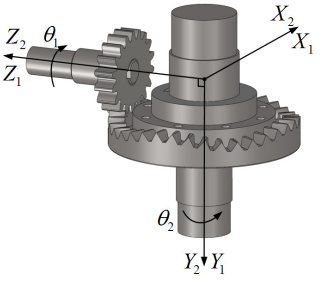


**Fig. 1.** *Modelling of curve-face gear drive*

The transmission ratio of curve-face gear drive and can be expressed as:

$$i_{12} = \frac{R}{r(\theta_1)}. \tag{1}$$

The value of cylindrical radius $R$ and polar radius $r(\theta_1)$ of non-cylindrical gear can be represented as:

$$\begin{cases} r(\theta_1) = \dfrac{1 - k\cos(n_1\theta_1)}{a(1-k^2)} \\ R = \dfrac{n_2}{2\pi}\displaystyle\int_0^{\frac{2\pi}{n_1}} r(\theta_1)\mathrm{d}\theta_1 \end{cases}. \tag{2}$$

### 1.1 Method of Lagrange Bond-Graph

With the complexity of system increases, the conventional method establishing the nonlinear vibration model is quite tedious. Especially for curve-face gear drives, the influence of eccentric mass must be considered [13]. Although the modelling process by the Lagrange equation, based on kinetic energy and potential energy can be easier, the solving process remaining difficult. To overcome this disadvantage, combining with the method of bond-graph, the system equation and the calculation process can be easier. A basic Lagrange bond-graph model is shown in Fig. 2, $X$ represents the field source, such as damping filed - $R$, Inertial field - $I$ and elastic field - $K$, etc. "1" port link the serial energy ports. MIF represents the matrix transformation $T_X \cdot \dot{q}_G$ is the generalized velocity vector which is the first order derivative of generalized displacement $q_G \cdot F_X$ represents the corresponding

force, such as the D 'Alembert force $F_I$, elastic force $F_{K/k}$, dissipative force $F_{R/r}$ and input force $F_s$.

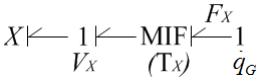


**Fig. 2.** *Basic Lagrange bond-graph model*

$V_X$ is the velocity vector which can be expressed as:

$$V_X = T_X \cdot \dot{q}_G. \tag{3}$$

In this paper, a generalized nonlinear model based on the Lagrange bond-graph is proposed as shown in Fig. 3.

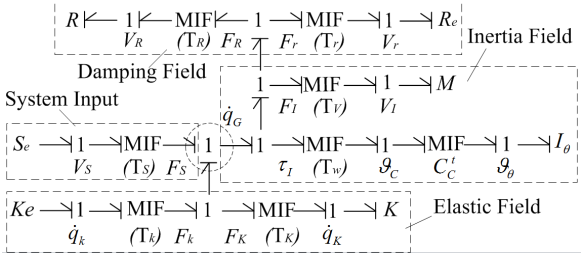


**Fig. 3.** *Lagrange bond-graph model of system*

In Fig. 3, "1" port links the serial energy ports. Each leg (force) has a contribution in "1" port.

$$F_I + \tau_I + F_K + F_R = F_S + F_k + F_r. \tag{4}$$

The hidden dynamic equation of the Lagrange bond-graph model is represented as follows:

$$T_I^t I\left(T_I \frac{d^2 q_G}{dt^2} + \frac{dT_I}{dt}\frac{dq_G}{dt}\right) + T_W{}^t C_C \frac{dC_C^t}{dt} I_C \cdot T_W \frac{dq_G}{dt} + \\ + T_K{}^t K f\left(q_G\right) + T_R{}^t R g\left(q_G\right) = \\ = T_S{}^t \tau_S + T_k{}^t K_e e_t + T_r{}^t R_e \frac{de_t}{dt}. \tag{5}$$

### 1.2 Derivation of Dynamic Model

The dynamic model of a curve-face gear drive is shown in Fig. 4. $Z_1$ and $Y_2$ are rotational axes of the non-cylindrical gear and curve-face gear, respectively. The value of basic parameters, meshing stiffness $k_i$, damping $c_i$ ($i$=$x_1$,$x_2$,$y_1$,$y_2$,$m$), and torque $T_j$ ($j$=1,2) are shown in Table 1.

#### *1.2.1 Determination of Key Vectors*

The displacement vector in generalized coordinates can be represented as:

$$q_G = \left[X_1 \quad Y_1 \quad \theta_1 \quad X_2 \quad Y_2 \quad \theta_2\right]^t, \tag{6}$$

and the displacement vector in elastic field can be defined as:

$$q_K = \left[X_1 \quad Y_1 \quad c_1 X_n \quad X_2 \quad Y_2 \quad c_2 X_n\right]^t, \tag{7}$$

where $c_1 = \cos a_n$, $c_2 = \sin a_n$.

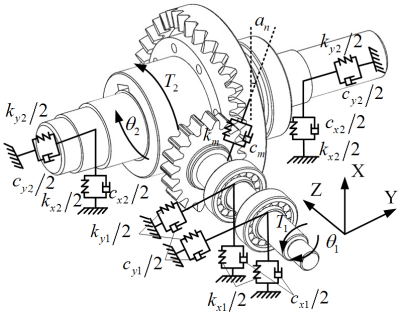


**Fig. 4.** *Dynamic model of curve-face gear drive system*

Input force vector $\tau_S$ can be defined as:

$$\tau_S = \left[0 \quad 0 \quad T_1 \quad 0 \quad 0 \quad -T_2\right]^t. \tag{8}$$

Gear comprehensive error vector can be defined as:

$$e_t = \left|e_t\right| \cdot \left[1 \quad \ldots \quad 1\right]^t_{1\times 6} \tag{9}$$

For the cylindrical gear drive, the pressure angle is equal to the gear shaper. However, this is not so for the curve-face gear pair.

As shown in Fig. 5, $L_1$ as 1, $L_2$ as 2 and $L_3$ as 3 are the pitch curve of the non-cylindrical gear, curve-face gear and gear shaper, respectively. Three tooth profiles $G_1$, $G_2$ and $G_3$ are in tangency at point $P$.

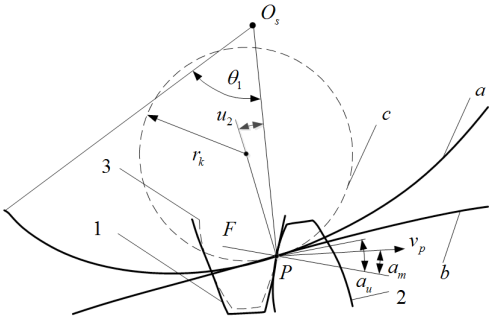


**Fig. 5.** *Pressure angle of curve-face gear drive*

According to the definition of pressure angle, the pressure angle $\alpha_u$ of the gear shaper is constant. However, the pressure angle $\alpha_n$ of the curve-face gear

refers to the angle between absolute velocity $v_p$, and the normal force $F$ which can be obtained as:

$$\alpha_n = \alpha_u + \frac{\pi}{2} - \arctan r(\theta_1)/\dot{r}(\theta_1). \quad (10)$$

Set $X_n$ as the static transmission error.

$$X_n = c_1(X_1 + r_{b1}\theta_1) + c_2 Y_1 - c_1(X_2 + R\theta_2) - c_2 Y_2. \quad (11)$$

However, in the actual condition, gear backlash $2b$ is an important nonlinear factor of gear dynamics, which can be expressed as:

$$f(x) = \begin{cases} X_n - b & X_n > b \\ 0 & |X_n| \le b \\ X_n + b & X_n < -b \end{cases}. \quad (12)$$

### 1.2.2 Determination of Transform Matrix

The curve-face gear drive is a complex transmission system composed of multiple rigid bodies. The comprehensive velocity transform matrix in an inertial field can be expressed as:

$$T_I = \left[\frac{T_V}{T_W}\right]. \quad (13)$$

Moreover, velocity transform matrix in a potential source field can be expressed as:

$$T_S = E_{(6\times 6)}. \quad (14)$$

Velocity transform matrix in a damping field can be expressed as:

$$T_R = \begin{bmatrix} 1 & 0 & 0 & 0 & 0 & 0 \\ 0 & 1 & 0 & 0 & 0 & 0 \\ c_1^2 & c_1c_2 & c_1r_{b1} & -c_1^2 & -c_1c_2 & -c_1R \\ 0 & 0 & 0 & 1 & 0 & 0 \\ 0 & 0 & 0 & 0 & 1 & 0 \\ c_1c_2 & c_2^2 & c_1r_{b1} & -c_1c_2 & -c_2^2 & -c_2R \end{bmatrix}. \quad (15)$$

When taking in account the gear comprehensive error, the velocity transform matrix in a damping field can be expressed as:

$$\mathrm{T}_r = diag(1 \quad 1 \quad r_{b1} \quad -1 \quad -1 \quad -R). \quad (16)$$

The velocity transform matrix in an elastic field can be expressed as:

$$T_K = T_R. \quad (17)$$

Similarly, the velocity transform matrix in an elastic field, considering the gear comprehensive error, can be defined as:

$$T_k = diag(1 \quad 1 \quad r_{b1} \quad -1 \quad -1 \quad -R). \quad (18)$$

The rotation matrix can be expressed as:

$$C_C = \begin{bmatrix} \cos\theta_1 & \sin\theta_1 & 0 & 0 & 0 & 0 \\ -\sin\theta_1 & \cos\theta_1 & 0 & 0 & 0 & 0 \\ 0 & 0 & 1 & 0 & 0 & 0 \\ 0 & 0 & 0 & \cos\theta_2 & \sin\theta_2 & 0 \\ 0 & 0 & 0 & -\sin\theta_2 & \cos\theta_2 & 0 \\ 0 & 0 & 0 & 0 & 0 & 1 \end{bmatrix}, \quad (19)$$

### 1.2.3 Determination of Boundary Conditions

The boundary conditions of curve-face gear drive are represented as follows:

a) Damping field

The damping matrix in a damping field can be expressed as:

$$R = diag\left(c_{x_1} \quad c_{y_1} \quad c_m \quad c_{x_2} \quad c_{y_2} \quad c_m\right). \quad (20)$$

Similarly, when taking into account gear comprehensive error, it can be defined as:

$$R_e = diag\left(c_x \quad c_y \quad c_m \quad c_x \quad c_y \quad c_m\right), \quad (21)$$

where $c_x = c_1c_m$, $c_y = c_2c_m$.

b) Inertial field

The mass matrix in an inertial field can be expressed as:

$$\mathrm{I} = \left[\begin{array}{c|c} \mathrm{M} & 0 \\ \hline 0 & \mathrm{I}_C \end{array}\right]. \quad (22)$$

c) Elastic field

The stiffness matrix in a damping field can be expressed as:

$$K = diag(k_{x_1} \quad k_{y_1} \quad k_m \quad k_{x_2} \quad k_{y_2} \quad k_m). \quad (23)$$

Similarly, when considering gear comprehensive error, it can be defined as:

$$K_e = diag(k_x \quad k_y \quad k_m \quad k_x \quad k_y \quad k_m), \quad (24)$$

where $k_x = c_1k_m$, $k_y = c_2k_m$.

### 1.2.4 Determination of System Equation

Substituting Eqs. (6) to (24) into Eq. (5), the dynamic nonlinear differential equations can be expressed as:

$$\left.\begin{aligned} &m_1\ddot{X}_1 + c_{x_1}\dot{X}_1 + k_{x_1}X_1 + c_1k_m\delta_n = -c_mc_1\dot{\delta}_n \\ &m_1\ddot{Y}_1 + c_{y_1}\dot{Y}_1 + k_{y_1}Y_1 + c_2k_m\delta_n = -c_mc_2\dot{\delta}_n \\ &I_{z_1z_1}\ddot{\theta}_1 + k_m\delta_nr_{b1} = T_1 - c_m\dot{\delta}_nr_{b1} \\ &m_2\ddot{X}_2 + c_{x_2}\dot{X}_2 + k_{x_2}X_2 - c_1k_m\delta_n = -c_mc_1\dot{\delta}_n \\ &m_2\ddot{Y}_2 + c_{y_2}\dot{Y}_2 + k_{y_2}Y_2 - c_2k_m\delta_n = c_mc_2\dot{\delta}_n \\ &I_{z_2z_2}\ddot{\theta}_2 - k_m\delta_nR = -T_2 + c_m\dot{\delta}_nR \end{aligned}\right\}, \quad (25)$$

where $\delta_n = X_n - e(t), \dot{\delta}_n = \dot{X}_n - \dot{e}(t).$

## 2 VIBRATION EXCITATION OF SYSTEM

### 2.1 Stiffness

Meshing stiffness is composed of the average stiffness $k_{mm}$ and time-varying stiffness.

$$k_m(t) = k_{mm} + \sum_{i=1}^{n} k_i \cos(i\Omega_h t - \varphi_i). \tag{26}$$

The value of $k_i(t)$ is associated with contact ratio $\varepsilon$ and can be expressed as:

$$\begin{cases} k_i(t) = \dfrac{\sqrt{2-2\cos(2\pi i(\varepsilon_m - m))}}{i\pi} k_p \\ \varphi_i = \arctan \dfrac{1-\cos(2\pi i(\varepsilon_m - m))}{\sin(2\pi i(\varepsilon_m - m))} \\ k_p = k_{mm} / \varepsilon_m \end{cases}, \tag{27}$$

where $\varepsilon_m$ fits the monogenic harmonic function, which can be obtained as:

$$\varepsilon_m(\theta_1) = \varepsilon_{mm} + \sum_{i=1}^{n} \varepsilon_i \cos(i\theta_1 - \sigma_i). \tag{28}$$

As the stiffness of the bearing is highly sensitive to the load on the bearing in the radial direction, the selection of the adopted bearing stiffness is necessary. As a kind of non-circular gear, the curve-face gear is mainly applied in medium-low speed and low-load occasions. Specifically, the change of load has little effect on the stiffness. In this paper, the bearing stiffness is regarded as a constant, which can be obtained as:

$$k = \lim_{\substack{\Delta F_r \to 0 \\ \Delta\delta \to 0}} \frac{\Delta F_r}{\Delta\delta} = \frac{1}{n + m + m\ln F_r + 0.13CF_r^{-1.13}}, \tag{29}$$

where the basic parameters *m, n, C* and $F_r$ can be obtained from the reference [17].

### 2.2 The Driving Torque

Although the driving torque $T_2$ is constant, the driven torque $T_1$ of the curve-face gear is variable due to the time-varying transmission ratio. The relationship between the driving torque $T_2$ and the driven torque $T_1$ can be expressed as:

$$T_1 = (T_2 - I_2\alpha_2)/i_{12}, \tag{30}$$

where angular acceleration $a_2$ can be described as:

$$\alpha_2 = \frac{d\omega_2}{dt} = \frac{n_1 a\omega_1^2 k(1-k^2)\sin(n_1\omega_1 t)}{R(1-k\cos(n_1\omega_1 t))^2}. \tag{31}$$

The equivalent excitation force can be described as:

$$F_m(t) = \frac{T_1 I_{z2z2} r_{b1}(\theta_1) + I_{z1z1} R(T_2 - I_2\alpha_2)}{I_{z1z1}R^2 + I_{z2z2} r_{b1}^2(\theta_1)}. \tag{32}$$

## 3 DIMENSIONLESS DYNAMIC EQUATION

For curve-face gear, the value of $r(\theta_1)$ varies with the rotation angle $\theta_1$. That is, the base radius $r_{b1}$ of the non-cylindrical gear is not constant and the velocity of the static transmission error can be calculated as:

$$\begin{aligned} \dot{X}_n = &(\dot{X}_1 \cos a_n + \dot{r}_{b1}\theta_1 + r_{b1}\dot{\theta}_1) + \dot{Y}_1 \sin a_n - \\ &-(\dot{X}_2 \cos a_n + R\dot{\theta}_2) - \dot{Y}_2 \sin a_n. \end{aligned} \tag{33}$$

Let $\omega_n = \sqrt{k_{mm}/m_e}$, $\tau = \omega_n t$, $\omega_h = \Omega_h/\omega_n$; $x_j = X_j/b_m$; $y_j = Y_j/b_m$; $\lambda_n = X_n/b_m - e(\tau)$; $\vartheta_j = \theta_j/b_m$ and $e(\tau) = (e_0 + e_r\cos(\omega_h\tau + \phi_i))/b_m$.

Then, Eq. (25) can be dimensionless as:

$$\left.\begin{aligned} &\ddot{x}_1 + 2\zeta_{x_1}\dot{x}_1 + 2c_1\zeta_{m1}\dot{\lambda}_n + \kappa_{x_1}x_1 + c_1\kappa_{m1}\lambda_n = 0 \\ &\ddot{y}_1 + 2\zeta_{y_1}\dot{y}_1 + 2c_2\zeta_{m1}\dot{\lambda}_n + \kappa_{y_1}y_1 + c_2\kappa_{m1}\lambda_n = 0 \\ &\ddot{\vartheta}_1 + 2r_{b1}\zeta_{h1}\dot{\lambda}_n + r_{b1}\kappa_{h1}\lambda_n = \xi_1 \\ &\ddot{x}_2 + 2\zeta_{x_2}\dot{x}_2 - 2c_1\zeta_{m2}\dot{\lambda}_n + \kappa_{x_2}x_2 - c_1\kappa_{m2}\lambda_n = 0 \\ &\ddot{y}_2 + 2\zeta_{y2}\dot{y}_2 - 2c_2\zeta_{m2}\dot{\lambda}_n + \kappa_{y_2}y_2 - c_2\kappa_{m2}\lambda_n = 0 \\ &\ddot{\vartheta}_2 - 2R\zeta_{h2}\dot{\lambda}_n - R\kappa_{h2}\lambda_n = -\xi_2 \end{aligned}\right\}, \tag{34}$$

where $\omega_{ij} = \sqrt{k_{ij}/m_j}$; $\zeta_{ij} = c_{ij}/(2m_j\omega_n)$; $\zeta_{mj} = c_m/(2m_j\omega_n)$; $\kappa_{mj} = k_m(\tau)/(2m_j\omega_n)$; $\kappa_{hj} = k_m(\tau)/(2I_j\omega_n)$; $\kappa_{ij} = \omega_{ij}^2/\omega_n^2$; $\zeta_{hj} = c_m/(2I_j\omega_n)$; $(i = x, y, j = 1, 2)$.

## 4 SIMULATION AND ANALYSIS

As can be seen in Eq. (34), it is a higher-order nonlinear vibration system. In this paper, the bond-graph method was introduced to solve the dimensionless dynamic of differential equations. When the generalized coordinates, the parameter equation, the force input and the velocity conversion matrix (Eqs. (6) to (24)) are determined, the time history chart and phase diagram can be obtained, and the results are presented in the dimensionless form.

Due to the external excitation of the curve-face gear pair caused by eccentricity *k*, meshing frequency

$\omega_h$ and order $n_1$ of the non-cylindrical gear, a unique dynamic characteristic of curve-face gear system is produced as shown in Figs. 6 to 8.

**Table 1.** *Basic parameters of curve-face gear drive*

| Parameters | Curve-face gear |
|---|---|
| Module $m$ [mm] | 4 |
| Teeth of driving gear $z_1$ | 18 |
| Teeth of driven gear $z_2$ | 36 |
| Tooth width $B$ [mm] | 30 |
| Driven torque [Nm] | 700 |
| Weight of drive gear $m_1$ [kg] | 0.515 |
| Weight of driven gear $m_2$ [kg] | 1.673 |
| Rotational inertia $I_{z1z1}$ [kg·m²] | $3.5\times10^{-4}$ |
| Rotational inertia $I_{z2z2}$ [kg·m²] | $8.1\times10^{-3}$ |
| Meshing rigidity $k_{mm}$ [N·m⁻¹] | $8.1\times10^{8}$ |
| Meshing damping $c_m$ [N·s·m⁻¹] | $2.5\times10^{3}$ |
| Support stiffness $k$ [N·m⁻¹] | $k_{x1}=7.41\times10^{8}$; $k_{x2}=1.2\times10^{9}$; $k_{y1}=6.48\times10^{8}$; $k_{y2}=1.13\times10^{9}$ |
| Support damping $c$ [N·s·m⁻¹] | $c_{x1}=2.26\times10^{3}$; $c_{x2}=1.6\times10^{4}$; $c_{y1}=2.11\times10^{3}$; $c_{y2}=1.55\times10^{4}$ |

### 4.1 Dynamic Results by Eccentricity

Eccentricity $k$ is one of the main parameters that reflects the vibration response of the curve-face gear drive. Fig. 6 gives the results of gear vibration response in different eccentricity $k$.

Referring to 'time history chart' (Fig. 6), when the meshing frequency is constant, the number of vibration periods remains unchanged with eccentricity $k$. With the increase of eccentricity $k$, the vibration amplitude increases and the vibration period converts from harmonic-periodic to quasi-periodic motion. The main cause for this phenomenon depends on:

1) According to Eq. (34), $r_{b1}$ and $R$ are the main factors affecting the vibration response of the system. For the curve-face gear, $r_{b1}$ changes accordingly with the change of meshing frequency, which is different from the ordinary gear. This leads to a regular fluctuation of the normal load (or eccentric load) under the same load torque with the external excitation changes.
2) In addition to the influence of the meshing frequency, $r_{b1}$ and $R$ are also affected by eccentricity $k$ and the order number $n_1$ of non-cylindrical gear. The fluctuating range of $r_{b1}$ increases but the value of $R$ decreases with the rise of eccentricity $k$, which results in the increase of external excitation and the intention of vibration.

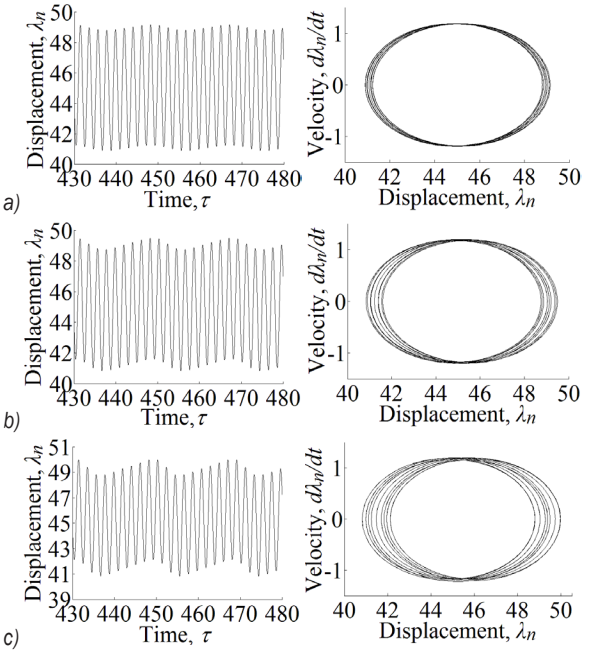


**Fig. 6.** *Influence of eccentricity on system response; time history chart and phase diagram for a) eccentricity $k=0.1$, b) eccentricity $k=0.2$, and c) eccentricity $k=0.3$*

As shown in the phase diagram (Fig. 6), the equilibrium positions of the curve-face gear shift backwards and forwards in the process of vibration: the equilibrium positions of vibration vary periodically with meshing time, and the value of the vibration amplitude rises with the increase of eccentricity $k$. The main reason is that the normal load (or eccentric load) between the tooth is affected by $r_{b1}$ and $R$. Under the excitation of meshing stiffness, the vibration displacement changes and thus the deviation of the equilibrium position changes correspondingly.

In conclusion, the dynamic performance tends to be better with the decrease of eccentricity $k$.

### 4.2 Dynamic Results by the Order $k_1$

As another significant factor of the vibration response of the curve-face gear drive, the different order number $n_1$ of non-cylindrical gear determine different dynamic performances as shown in Fig. 7.

As shown in the 'time history chart' (Fig. 7), when the meshing frequency is constant, the number of vibration periods remains unchanged with the order number $n_1$ of non-cylindrical gears. With the increase of the order number $n_1$, the vibration amplitude decreases and the fluctuation period increases from 1 to 3. The main reasons are as follows:

1) The change period of $r_{b1}$ increases, and the amplitude remains unchanged, which leads to the increase of the fluctuation period of vibration;
2) The vibration amplitude decreases as the value of $R$ increases and the order number $n_1$ increases.

As shown in the phase diagram (Fig. 7), the periodic change and main reason of the equilibrium positions are the same as in Fig. 6. However, the deviation of the equilibrium position remains constant and the number of the equilibrium positions decreases due to the changing rules of $r_{b1}$.

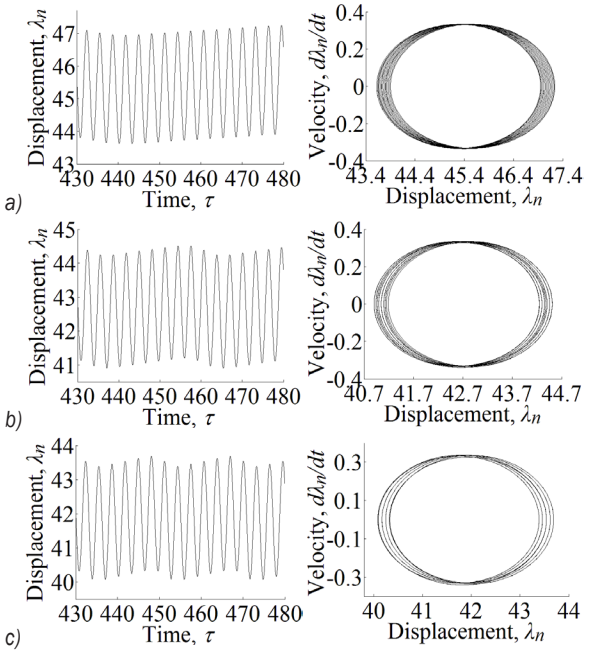


**Fig. 7.** *Influence of order on system response, time history chart, and phase diagram for: a) order $n_1 = 1$, b) order $n_1 = 2$ and c) order $n_1 = 3$*

In conclusion, the dynamic performance tends to be better with the increase of the order $n_1$.

### 4.3 Dynamic Results by Meshing Frequency

For various meshing frequencies, the dynamic response of curve-face gear drive shows different fluctuation amplitudes and equilibrium positions.

As shown in Fig. 8, when the meshing frequency increases, eccentricity $k$ and the order number $n_1$ are constant:

1) The number of vibration periods, the equilibrium positions and the vibration amplitude all increase, which is the same as the vibration of the face gear **[11]**;
2) The equilibrium positions vary periodically with meshing frequency since $r_{b1}$ changes accordingly with the change of meshing frequency.

For the vibration response of curve-face gear, while the meshing frequency increases, the change of value $r_{b1}$ affects the external excitation, inertia force and centrifugal force, which intensifies the vibration of the system. Consequently, the vibration performance of the curve-face gear is more complex than that of the face gear.

In this situation, both sides of the tooth surface will contact alternatively when the meshing frequency reaches a certain value. This is not allowed in the vibration response of the gear transmission system, which results in a limited meshing frequency of the curve-face gear.

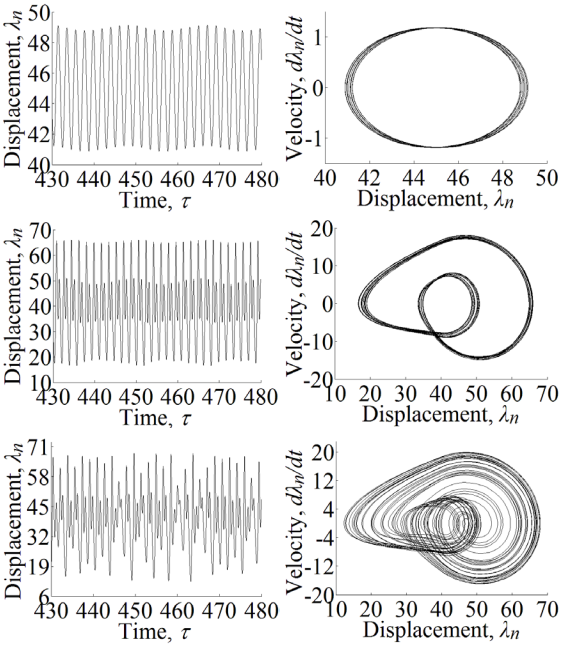


**Fig. 8.** Influence of meshing frequency on system response; time history chart and phase diagram for dynamic response when a) $\omega_h = 0.3$, b) $\omega_h = 0.35$ and c) $\omega_h = 0.3591$

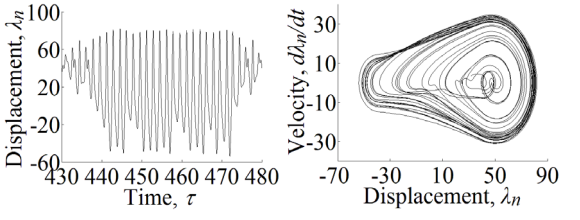


**Fig. 9.** *Dynamic response under limited speed; time history chart and phase diagram*

As shown in Fig. 9, when the meshing frequency is 0.378, the reverse contact appears. This reveals that

the gear will not work properly since the meshing frequency reaches the limited value. The meshing frequency can be converted to a limited speed of 790 rpm, which indicates that the curve-face gear is suitable for medium and low speed situations.

## 5 VALIDATION AND ANALYSIS

### 5.1 Theory Validation

When $k=0$, the curve-face gear can be degenerated into an ideal face gear. A harmonic response is shown by the time history chart and phase diagram (Fig. 10), which is the same as the existing conclusion of face gear [11]. This means that the dynamic equation not only can be applied to the dynamic analysis of curve-face gear, but also to face gear.

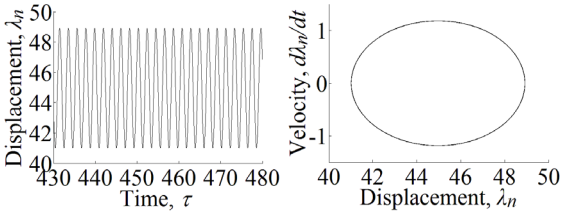


**Fig. 10.** *Theory validation, time history chart, and phase diagram*

The root cause lies in the fact that there is no essential difference between non-circular gears and conventional gears except for the difference of transmission ratio function. Thus, the impact of external excitation no longer exists.

### 5.2 Experiment Validation

The experiment is based on the transmission platform of the curve-face gear as shown in Fig. 11.

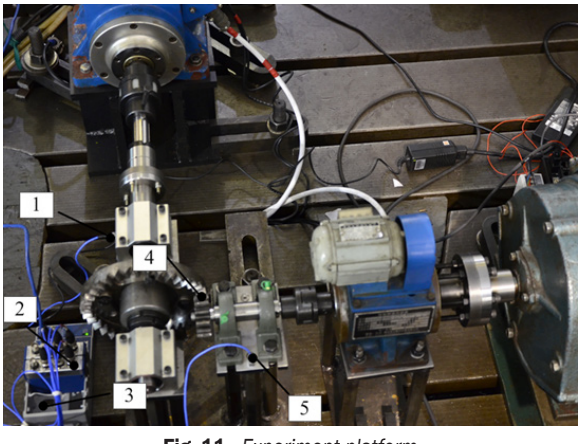


**Fig. 11.** *Experiment platform*

Dynamic signals can be acquired by measuring the vibration value along $X$, $Y$ and $Z$ directions on the bearing cap. No. 1 and 5 are acceleration sensors; No. 2 is the dynamic signal acquisition module; No. 3 is the Ethernet chassis. No. 4 is the simplified curve-face gear pair.

Since the acquisition process is affected by the interference of random signals, acquired data will be picked by some existing errors. To reduce the influence of the error on the experimental results, the data must be collected after certain processing. The changing rules of the vibration response along $X$ and $Y$ are the same. Therefore, the variation responses along $X$ in the meshing period were analysed as shown in Fig. 12.

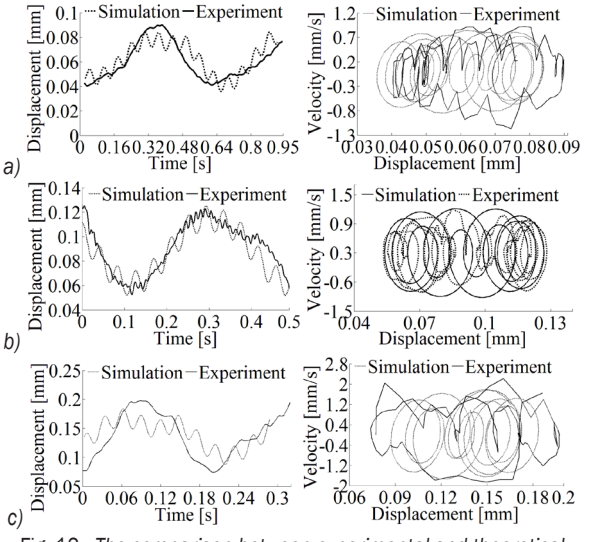


Fig. 12. *The comparison between experimental and theoretical data; time history chart and phase diagram for input velocity a) 200 rpm, b) 400 rpm, and c) 600 rpm*

The velocity signal (Fig. 12b) and displacement signal (Fig. 12a) can be transformed directly by the first and twice integral of the acceleration signal, separately.

The experimental results prove that:

1) when the meshing frequency is constant, the periodic fluctuation of the vibration response of the curve-face gear is more complex than that of the face gear due to the influence of the basic parameters of curve-face gear;
2) the comparison between experiment and simulation results demonstrates that the analytical results show good agreement with the related experimental data. It is reasonable to conclude that the experiment presents the validation of numerical model.

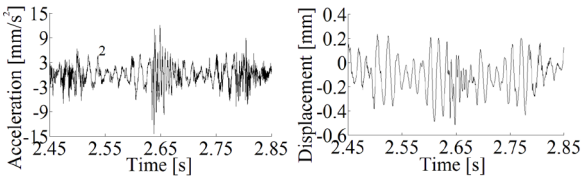


**Fig. 13.** *Experimental result under limited speed; vibration acceleration and time history chart*

For the validation of the limited speed of the curve-face gear, the vibration response can be obtained when the input speed is around 790 rpm, as shown in Fig. 13. The vibration displacement of the gear pair is negative, which indicates the reverse contact of the gear pair and will cause the destruction of the gear. Thus, the gear pair reaches the limit speed position, which represents the validation of the mathematical model.

## 6 CONCLUSIONS

1) A nonlinear dynamic model based on a Lagrange bond-graph was presented. The proposed method not only applies to the dynamic analysis of the curve-face gear, but also can be applied to the face gear.
2) The external excitation, caused by $r_{b1}$ and $R$ which are affected by the eccentric $k$ and the order $n_1$ of non-circular gear, is the main factor affecting the vibration response of curve-face gear. The research results show that reducing the eccentricity and raising the order number $n_1$ will improve the dynamic characteristics of system.
3) The vibration response of the curve-face gear is also affected by the meshing frequency. However, due to the influence of external excitation, which will exacerbate the vibration, the limited meshing frequency of the curve-face gear is lower than that of the face gear. These characteristics determine that the gear cannot be applied to the transmission system with high speed.
4) The experiment results are in good agreement with the theory analysis of the models. It is reasonable to conclude that the model presented is capable of efficiently simulating the vibration response of the curve-face gear.

## 7 ACKNOWLEDGMENT

This work supported by Research Program supported by from the National Natural Science Foundation (51275537), China and Graduate Student Research Innovation Project (No. CYB15019).

## 8 NOMENCLATURES

$R$ the radius of curve-face gear, [mm]
$r(\theta_1)$ the polar radius of non-cylindrical gear, [mm]
$k$ eccentricity
$n_1$ the order number of non-cylindrical gear
$n_2$ the order number of curve-face gear
$a$ semi major axis of ellipse, [mm]
$F_I$ D 'Alembert force, [N]
$\tau_I$ inertia force, [N]
$F_K$ elastic force, [N]
$F_S$ input force, [N]
$F_R$ dissipative force, [N]
$F_k$ elastic force caused by gear comprehensive error, [N]
$F_r$ dissipative force caused by gear comprehensive error, [N]
$T_I$ comprehensive velocity transform matrix in inertial field
$q_G$ displacement vector in generalized coordinates system
$I$ mass matrix in inertial field
$T_W$ transform matrix of angular velocity in inertial field
$C_C$ rotation matrix in inertial field
$I_C$ inertia matrix in inertia field
$T_K$ velocity transform matrix in elastic field
$K$ stiffness matrix
$T_R$ velocity transform matrix in damping field
$R$ damping matrix
$T_S$ velocity transform matrix in potential source
$\tau_S$ input force vector
$T_k$ velocity transform matrix of gear comprehensive error in elastic field
$K_e$ stiffness matrix of gear comprehensive error
$e_t$ gear comprehensive error vector
$T_r$ velocity transform matrix of gear comprehensive error in damping field
$R_e$ damping matrix of gear comprehensive error
$T_1$ driving torque, [N·m]
$T_2$ driven torque, [N·m]
$\alpha_n$ pressure angle of curve-face gear, [°]
$r_{b1}$ base radius of non-cylindrical gear, [mm]
$T_V$ translational transform matrix in inertial field
$T_W$ angular velocity transform matrix in inertial field
$E$ unit vector
$k_m$ meshing stiffness, [N·m$^{-1}$]
$k_{mm}$ average meshing stiffness, [N·m$^{-1}$]
$\Omega_h$ gear meshing frequency
$\varepsilon_m$ time-varying contact ratio
$\varepsilon_{mm}$ average contact ratio
$\sigma_i$ initial phase
$\varepsilon_i$ $i$-order time-varying contact ratio

$\omega_n$ nominal simulating frequency
$b_m$ the normal backlash, [mm]
$\eta_j$ nominal displacement (angle) $j = (x, y, \vartheta, \lambda)$
$\tau$ nominal time
$e(t)$ dimensionless comprehensive error
$\omega_h$ dimensionless simulating frequency

## 9 REFERENCES


[1] Lin, C., Gong, H., Nie, N., Zen, Q., Zhang, L. (2012). Geometry design, three-dimensional modeling and kinematic analysis of orthogonal fluctuating gear ratio face gear drive. *Proceedings of the Institution of Mechanical Engineers, Part C: Journal of Mechanical Engineering Science*, vol. 227, no. 4, p. 779-793, **DOI:10.1177/0954406212453382**.

[2] Litvin, F.L., Wang, J.-C., Bossler, R.B., Chen, Y.-J., Heath, G., Lewicki, D.G. (1994). Application of face-gear drives in helicopter transmissions. *Journal of Mechanical Design*, vol. 116, no. 3, p. 672-676, **DOI:10.1115/1.2919434**.

[3] Lin, C., Cai, Z. (2015). Modeling of dynamic efficiency of curve-face gear pairs. *Proceedings of the Institution of Mechanical Engineers, Part C: Journal of Mechanical Engineering Science*, vol. 230, no. 7-8, p. 1209-1221, **DOI:10.1177/0954406215623308**.

[4] Mohammed, O.D., Rantatalo, M., Aidanpää, J.-O. (2015). Dynamic modelling of a one-stage spur gear system and vibration-based tooth crack detection analysis. *Mechanical Systems and Signal Processing*, vol. 54-55, p. 293-305, **DOI:10.1016/j.ymssp.2014.09.001**.

[5] Mohammed, O.D., Rantatalo, M., Aidanpää, J.-O., Kumar, U. (2013). Vibration signal analysis for gear fault diagnosis with various crack progression scenarios. *Mechanical Systems and Signal Processing*, vol. 41, no. 1-2, p. 176-195, **DOI:10.1016/j.ymssp.2013.06.040**.

[6] Sawalhi, N., Randall, R.B. (2014). Gear parameter identification in a wind turbine gearbox using vibration signals. *Mechanical Systems and Signal Processing*, vol. 42, no. 1-2, p. 368-376, **DOI:10.1016/j.ymssp.2013.08.017**.

[7] Khabou, M.T., Bouchaala, N., Chaari, F., Fakhfakh, T., Haddar, M. (2011). Study of a spur gear dynamic behavior in transient regime. *Mechanical Systems and Signal Processing*, vol. 25, no. 8, p. 3089-3101, **DOI:10.1016/j.ymssp.2011.04.018**.

[8] Karnopp, D. (1977). Lagrange's equations for complex bond graph systems. *Journal of Dynamic Systems, Measurement, and Control*, vol. 99, no. 4, p. 300-306, **DOI:10.1115/1.3427123**.

[9] Shen, Y., Yang, S., Liu, X. (2006). Nonlinear dynamics of a spur gear pair with time-varying stiffness and backlash based on incremental harmonic balance method. *International Journal of Mechanical Sciences*, vol. 48, no. 11, p. 1256-1263, **DOI:10.1016/j.ijmecsci.2006.06.003**.

[10] Litak, G., Friswell, M.I. (2005). Dynamics of a gear system with faults in meshing stiffness. *Nonlinear Dynamics*, vol. 41, no. 4, p. 415-421, **DOI:10.1007/s11071-005-1398-y**.

[11] Lin, T., Ran, X. (2012). Nonlinear vibration characteristic analysis of a face-gear drive. *Journal of Vibration and Shock*, vol. 31, no. 2, p. 25-31. (in Chinese)

[12] Li, X., Zhu,R., Li Z. (2013). Analysis of coupled vibration of face gear drive with non-orthogonal. *Journal of Central South University (Science and Technology)*, vol. 44, no. 6, p. 2274-2280.

[13] Wang, A., Ma,Q., Liu, L. (2006). Modeling and Simulation of Ellipse Gears. *Journal of Mechanical Transmission*, vol. 30, no. 4, p. 7-10. (in Chinese)

[14] Chen,Y., Hu,Q., Luo, L. (2009). Research on a novel transmission mechanism based on the principle of space curve mesh. *Journal of Mechanical Transmission*, vol. 33, no. 2, p. 1-4. (in Chinese)

[15] Arakawa, A. (1995). Contact ratio of noncircular gears. *Transactions of the Japan Society of Mechanical Engineers Series C*, vol. 61, no. 585, p. 2093-2099, **DOI:10.1299/kikaic.61.2093**. (in Japanese)

[16] Lin, C., Liu, Y., Gu, S. (2014). Analysis of nonlinear twisting vibration characteristics of orthogonal curve-face gear drive. *Journal of the Brazilian Society of Mechanical Sciences and Engineering*, vol. 37, no. 5, p. 1499-1505, **DOI:10.1007/s40430-014-0296-y**.

[17] Wu, H., Wang, J., An, Q. (2008). Study on the calculating method of radial stiffness of tapered roller bearing. *Lubrication Engineering*, vol. 33, no. 7, p. 39-43.

Strojniški vestnik - Journal of Mechanical Engineering 63(2017)3, 171-180

DOI:10.5545/sv-jme.2016.3968
Original Scientific Paper
Received for review: 2016-08-19
Received revised form: 2017-01-18
Accepted for publication: 2017-01-31

# Efficiency Improvement of Agricultural Winch Machines

Martin Kodrič[1] – Jože Flašker[2] – Stanislav Pehan[2]
[1] Krško Nuclear Power Plant, Slovenia
[2] University of Maribor, Faculty for Mechanical Engineering, Slovenia

*In this article the problems with the use of the common winch cart on very steep terrain planted with permanent crops are described, especially with regard to energy losses. A hypothesis is developed regarding the improved use of the potential energy that leads to the development of a new economical hydraulic machine. A transmission of the new agricultural tractor that can use the much bigger share of the effective potential energy is conceived in rough principles. A portable flatbed improves the total efficiency. A comparable analysis on very different sloped terrains is presented to argue for the greater efficiency of the new machine. The yearly fuel quantity saving by using the new hydraulic machine on the sloping terrain with realistic topography is 36 % in comparison to the winch cart. Decisional limits about the minimum internal combustion engine power are discussed.*

**Keywords: sloped terrain, permanent crop treatments, hydraulic tractor, crop treatment efficiency**

**Highlights**
- *The effective replacement for winch cart is designed and analyzed.*
- *The proposed computing procedure enables rough estimation of competitive machines.*
- *The new machine returns potential energy back to useful energy.*
- *The new machine enables big saving in fuel and labor time.*
- *The efficiency of the crop treatment is introduced.*

## 0 INTRODUCTION

To treat the agriculture terrain planted with permanent crops and inclined at angles greater than 60 % winch power is required. Working on such terrain with conventional agriculture tractors, even equipped with caterpillar treads, is a dangerous venture and is often impossible due to the weak traction forces on the sloped terrain (slip). Working on steep inclines with ordinary tractors frequently results in accidents [1]. Treatment of the permanent crops on the sloped terrain requires about twenty-four executions per year.

In recent years, many comprehensive studies about treating slope agriculture terrains have been made [2] to [4]. Probably the most influential one is by a German author [5] who determined the basic limits of the usability of different agricultural tractors and machines; this is considered to be the base understanding, Fig. 1.

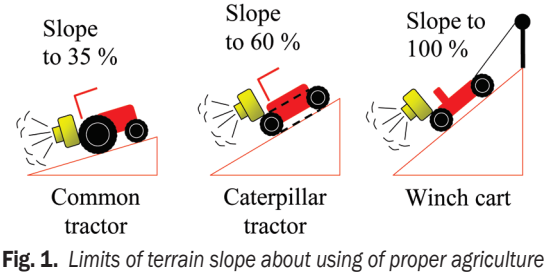


**Fig. 1.** *Limits of terrain slope about using of proper agriculture tractor or machine*

The usage of tractors and agricultural machinery on slopes with different inclines is described in the references [6] to [8]. The great issue with ordinary tractors is their stability when working on steep terrain [9].

The current machine considered appropriate for agiculture treatment on a very sloped terrain is a cart driven by the winch that is firmly placed on the top of the slope. Such a cart has its own engine for powering accessories. The winch located on the flat reef can be driven by a tractor propeller shaft or has its own engine. When the cart is sliding downwards on the slope, only one accessory can be active. Afterwards, with the rope anchored on the flat reef, the cart is pulled upwards. In this stroke, all accessories are switched off, Fig. 2. Consequently, this type of treatment leads to long processing time and is significantly more expensive than the treatments on the flatter terrains. The treatment time is often decisive [10] and [11].

Special care should be devoted to the enormous amount of energy consumed. In addition to higher fuel costs, there are also greater $CO_2$ emissions and higher expenses for harvesting in general. Consequently, farmers who use the described technology cannot be competitive on the market. The focus of this paper is to indicate the basic problems of current technology for treating sloped terrains and to show ways to solve them in order to reduce energy and labour costs.

*Corr. Author's Address: University of Maribor, Faculty for Mechanical Engineering, Smetanova ulica 17, 2000 Maribor, Slovenia, stanislav.pehan@um.si

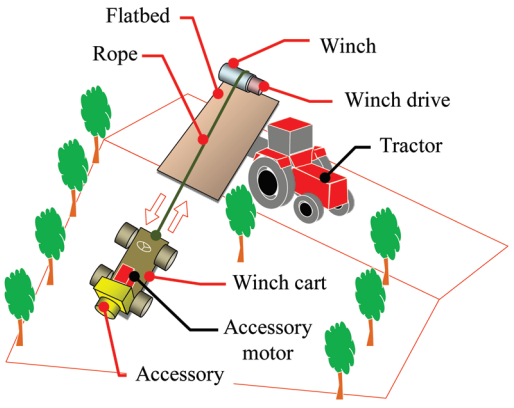


**Fig. 2.** *Basic working principle by using winch cart*

## 1 THE ENERGY LOSSES FOR THE TREATMENT OF FLAT AND SLOPED TERRAINS

For the winch cart, the first energy loss is the one that occurs due to not using potential energy during the downward stroke of the winch cart. The second energy loss is inherent to the basic working principle in which it is evident that one of two strokes is useless for using the accessories. Under the assumption that the downward stroke is the working stroke for the accessories, the upward stroke is a waste of time and energy. The upward stroke should be performed to reposition the winch cart on the top of the slope, along the flat reef, to make a longitudinal relocation of the cart, Fig. 3.

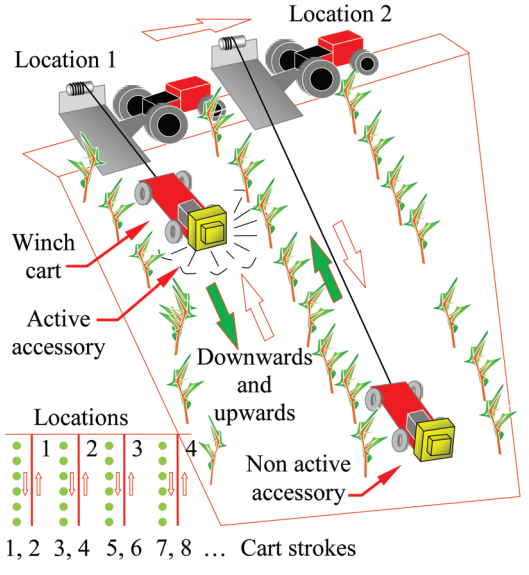


**Fig. 3.** *Basic treatment principle on terrains inclined more than 60 %*

The working principle of the treatment (probably of the same crops) by using a common agricultural tractor on the terrains sloped less than 60 % is much more rational [12]. Each part of the tractor path is maximally effective with all accessories fully active all the time, Fig. 4.

To illustrate the problem of excessive energy consumption on sloped agricultural terrain, a few different cases are carried out. The energy needed for the movement on varied terrain inclined by 0 %, 35 %, 60 % and 100 % are compared, Table 1. The length of the machine path is 100 metres. To obtain comparable data, all relevant vehicles characteristics are identical, including vehicles mass, rolling resistance and moving velocities. The vehicles characteristics correspond to the average tractors [2].

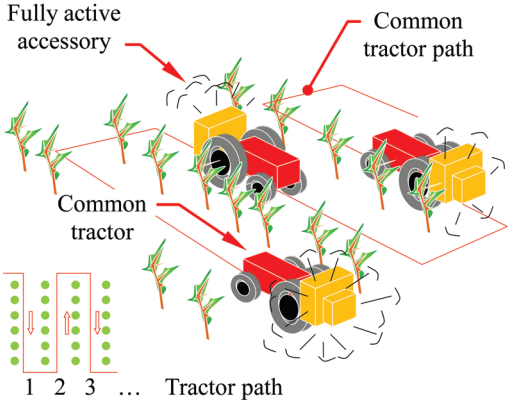


**Fig. 4.** *Basic treatment principle on terrains inclined less than 60 %*

**Table 1.** *Data for the movement the machine equipped with the mower in one stroke (upwards)*

| Machine | Common or caterpillar tractor | | | Winch cart |
|---|---|---|---|---|
| Terrain slope [%] | 0 | 35 | 60 | 100 |
| Energy for climbing up [MJ] | 0.48 | 1.00 | 1.31 | 1.71 |
| Power for climbing up [kW] | 6 | 11 | 15 | 19 |
| Potential energy [MJ] | 0 | 0.04 | 0.28 | 0.63 |
| Potential power [kW] | 0 | 0.5 | 3 | 7 |

The data in the Table 1 are calculated according to the Eqs. (1) to (7).

$$R_f = f_r \cdot m \cdot \cos\alpha \cdot g, \quad (1)$$

$$R_S = m \cdot \sin\alpha \cdot g. \quad (2)$$

where $R_f$ is rolling resistance, $R_S$ is slope resistance, α is terrain slope, m is a total mas of tractor or cart equipped with accessories and with driver ($m_T$ = 1300 kg is tractor or winch cart net weight [2], $m_D$ = 85 kg

is driver weight, $m_{mu}$ = 105 kg is mower weight [13]) and $f_r$ = 0.25 is rolling resistance coefficient [14].

For $R_{up}$ and $R_{down}$ see Eqs. (13) and (14).

$$W_{up} = R_{up} \cdot s, \tag{3}$$

$$W_{down} = R_{down} \cdot s, \tag{4}$$

$$P_{up} = \frac{W_{up}}{t}, \tag{5}$$

$$P_{down} = \frac{W_{down}}{t}, \tag{6}$$

$$t = \frac{s}{v_{av}}, \tag{7}$$

where $W_{up}$ is energy for climbing up, $W_{down}$ potential energy, $P_{up}$ power for climbing up, $P_{down}$ potential power, $t$ labour time, $v_{av}$ = 4 km/h average tractor speed [15] and $s$ length of the path.

When analysing the data gathered in Table 1, it is evident that the slope resistance is the most significant factor. To overcome the slope and rolling resistance, a winch cart needs only 3.5 times greater energy in comparison to the same vehicle moving on the flat terrain. It is also significant that potential energy theoretically rises with the terrain slope, but in fact remains unused. No winch cart currently on the market uses this potential energy.

The energy needed for treating the flat and sloped terrain are calculated (Table 2). The length of the crop line is 100 metres. The first accessory is the rotary mower; the second is the sprayer. With the use of the winch cart, the number of the strokes are doubled in comparison to the common tractor.

**Table 2.** *Data for the treatment two columns of crops on different sloped terrains by using two accessories separately*

| Machine | Common or caterpillar tractor | | | Winch cart |
|---|---|---|---|---|
| Terrain slope [%] | 0 | 35 | 60 | 100 |
| Energy for treating [MJ] | 5.10 | 7.00 | 7.30 | 10.00 |
| Fuel [l] | 0.42 | 0.58 | 0.61 | 0.83 |
| Efficiency [%] | 62 | 46 | 43 | 32 |
| Labour time [h] | 0.1 | 0.1 | 0.1 | 0.2 |

$m_{Sp}$ = 85 kg; sprayer weight [13], $P_M$ = 12 kW; mower power [13] and $P_{Sp}$ = 6 kW; sprayer power [13].

To obtain comparable results as presented in Table 2, the main characteristics of agricultural machines are the same; the same are also valid for the accessories. The enormous amount of energy needed for running accessories on the sloped terrain is a matter of concern, as is the fact that it takes twice as much time to do the work.

In Table 3, the results for the treatment of one hectare of crops per year are presented. The same shape of the field with the same number of crop lines is assumed. The machines have the same weight, and they are equipped with the same accessories.

The data in Tables 2 and 3 are calculated by using the Eqs. (1) to (4), Eqs. (8) to (10), (13), (14) and (17).

**Table 3.** *Data for treating one hectare of agricultural terrain per year with all accessories for tractors and winch cart*

| Machine | Common or caterpillar tractor | | | Winch cart |
|---|---|---|---|---|
| Terrain slope [%] | 0 | 35 | 60 | 100 |
| Energy for treating [MJ] | 1458 | 1488 | 1535 | 2971 |
| Fuel [l] | 121 | 123 | 127 | 247 |
| $CO_2$ emission [kg] | 313 | 319 | 329 | 651 |
| Labour time [h] | 30 | 30 | 30 | 60 |
| Efficiency [%] | 62 | 61 | 59 | 30 |

$P_{Msp}$ = 5 kW; manure spreader power [16], $P_{SideCt}$ = 9 kW; side cutter power [17], $P_{SCt}$ = 9 kW; spring cutter power [18], $m_{Msp}$ = 180 kg; manure spreader weight [16], $m_{SideCt}$ = 170 kg; side cutter weight [17], $m_{SCt}$ = 170 kg; spring cutter weight [18], and $m_{Cont}$ = 150 kg; and container for harvest weight.

In one year, 24 treatments of the terrain should be done: ten times with the mower, ten times with the sprayer, and once per year with all other accessories. The steepest terrain is treated with the winch cart technology; the other terrains are treated with common agriculture tractors. The results from Table 3 again show that the enormous energy consumption on the steep terrains.

## 2 ECONOMICAL HYDRAULIC MACHINE CONCEIVING

From the presented rough energy and labour time consumption analysis, it is obvious that a great opportunity exists for efficiency improvements of the winch cart. To make a step forward, an entirely new product, a new economical hydraulic (EH) machine, for treating the most difficult terrains, is conceived, designed, and made in a prototype version. The machine's design and operating method lend themselves to reducing treatment costs [19]. The energy transformation takes into account the proven design [20]. The most obvious characteristic of the new EH machine is its drive: a purely conventional internal combustion (IC) diesel engine adapted to the inclination of the terrain by its free tilting, which ensures adequate lubrication. The IC engine runs a hydraulic pump that is connected by hydraulic

piping with hydraulic motors on wheels, winch, and accessories. The power transmission from the winch to the hydraulics pump is designed according to the already proven rules [21] and [22] and general procedures of design [23]. All hydraulic motors are controlled by a central control unit, Fig. 5. The IC engine is designed to give the minimum necessary power needed for the sloped terrain treatment. This enables the minimal dimensions and lowest weight of the new EH machine. Weight is reduced to the lower strength limit where the machine still operates [24] and [25]. When this machine is lowered down the slope the potential energy is converted into the mechanical energy for the accessories. Consequently, two accessories can be connected to the machine instead of one.

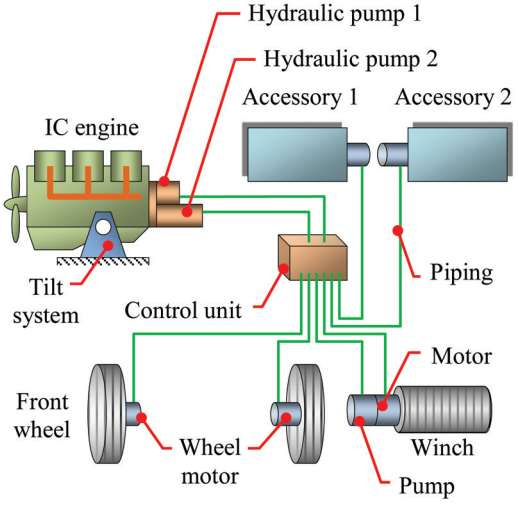


**Fig. 5.** *Hydraulic components of the modest tractor*

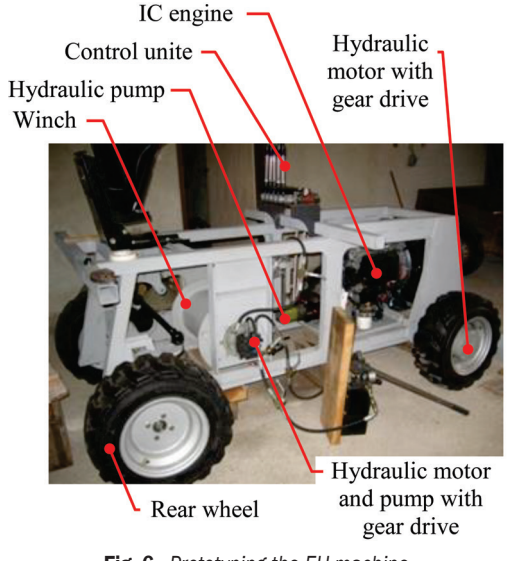


**Fig. 6.** *Prototyping the EH machine*

Since this machine is self-propelling, it has a significantly wider scope than ordinary winch carts with accessories only and no self-drive system. The next obvious advantage of the new EH machine is its ability to use both systems of the drive: the wheels and winch. No additional tractor is required for coming up steep terrains. Even though the new EH machine has a dual drive is suitable due to the low weight carrying out the common farm work on nearly flat terrains.

The new EH machine is conceived in real and prototyped already to the final stage, equipped with all components, Fig. 6.

The new EH machine is equipped with the rope winch at its rear. The rope is firmly anchored on the top of the terrain. With the upwards movement of the hydraulic machine, both drive systems (wheels and winch) function simultaneously. In the case of bad wheel grip due to the slippery terrain, the smart control system redirects the power to the winch drive.

In the case of terrain/rope contact, as presented in Fig. 7, the rope will no harm the terrain because it is not moving along its length. In comparison to the winch cart with the winch on the top of the terrain, this is likely a significant improvement. To avoid unnecessary friction, the rope is released as it is needed.

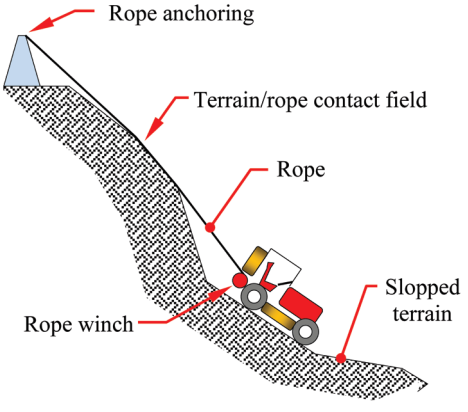


**Fig. 7.** *Terrain/rope contact situation*

To run both accessories, the sprayer and mower, the new EH machine has two built-in output drives: one is positioned on the front and the other on the rear of the vehicles. Two output drives ensure simultaneous but independent use of both accessories. The energy for one accessory comes directly from the IC engine, but the other accessory can obtain the necessary energy from the potential energy of the new EH machine traveling downhill. When the vehicle is moving downhill, both accessories can be active. When it is moving uphill, both accessories are

excluded, and all the IC engine power for moving the vehicle is available.

Using the potential energy, that is coming from the descending new EH machine for powering the accessories, saves time and energy. If the potential energy does not cover the needs of accessories, additional energy comes from the IC engine.

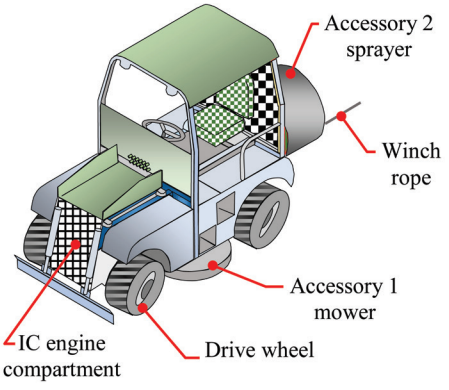


**Fig. 8.** *The new EH machine*

In Fig. 8, the new EH machine is presented. The main advantage of it is the free flow of the energy. Both the IC engine and winch rope can become a source of power that can run the accessories. The hydraulic pump on the winch can transform the potential energy of the descending machine into the pressure and flow of the hydraulic oil, which are directly used for running the accessories.

### 2.1 Portable Flatbed Design

To move the new EH machine from one crop line to the next, a self-propelled portable flatbed is provided that would be attached to the anchor line. Therefore no additional tractor is required to do this work.

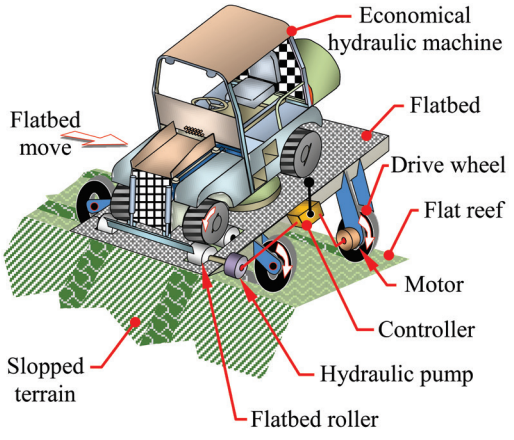


**Fig. 9.** *Working portable flatbed*

After the new EH machine is on the portable flatbed, Fig. 9, the vehicle front wheels are in contact with the driving rollers of the flatbed. The rollers drive the system that hydraulically moves the portable flatbed along the flat reef of the terrain [26].

## 3 EFFICIENCY OF THE NEW ECONOMICAL HYDRAULIC MACHINE

Sample calculations are done for one hectare of terrain, on which 24 treatments are considered. The treatments are 10 times of mowing, 10 times of spraying, one -time of scoring, one -time of fertilizing, one -time of peak cutting and one -time of harvesting crops.

### 3.1 Constant Sloped Terrain

The slopes of the terrain are chosen 0 %, 35 %, 60 % and 100 %. For the steeped slope the new EH machine is used with added technology for using the potential energy, which enables merging two treatments, such as mowing and spraying. That fact leads to the reduction of the number of the vehicle drives per year, from 24 to 14 with the use of the new EH machine on the 100 % slope.

The labour time for using the new EH machine is 20 % longer than for the treatments on the other slopes due to the four treatments in which the winch tractor should not move along the terrain when the vehicle is at the bottom of the terrain. For the treatments of the first three slopes, a standard tractor, which can simply turn around at the end of each column, is assumed. In comparison with Table 3, in Table 4 only the fourth column is different. Instead of the cart the new EH machine is analyzed. The fuel consumption of this machine is only slightly higher comparing with the tractors which process nearly flat farm fields.

**Table 4.** *Data for treatment one hectare of agricultural terrain per year with all accessories*

| Machine | Common or caterpillar tractor | | | New EH machine |
|---|---|---|---|---|
| Terrain slope [%] | 0 | 35 | 60 | 100 |
| Energy for treating [MJ] | 1458 | 1488 | 1535 | 1763 |
| Fuel [l] | 121 | 123 | 127 | 146 |
| $CO_2$ emission [kg] | 313 | 319 | 329 | 386 |
| Labour time [h] | 30 | 30 | 30 | 35 |
| Efficiency [%] | 62 | 61 | 59 | 51 |

In Table 5, the use of a winch cart and the newly designed EH machine are compared for very steep terrain (100 %).

**Table 5.** *Treatment of one hectare 100 % slope terrain per year with all accessories*

| | Winch cart | New EH machine |
|---|---|---|
| Total Energy [MJ] | 2971 | 1763 |
| Total Fuel [l] | 247 | 146 |
| $CO_2$ emission [kg] | 651 | 386 |
| Labour time [h] | 60 | 35 |
| Efficiency [%] | 30 | 51 |

The efficiency of the crop treatment is calculated according to the equation:

$$\eta = \frac{W_{acc}}{W_{acc} + W_{trac}}, \tag{8}$$

where $\eta$ is efficiency of the crop treatment, $W_{acc}$; energy needed for the accessories; and $W_{trac}$; energy needed for the machine drive.

Fuel consumption is calculated with the equation:

$$Q_{Fuel} = \frac{W_{Total}}{c} \cdot \frac{1}{\eta_{IC}}, \tag{9}$$

where $Q_{Fuel}$ is total fuel used, $W_{Total}$ total energy used, $c$=41.2 MJ/kg heating value of fuel [27], and $\eta_{IC}$=0.35 efficiency of internal combustion engine [2].

Carbon dioxide emission is calculated with the equation:

$$CO2_{emiss} = f_{CO2} \cdot Q_{Fuel}, \tag{10}$$

where $CO2_{emiss}$ [kg] is carbon dioxide emission, and $f_{CO2}$ = 3.16 carbon dioxide emission coefficient [28].

According to the Table 5 all advantages are on the side of the newly developed EH machine, especially the efficiency of the crop treatment, which is 70% better comparing with the common cart driven by winch. Above statements are additional confirmed with the procedure based on the neural networks [29] to [31], which is specially designed to predict crop treatment efficiency, fuel consumption, the level of $CO_2$ emissions and the time taken for the treatment of agricultural land [26].

### 3.2 Squared Terrain with Realistic Topography

In the preliminary subchapter, the constant slope of the whole terrain is assumed. To describe the agriculture terrain on which crops can be found in real circumstances, a matrix is made for which the individual slopes of increments are specified. The terrain is simplified by considering the following assumptions:

- the outer border of the terrain is square with sides 100 m long.
- each stroke is 100 m long.
- the distance between the crop columns is assumed to be 2 m. Therefore, 50 strokes are needed to treat the whole terrain.
- each stroke is divided into ten segments of slope. The slope of the individual segment is an independent data point and represents the average. This characteristic is represented by one column in the matrix.
- the matrix that describes such terrain consists of 10 rows and 50 columns.

The very likely matrix of the realistic topography could look like this:

$$\mathbf{M}_{Slope} = \begin{bmatrix} 44 & 43 & & 33 & 32 \\ 44 & 43 & & 32 & 32 \\ 43 & 43 & \dots & 31 & 31 \\ 42 & 42 & & 30 & 30 \\ 42 & 41 & & 30 & 29 \\ 41 & 41 & & 29 & 28 \\ 41 & 41 & & 29 & 28 \\ 41 & 40 & \dots & 27 & 27 \\ 40 & 39 & & 27 & 27 \\ 38 & 38 & & 27 & 27 \end{bmatrix}.$$

Each number in the matrix represents the segment slope in degrees. The terrain specified in the matrix is presented in Fig. 10.

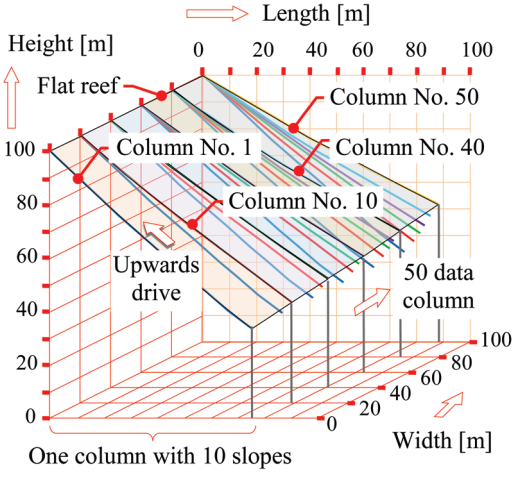


**Fig. 10.** *Presentation of the one hectare of terrain with realistic topography*

Driving resistances are calculated according to the following two equations:

$$R_f = f_r \cdot \left(m_T + m_D + m_M + m_S\right) \cdot \cos\alpha_{m,n} \cdot g, \quad (11)$$

$$R_S = \left(m_T + m_D + m_M + m_S\right) \cdot \sin\alpha_{m,n} \cdot g, \quad (12)$$

where $R_f$ is rolling resistance for segment $s_{m,n}$; $R_s$ slope resistance for segment $s_{m,n}$; $\alpha_{m,n}$ slope of the segment $s_{m,n}$; $s_{m,n}$ segment in row $m$ = 1 to 10 and column $n$ = 1 to 50.

The total resistance that acts during the moving of the vehicle equipped with two accessories upwards the sloped terrain is the sum of rolling and slope resistances. The applicable resistance that acts during the moving the same vehicle downwards is the difference of those individual resistances that are described with the equations:

$$R_{up} = R_S + R_f, \quad (13)$$

$$R_{down} = R_S - R_f, \quad (14)$$

where $R_{up}$ is applicable resistance at upwards drive and $R_{down}$ applicable resistance at downwards drive.

To obtain the consumed energies needed to overcome a sloped segment up- or down-wards, the resistances are multiplied by the length of the segment that is $c$ = 10 m because of the simplicity introduced.

$$W_{up} = R_{up} \cdot c, \quad (15)$$

$$W_{down} = R_{down} \cdot c, \quad (16)$$

where $W_{up}$ is applicable energy at upwards drive, and $W_{down}$ an applicable energy at downwards drive.

The total time, $t_{total}$, needed for the one treatment of the agricultural terrain is calculated with the equation:

$$t_{total} = \frac{2 \cdot 50 \cdot 100 \cdot \mathrm{m}}{v_{av}}. \quad (17)$$

The numeral 2 represents the number of vehicle strokes for each line of crops. The numeral 50 is equivalent to the crop lines or number of columns; 100 m is the terrain length of the crop column, Fig. 10.

The number of accessories, one or two, that can be functioning during the vehicle's downward drive, depends on the vehicle type. With the respect to the fact that the tractor power is very close to the minimum needed for the drive upwards, only one accessory can be used in case of the vehicle descending. In the case of a machine that can exploit the available potential energy, two accessories can be active simultaneously.

Technology that would be able to transform the potential energy for running the accessories cannot be derived mechanically for many reasons. The obvious one is the incorrect ratio between the wheels and accessories. A gearbox that would change this ratio freely would be necessary. The only way to accomplish this in financially feasible manner is the introduction of a hydraulic transmission. This has to be modified for this situation. In the continuation, two hydraulic agricultural machines are considered; the first one with only a basic hydraulic and the second one, called new EH machine, which is modified. Only the latter machine enables the simultaneous use of both accessories.

In Tables 6 and 7, data are presented that enable estimating the type of the machine. The data collected in the Table 6 describe the situation on one hectare of terrain treatment with two accessories only. The data in Table 7 represent the situation over the year.

The data in the Tables 6 and 7 are calculated on the basis of slopes delivered in $\mathbf{M}_{Slope}$ matrix and by using already explained equations (from 1 to 17).

**Table 6.** *Data for treating one hectare of real agricultural terrain per year – two accessories*

| | Winch cart | New EH machine |
|---|---|---|
| Energy for treating [MJ] | 2310 | 1388 |
| Fuel [l] | 192 | 115 |
| $CO_2$ emission [kg] | 506 | 304 |
| Labour time [h] | 50 | 25 |
| Efficiency [%] | 35 | 58 |

**Table 7.** *Treatment of one hectare of real agricultural terrain per year – all accessories*

| | Winch cart | New EH machine |
|---|---|---|
| Total Energy [MJ] | 2729 | 1743 |
| Total Fuel [l] | 227 | 145 |
| $CO_2$ emission [kg] | 598 | 382 |
| Labour time [h] | 60 | 35 |
| Efficiency [%] | 33 | 52 |

On the basis of the data in the previous two tables, it can be concluded that the new EH machine with modified hydraulic transmission demonstrates some obvious advantages. The savings in energy, fuel, emission and consumed labour time are obvious and doubtless cover the higher expenses of purchasing the equipment.

## 4 ESTIMATING THE TERRAIN FOR NEW ECONOMICAL HYDRAULIC MACHINE APPLICABILITY

The nominal power of the EH machine should be as low as possible. First condition: the new EH machine equipped with the heaviest accessories should be

driven upwards with the speed of about 4 km per hour. Second condition: when descending, the EH machine should have enough power to overcome the driving resistances and to run the two accessories. When descending the EH machine is using the energy of the IC engine and the potential energy.

A critical situation would occur at the moment the total power would not be enough to run both accessories at their maximum power. From the known data about the IC engine power, accessories' power, and other necessary data from the machines, only the driving resistance is questionable. In the case of an agriculture vehicle, the driving resistance directly depends on the terrain slope.

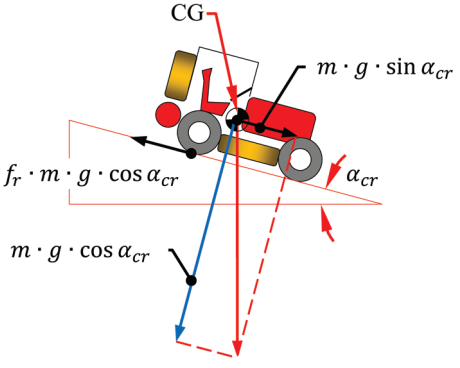


**Fig. 11.** *Force equilibrium at critical slope determination*

To fulfil the second condition with the lowest power of the IC engine, the rolling resistance should be equal to the gravity acting along the slope direction, Fig. 11. The calculation of the critical slope, $\alpha_{cr}$, is done as follows:

$$m \cdot g \cdot \sin \alpha_{cr} = f_r \cdot m \cdot g \cdot \cos \alpha_{cr}, \tag{18}$$

$$m = m_T + m_D + m_{mu} + m_{Sp}, \tag{19}$$

where $m$ is total mass of EH machine, $f_r = 0.25$ rolling resistance coefficient [14], and $\alpha_{cr}$ critical slope.

From the above equation, it is derived that:

$$\alpha_{cr} = \tan^{-1} f_r. \tag{20}$$

Considering the supposed rolling resistance in its value, the critical slope is: $\alpha_{cr} = 14°$.

Once the critical slope is determined, the terrain topography can be judged, Fig. 12. The only constraint to be considered is that each slope should be greater than a critical one.

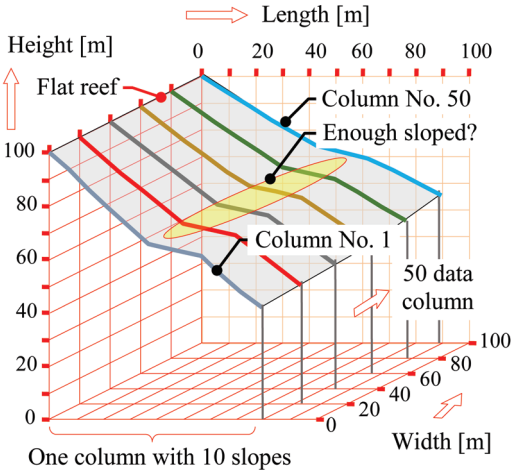


**Fig. 12.** *Presentation of one hectare of terrain with the topography, which is perhaps locally not sufficiently sloped*

Another representation of the terrain can be made with the matrix of partial slopes.

$$\mathbf{M}_{Slope} = \begin{bmatrix} 44 & 43 & & 33 & 32 \\ 44 & 43 & & 32 & 32 \\ 43 & 43 & \dots & 31 & 31 \\ 42 & 42 & & 30 & 30 \\ 42 & 41 & & 30 & 29 \\ 14 & 14 & & 14 & 14 \\ 14 & 14 & & 14 & 14 \\ 41 & 40 & \dots & 27 & 27 \\ 40 & 39 & & 27 & 27 \\ 38 & 38 & & 27 & 27 \end{bmatrix}. \tag{21}$$

The intention of the calculation of energy, the power and the time consumption on the terrain, as presented in Table 8, is to verify the IC engine power, which should not be too low.

**Table 8.** *Data for treating one hectare of realistic agricultural terrain (strip with limited slope in the middle of terrain)*

| | Two accessories 1 treatment | All accessories 24 treatments |
|---|---|---|
| Energy for treating [MJ] | 137 | 1719 |
| Fuel [l] | 11 | 142 |
| $CO_2$ emission [kg] | 30 | 377 |
| Labour time [h] | 2.5 | 35 |
| Efficiency [%] | 59 | 53 |

In case the slope of the particular segments on the terrain are too flat, the IC engine power will not be sufficient to run the accessories at full power while running the machine itself. In this case the IC

engine power should be increased to an extent that the engine is then able to run the accessories. In addition to the gravity force, which is acting along the slope, the driving force should be added, which is generated on the wheel circumferential. The sum of these forces should be in equilibrium with the rolling resistance:

$$m \cdot g \cdot \sin\alpha + \frac{\Delta P}{v_{av}} = f_r \cdot m \cdot g \cdot \cos\alpha. \qquad (21)$$

$\Delta P$ is IC engine power (excess over accessories needs), $\alpha$ actual minimum slope, and $v_{av}$ [m/s] average velocity of the machine.

From the Eq. (21) the IC engine power surplus can be derived:

$$\Delta P = m \cdot g \cdot v_{av} \cdot \left( f_r \cdot \cos\alpha - \sin\alpha \right). \qquad (22)$$

The power of the selected IC engine of the EH machine must be the same or greater than the power that is required to run the accessories and the machine downwards at the most flat terrain section where the minimal gravity force is acting.

## 5 CONCLUSIONS

In this article, the initial hypothesis about the possibility of the energy saving of the agricultural winch machine is confirmed. The problem of using the efficient potential energy in the working process cannot be carried out with the normal mechanical transmission, because each of the accessories needs their own input velocity and torque. As a result, the hydraulic transmission is the only rational way to effectively use the potential energy, which is available in abnormal quantities on this type of agriculture terrain. For the real terrain is proven the rise of the crop treatment efficiency per year from the normally 0.33 % to 0.52 % that is characteristic of the new EH machine. At the same time the labor time is shortened from 60 hours to 35 hours only.

The designer of the new EH machine defends the use of the IC engine with the minimal power due to minimal machine weight, minimal environmental burdens, and as low as possible expenses. A few purely theoretical calculations where the new EH machine and the potential competitors are compared on the ideal terrain to emphasize the eligibility of the proposed new machine. According to the analysis, the use of the common winch cart that is widely in use around the world seems to be non-economical and not rational.

## 6 REFERENCES


[1] Jerončič, R., Bernik, R. (2008). The Research of the number of accidents with the agriculture and forestry tractors in the Europe and the main reasons for those accidents. *Strojniški vestnik - Journal of Mechanical Engineering*, vol. 54, no. 7-8, p. 557-564.

[2] Bernik, R. (2004). *Techniques in Agriculture*. University of Ljubljana, Biotechnical Faculty, Ljubljana (in Slovene)

[3] Vidoni, R., Bietresato, M., Gasparetto, A., Mazetto, F. (2015). Evaluation and stability comparsion of different vehicle configurations for robotic agricultural operations on side slopes. *Biosystems Engineering*, vol. 129, p. 197-211, **DOI:10.1016/j.biosystemseng.2014.10.003**.

[4] Oswald, W. (2000). *Taschenbuch der Weinbautechnik.* Fachverlag Dr. Fraund, Mainz.

[5] Bohme, A. (2003). *Umweltgerechte Technik den Steillagenweinbau*. KTBL, Darmstadt.

[6] Uberti, S., Gadola, M., Chindamo, D., Romano, M., Galli, F. (2015). Design of a double wishbone front suspension for an orchard-vineyard tractor: Kinematic analysis. *Journal of Terramechanics*, vol 57, p. 23-39, **DOI:10.1016/j.jterra.2014.11.001**.

[7] Rühling, W. (1991). *Mechanisierung von Steillagen auf der Basis handgeführter Kleinraupen*. Der Deutsche Weinbau, no. 16, p. 631-638.

[8] Bartsch, M. (2013). New machine could save German vineyards, from *http://www.spiegel.de/international/germany/steeply-sloped-german-vineyards-hope-technology-can-save-them-a-935752.html*, accessed on 2016-11-10.

[9] Mashadi, B., Hanif, H. (2009). Automatic control of a modified tractor to work on steep side slopes. *Journal of Terramechanics*, vol. 46, no. 6, p. 299-311, **DOI:10.1016/j.jterra.2009.08.006**.

[10] Wild, K., Auernhammer, H. (1996). Ansätze zur automatisierten Arbeitszeitermittlung bei Feldarbeiten. *Landtechnik*, vol. 51, no. 4, , p. 198-199, DOI:10.15150/lt.1996.2771

[11] Jäger, P. (1991). Zeitbedarf von Feldarbeiten. *Landtechnik*, vol. 46, no. 4, p. 69-71.

[12] Hrastar, K. (2014). *Tractor Catalogue: Handbook*. ČZD Kmečki glas. Ljubljana (in Slovene).

[13] Zupan Catalog (2016). from *htpp://www.zupan.si*, accessed on 2016-11-10

[14] Saarilahti, M. (2002). *Soil Interaction Model*. MSc thesis, University of Helsinki, Helsinki.

[15] FITO-INFO Catalog (2016). from *http:///www.fito-info.si,* accessed on 2016-11-10.

[16] INO Brežice Catalog (2016). from *http://www.inobrezice.com,* accessed on 2016-11-10.

[17] Fabijan Catalog (2016). from *http://www.fabijan.si*, accessed on 2016-11-10.

[18] KGM-Podlehnik Catalog (2016). from *http://kmg-podlehnik.si*, accessed on 2016-11-10

[19] Katrašnik, T., Trenc, F., Oprešnik, S. (2007). Study of the energy-conversion efficiency of hybrid powertrains. *Strojniški vestnik - Journal of Mechanical Engineering*, vol. 53, no.10, p. 667-682.

[20] Hunt, D. (1995). *Farm Power and Machinery Management*. Iowa State University, Arnes, p. 259-275.
[21] Flašker, J., Pehan, S. (2005). *Power Transmissions*. University of Maribor, Faculty of Mechanical Engineering, Maribor. (in Slovene)
[22] Flašker, J., Pehan, S. (2008). *Tribology*. University of Maribor, Faculty of Mechanical Engineering, Maribor, Maribor. (in Slovene)
[23] Eggert, J. (2005). *Engineering Design*, Prentice Hall, New Jersey.
[24] Bižal, A., Klemenc, J., Fajdiga, M. (2014). Evaluating the statistical significance of a fatigue-life reduction due to macro-porosity. *Strojniški vestnik - Journal of Mechanical Engineering*, vol. 60, no. 6, p. 407-416, **DOI:10.5545/sv-jme.2013.1453**.
[25] Zaletelj, H., Fajdiga, G., Nagode, M. (2011). Numerical methods for TMF cycle modeling. *Strojniški vestnik - Journal of Mechanical Engineering*, vol. 57, no. 6, p. 485-494, **DOI:10.5545/sv-jme.2010.212**.
[26] Kodrič, M. (2016). *Development of a Hybrid Machine for Working on Sloping Terrain*, PhD Thesis, University of Maribor, Faculty of Mechanical Engineering, Maribor. (in Slovene)
[27] Kraut, B. (1987). *Mechanical Engineering Handbook*. Tehniška založba Slovenije, Ljubljana. (in Slovene)
[28] Ecoscore Catalog (2016). from *http://www.ecoscore.be*, accessed on 2016-11-10.
[29] Hykin, S. (1994). *Neural Networks, a Comprehensive Foundation*. MacMillan College New York.
[30] Bishop, C.M. (1995). *Neural Networks for Pattern Recognition*. Clarendon Press, Oxford.
[31] Rahimi-Ajdadi, F., Abbaspour-Gilandeh, Y. (2011). Artificial Neural Network and stepwise multiple range regression methods for prediction of tractor fuel consumption. *Measurement*, vol. 44, no. 10, p. 2104-2111, **DOI:10.1016/j.measurement.2011.08.006**.

Strojniški vestnik - Journal of Mechanical Engineering 63(2017)3, 181-190

DOI:10.5545/sv-jme.2016.3508 Original Scientific Paper
Received for review: 2016-03-01
Received revised form: 2016-08-06
Accepted for publication: 2016-10-05

# Modelling and Control of a Fixed Calliper-Based Electronic Wedge Brake

Fauzi Ahmad[1,2,*] – Khisbullah Hudha[3] – Saiful Amri Mazlan[1] – Hishamuddin Jamaluddin[4] – Hairi Zamzuri[1] – Zulkiffli Abd Kadir[1,3] – Vimal Rau Aparow[3]

[1] University of Technology of Malaysia, Malaysia-Japan International Institute, Malaysia
[2] Technical University of Malaysia, Faculty of Mechanical Engineering, Malaysia
[3] National Defence University of Malaysia, Faculty of Engineering, Malaysia
[4] Southern University College of Malaysia, Faculty of Engineering and Information Technology, Malaysia

*This paper presents a new design of an electronic fixed calliper-based wedge brake system. The movement of both sides of the brake piston is activated by a wedge block mechanism. The proposed fixed calliper-based electronic wedge brake system is a class of hydraulic-free device. The mechanism consists of two sets of wedge blocks, a ball screw drive shaft, a sliding beam and an electric motor. In this mechanism, the rotation of the shaft of the electric motor is converted into linear motion by using a ball screw drive shaft while the linear motion of the drive shaft will force the sliding beam to be displaced linearly. This will activate the wedge mechanism, which will cause the pad to be displaced tangentially to the disc brake. The movement of the pad in pressing the disc will generate clamping force and produce brake torque when the wheel rotates. In this study, the mathematical model of the system that generates the clamping force was identified. The model was based on a second order transfer function. The proposed mathematical model was then validated experimentally using a brake test rig installed with several sensors and input-output (IO) device. The performance of the brake mechanism in term of rotational input of the drive shaft and clamping force produced by the brake were observed. Accordingly, a torque tracking proportional–integral–derivative (PID) control of the system was proposed and studied through simulation and experiment. Comparisons between experimental results and model responses were made. It is found that the trend between simulation results and experimental data are similar, with an acceptable level of error.*

**Keywords: fixed calliper-based electronic wedge brake, clamping force system modelling and validation, torque tracking control, hardware-in-the-loop-simulation**

**Highlights**

- *This paper presents the modelling and validation of a fixed calliper-based electronic wedge brake.*
- *It also discusses on the effectiveness of the model in order to develop a good control strategy for the FIXEWB.*
- *Based on the developed control strategy, the effectiveness of the proposed torque tracking control of the FIXEWB was studied and presented.*
- *The control strategy developed is based on a PID controller.*

## 0 INTRODUCTION

The enforcement of stringent active safety standards has led to the need for an active braking system in vehicles. An active braking system requires a fast response actuator to react effectively during critical situations. However, meeting this requirement with conventional hydraulic braking (CHB) systems is almost impossible due to its limitations, such as delayed response time up to 300 ms, highly non-linear two-step control, bulky size; heavy weight, and leakage in the hydraulic line **[1]** to **[3]**.

Inspired by the introduction of "x by wire" technology, a new braking system has been proposed as the solution to overcome the drawbacks of the CHB: electromechanical brake (EMB). However, an EMB that uses a motor linked to a gearbox requires actuation power that corresponds to the required clamping force to halt the wheel **[4]** and **[5]**. This power requirement is not sufficient where existing vehicles use only a 12V power supply. Concurrent with the extensive investigation on EMB, researchers started to search for other techniques to take advantage of the EMB in achieving higher clamping force with standard 12V power supply **[6]**. Subsequently, an EMB-based wedge mechanism later known as electronic wedge brake (EWB) has been proposed as one of the most interesting mechanisms to be investigated.

EWB is a pure electronically controlled actuator. It typically comprises an electric motor driving a wedge mechanism to clamp and release the brake rotor **[6]**. As a result, it has the potential to further reduce the braking time, as well as the easier integration of advanced control features such as anti-lock braking system (ABS), vehicle stability control (VSC), electronic parking brake (EPB), etc. **[6]** and **[7]**.

The investigation into EWB was first started by the German Aerospace Centre (eStop®) that proposed a simple and efficient mechatronic wedge brake namely eBrake® **[6]**. With the subsequent

Corr. Author's Address: Malaysia Japan International Institute, University of Technology, 54100 Jalan Semarak Kuala Lumpur, Malaysia, fauzi.ahmad@utem.edu.my.

introduction of EWB, a number of EWB designs have been produced, e.g. [8] to [15], as well as studies on modelling, design, optimization and control issues of EWBs reported [16] to [20]. Despite the favourable introduction of EWB over the last decade, the brake types were similarly designed based on the floating calliper type.

The capability of EWB usage in vehicle braking system is still lacking. All the tests conducted on EWB system showed only slight improvement; they were done only through modelling and validation. In contrast, successful implementations of EWB usage in vehicle braking system were reported by [7] and [20]. However, the experimental results obtained were not as expected theoretically [20]. According to [20], the disparities between the simulation and the experimental data were caused by the simplification and idealization during modelling of the system.

Generally, in the modelling of a dynamic system, two techniques can be used; the physical parametric estimation method (PPEM) and the system identification method (SIM). PPEM refers to the models in which the characteristic of the systems can be represented as linear and non-linear elements with defined parameters. However, SIM is entirely based on the performance of specific systems commonly depicted from a series of experiment input and output data. In this condition, it is best to say that, the modelling technique used by [20] is based on PPEM, which probably causes the disparities. The technique has also been used by [7], [8], [12], [19] and [21] resulting in more than 10 percent disparity between simulation and experimental results [12]. This is due to the PPEM technique needing several assumptions that might degrade the adequacy of the model. In order to overcome this problem, the SIM technique is a good and may be a better way to be used. This is because of the ability of the technique that can produce an adequate mock-up of the proposed system with less than 5 % error [16].

The global demand in the automotive vehicle sector today is for a vehicle that can provide a high dynamic response; therefore, a high capacity braking system is needed. A fixed calliper-based electronic wedge brake (FIXEWB) is thus proposed in this study. Basically, the proposed design of FIXEWB is a replacement to the fixed calliper-based CHB. Meanwhile, the SIM technique was then proposed to develop a mathematical equation of the FIXEWB. Based on the model, a torque tracking control of the system was then developed by using PID controller and validated experimentally using a hardware-in-the-loop-simulation technique.

## 1 THE FIXEWB

As the effective braking force generated is dependent on the angle of the wedge, the determination of the optimum wedge angle needed is essential. Since the optimum wedge angle is interdependent with the friction coefficient of the brake pad, the selection of brake pad should be made first. These two factors are very important in the initial decision process in order to produce a higher braking force and also to avoid the probability of the wedge sticking. Therefore, in this study, the brake pad used in a Malaysian national car was selected for the design consideration of the EWB and particularly the wedge angle. By referring to the SAE standard on brake pad [22] to [25], the E code shown on the pad indicates that the coefficient of friction of the pad lies between 0.25 to 0.35, as listed in Table A1 in the Appendix.

To select an appropriate wedge angle, the work done by [10] is referenced. Fig. 1 shows the free body diagram of one side of the FIXEWB mechanism. Note that $\alpha_w$ is the angle of the wedges, $F_r$ is the wedge friction force that occurs between the inner and outer wedges, $F_m$ is the motor force to the wedge and $\mu$ is the pad coefficient of friction. Assuming that the motor force is divided equally to both sides of the wedges and the forces acting on the left wedge is the same as on the right wedge, the relationship between the wedge pushing forces, friction forces, clamping forces, and braking forces to the disc for both sides of the wedges is given by:

Summation of force in $y$ direction:

$$\sum F_y = 0, , \tag{1}$$

$$F_m + F_r \sin\alpha_w + F_b = 0, \tag{2}$$

therefore,

$$F_r \sin\alpha_w = -(F_b + F_m). \tag{3}$$

Summation of force in $x$ direction

$$\sum F_x = 0, \tag{4}$$

$$-F_r \cos\alpha_w - F_n = 0, \tag{5}$$

therefore,

$$F_r \cos\alpha_w = -F_n. \tag{6}$$

By dividing Eq. (3) with Eq. (6), the summation of force at the wedge can be defined as follows:

$$\tan\alpha_w = \frac{F_{b+F_m}}{F_n}. \tag{7}$$

Noted that $F_n = F_c$ therefore $F_b = \mu F_c$. Rearrange Eq. (7) to be:

$$F_c \tan\alpha_w = F_m + \mu F_c. \tag{8}$$

Hence

$$F_c = \frac{F_m}{\tan\alpha_w - \mu}. \tag{9}$$

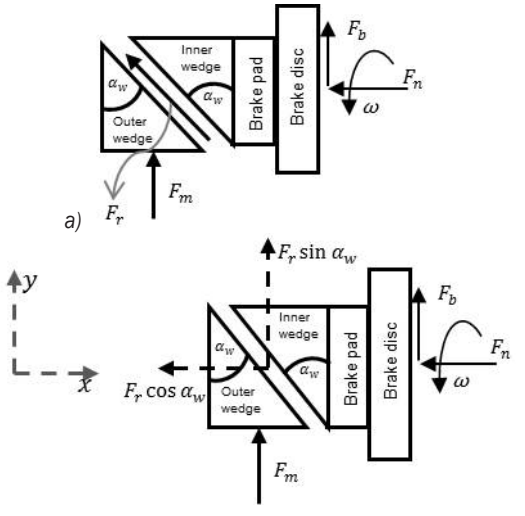


**Fig. 1.** *Free body diagram of FIXEWB; a) one side of FIXEWB, b) friction force distribution*

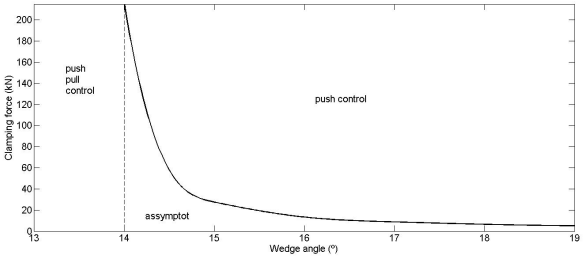


**Fig. 2.** *Clamping forces vs. wedge angle*

As shown in Fig. 2, the relationship between clamping force and the wedge angle can be described by employing Eq. (3) by assuming $F_m$ is 500 N and $\mu$ is 0.25 (according to the selected brake pad). It can be seen that the critical angle of the wedge is about 14.03° which is equal to $\tan\alpha_w = \mu$. In this condition, the clamping force is self-generated resulting from the friction between the wedges to the disc brakes. However, if the wedge angle is less than the critical angle, it will cause the actuator to work harder to push the wedge. When the pad and disc are in contact, the braking force created is greater than the force initiated from the actuator and causes greater pulling force that is needed to release the wedge. Therefore, in this study, the optimum wedge angle was chosen to be 15° to ensure the larger clamping forces can be produced, which are easy to control and to prevent the wedge from being jammed.

The effectiveness of the selected wedge angle can be examined by introducing the required motor force by varying the coefficient of friction. Fig. 3 was obtained by assuming the clamping force of 46 kN and varying the coefficient of friction from 0.25 to 0.35. From the figure, it can be seen that 1 kN motor force is required to create the desired clamping force at the initial condition. While at the coefficient of friction of 0.267, self-reinforcement will exist; thus, no motor force is needed. Other than that, as the coefficient of friction increases, the motor force becomes negative. The shifting from the positive to the negative force indicates that when the mechanism is working to sustain the required clamping force by varying the friction coefficient, the wedge needs to be repositioned hence retraction control is needed. Based on the optimised wedge angle, the CAD design of the FIXEWB is shown in Fig.4.

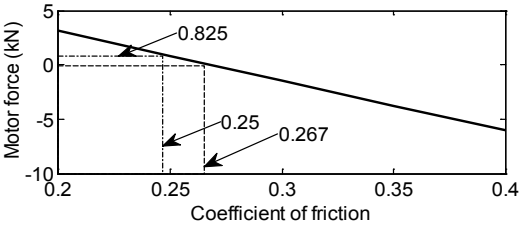


**Fig. 3.** *Motor force vs. coefficient of friction*

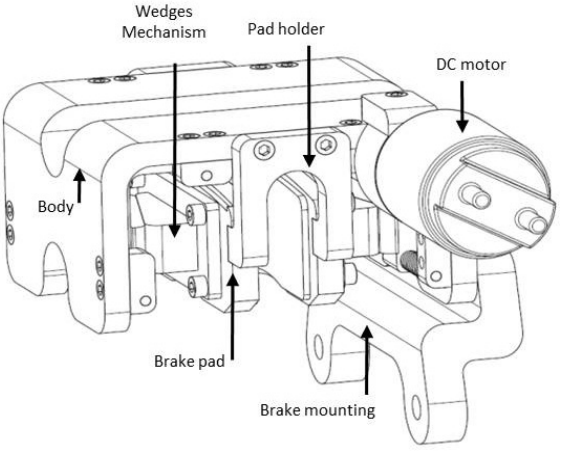


**Fig. 4.** *FIXEWB concept design*

### 1.1 Hardware of FIXEWB

The hardware of FIXEWB is shown in Fig. 5. The FIXEWB is driven by a DC motor that is directly

connected with a slider beam through a drive shaft. The slider beam, which enables forward and back movements, will initiate the inner wedges to move tangentially to the slider beam movement hence clamping the brake disc. The on-off condition of the brake is shown in Fig. 6.

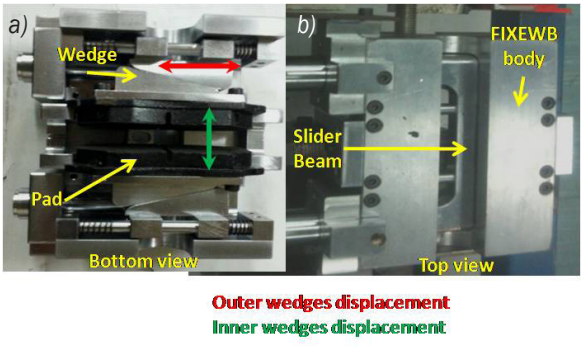


**Fig. 5.** *FIXEWB hardware, a) bottom view and b) top view*

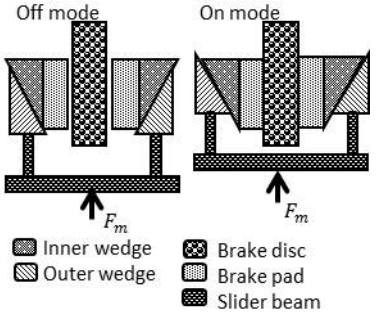


**Fig. 6.** *On-off mode FIXEWB*

### 1.2 FIXEWB Test Rig and Experimental Setup

As shown in Fig.7, the FIXEWB test rig consists of a FIXEWB actuator equipped with a data acquisition system, a force sensor and a potentiometer. The potentiometer was attached to the drive shaft to measure the rotational input to the calliper. The force sensor attached to the brake pad is used to measure the clamping force produced by the brake system. A National Instrument NI PCI 6221 card along with SCB-68 Quick reference label M-Series device were used as the data logger, and an electronic control unit (ECU) was used as the embedded system to control the FIXEWB. The ECU consists of three main circuits: a microcontroller unit (MCU ATMEGA 32, an opto-coupler, and H-Bridge driver circuits as the current buffer to drive the system. The hardware of the ECU is shown in Fig. A1 in the Appendix.

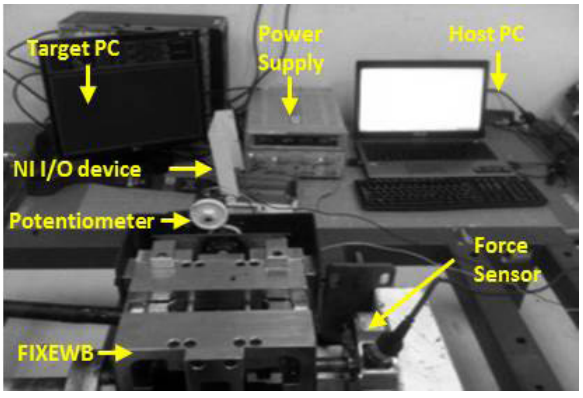


**Fig. 7.** *FIXEWB test bench*

Before experimental work was performed, the initial gap between the brake pad and the force sensor was set to approximately 0.5 mm by using a filler gauge. From this experiment, the responses measured were angle displacement and clamping force of the system as shown in Fig. 8.

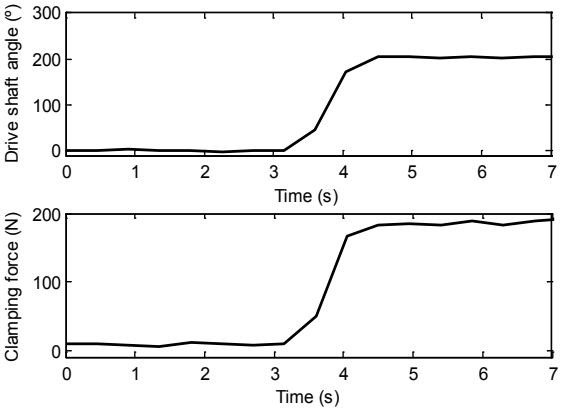


**Fig. 8.** *Training data obtained*

## 2 CLAMPING FORCE MODELS AND BRAKE TORQUE CALCULATION OF FIXEWB

Based on the training data obtained from the experiment shown in Fig. 8, a transfer function (TF) was developed to represent the relationship between the input and output of the system. In this system, the TF is expressed as the ratio of the Laplace transform of the clamping force and the drive shaft angle and corresponds to the Laplace transform of the impulse response $G(s)$. The transfer function of the system identified using the system identification method is:

$$G(s) = \frac{1.508}{s^2 + 0.571s + 0.7492}. \quad (10)$$

By referring to Fig. 9, the braking torque at the contact interface can be predicted as:

$$T_b = R_{eff} F_c, \tag{11}$$

where, $T_b$ is the brake torque, $R_{eff}$ is the effective pad radius and $F_c$ is the clamping force. However, the friction force generated at the contact interface, $F_b$ is dependent on normal force ($F_n$) and friction coefficient ($\mu$), given by:

$$F_b = \mu F_n. \tag{12}$$

The magnitude of the normal force is the same as the clamping force ($F_c$) applied to the top of the pad, as shown in Fig. 9. Since there is a pair of brake pads in the brake system, the total brake torque is:

$$T_b = 2\mu F_c. \tag{13}$$

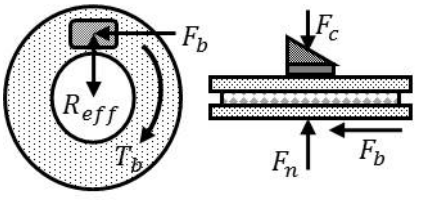


**Fig. 9.** *Brake torque model in contact interface side and top view*

### 2.1 DC Motor Model

In this FIXEWB system, a permanent magnet direct current motor (DC motor) was used to drive the FIXEWB. A DC motor is used because of several advantages, such as higher reliability since there are no brushes that may be susceptible to mechanical failure, reduced heat dissipation from the rotor, higher torque-to-inertia ratio, and a significant reduction in friction. The mathematical equations of the DC motor can be found in [9].

### 2.2 Validation of FIXEWB Model

The validation results of the proposed mathematical model for the FIXEWB are shown in Figs. 10 to 12. Several validation tests have been employed by varying the magnitude of the drive shaft angle i.e. step input, multiple step input and sine wave. The parameters of the model are defined as follows: $\mu$=0.25 and $R_{eff}$=150 mm. As shown in Fig. 10, the step input function has been used as the input rotation to the calliper, the output of the system is the clamping force resulting from the displacement of the wedges and the brake pad. It is noted that for 200° rotational input to the drive shaft, an approximately about 400 N clamping force and a 30 Nm braking torque are generated.

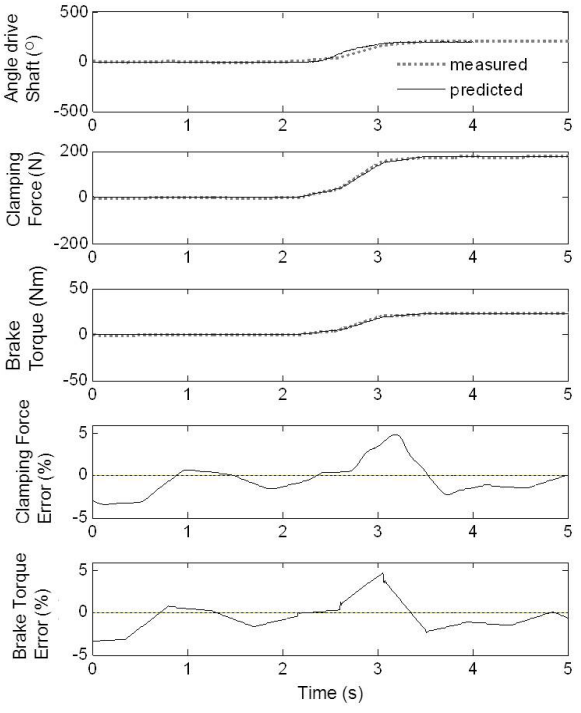


**Fig. 10.** *Validation using step input*

To validate the model further, another observation has also been made by using multiple steps input and sine input. The multiple steps and sine input tests were used to assess the effectiveness of the developed equation in order to present a continuous input to the system. As shown in Figs. 11 and 12, it can be seen that the trends between simulation results and experimental data are almost similar with acceptable errors in terms of the drive shaft displacement, clamping forces, and the brake torque produced. It was noted that the deviations between the simulation and the experimental data are almost less than 5 %. Some deviation in the experimental results is possibly caused by backlash at the connection between the DC motor and the drive shaft and the frictions between the mechanical moving parts that produced delay behaviour.

Overall, it is noted that the trends between simulation results and the experimental data are in good agreement with acceptable error. Conversely the error can be significantly reduced by fine tuning the modelling parameters. However, excessive fine tuning can be avoided since in the control-oriented model, the most important characteristic is the trends of the model response. As long as the trend of the model

is closely similar with the measured response with acceptable deviation in magnitude, it can be said that the model is adequate.

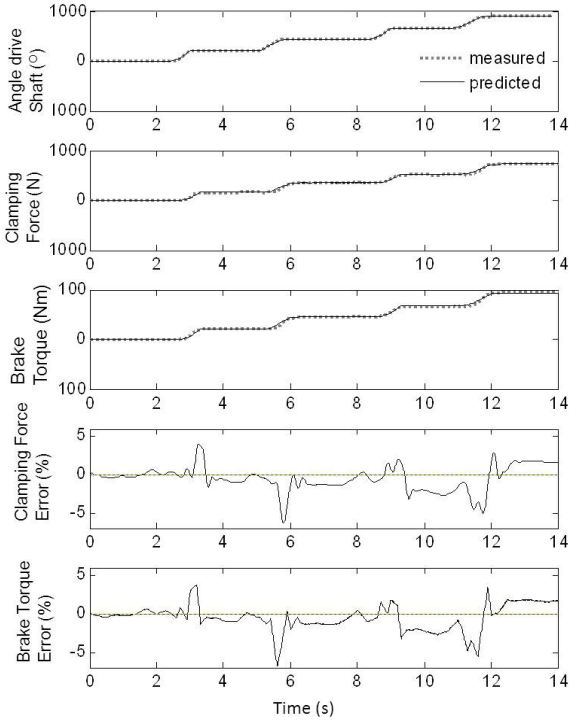


**Fig. 11.** *Validation using multiple steps input*

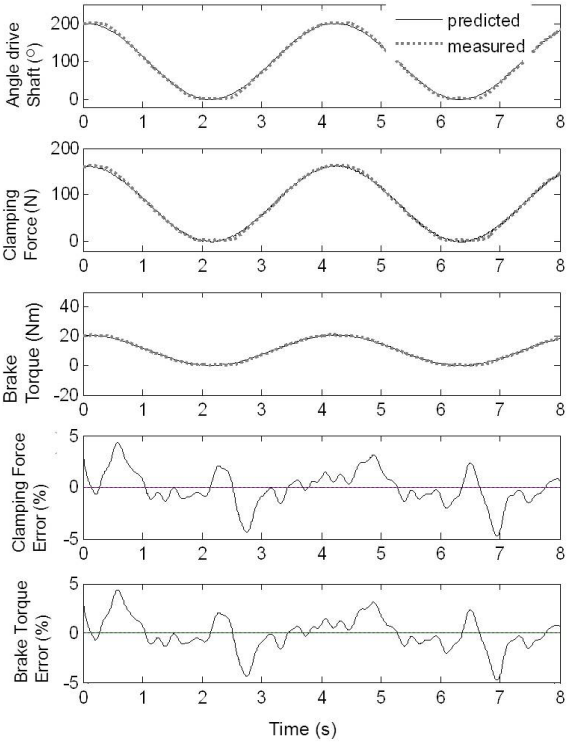


**Fig. 12.** *Validation using sine input*

## 3 FIXEWB CONTROLLER

The basic control structure of the proposed FIXEWB control is shown in Fig. 13. In this control structure, three control loops are employed, which are torque, speed and position control loops. For the torque controller, a proportional integral derivative (PID) based feedback controller was used. As the braking ability is influenced by a driving style that sometimes needs fast and slow braking responses, the brake actuator needs to work in a wide range of speed. Therefore, another feedback-based P controller, which acts as a speed controller, was used for maintaining the braking torque by allowing the motor to rotate at high speed regardless of the braking torque demand. The other loop is the position control-based PID controller used to maintain the gap distance between the pad and the disc brake. The controller parameters were tuned using Ziegler-Nichols method and the tuned controller parameters are shown in Table 1. The performance observed is brake torque tracking performance. Several test signals were used as the torque demand, which are the step, sine wave, square wave and saw tooth functions with magnitudes of 400 Nm, 800 Nm and 1200 Nm.

**Table 1.** *Controller parameters*

| Controller | P | I | D |
|---|---|---|---|
| Brake torque | 0.5411 | 3.809 | 0.02623 |
| Position | 30 | 2 | 1 |
| Speed | 0.01 | - | - |

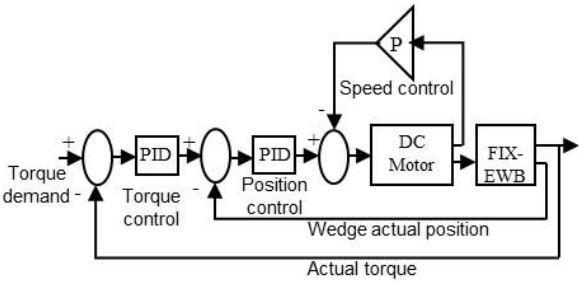


**Fig. 13.** *FIXEWB controller structure*

### 3.1 Performance Evaluation of Torque Tracking Controller of FIXEWB

Fig. 14 shows the performance evaluation of the torque tracking controller using a step input function. It can be seen that there is good agreement between the simulation results with the experimental data. For 400 Nm, 800 Nm, and 1200 Nm peak torque, Fig. 14

shows the ability of the controller structure in tracking the desired trajectory is very promising. However, there are some deviations between the responses for 1200 Nm (Fig. 14c), where the experimental response is slightly slower in comparison to the simulation with the difference about 1.25 s. Meanwhile, the percentage overshoot for 400 Nm, 800 Nm, and 1200 Nm peak torque in simulation are 5 % while in the experimental responses, the percentage overshoot for both 400 Nm, 800 Nm, and 1200 Nm are 1.38 %, 7.5 %, and 6.3 %, respectively. For the torque of 800 Nm, the settling time of the simulation and the experimental results are 4.8 s and 5.3 s, respectively, while for 1200 Nm the simulation and experimental results are 4.8 s and 6.06 s, respectively.

The torque tracking for sinusoid function with various peak torques shows good tracking performances between simulation and experimental results. This can be seen in Fig. 15, where there is good agreement between the simulation results and the experimental data, even though nonlinearities exist in the experimental responses.

The performance evaluations of tracking torque for sawtooth function with various peak torques are shown in Fig. 16. It can be seen that for this input function the torque tracking system is quite good, although it is unable to closely follow the desired torque, especially at the peak. However, it can be seen from the figure that the performance is poor when the actuator provides negative torque; meanwhile, when providing positive torque, the performance of torque tracking control is excellent. Aside from that, it is observed that there are jerk phenomena in between the maximum and minimum peak torque. This jerking is due to the extra effort needed by the actuator to follow the desired trajectories while at the same time the motor speed is limited.

For the square input function shown in Fig. 17, the system shows the tendency to follow the desired torque with similar trends for both simulations and experiments. However, the effort by the controller to produce a fast time response has led the system to produce high percentage overshoots and slower settling times. The percentage overshoot for simulation with 400 Nm, 800 Nm and 1200 Nm are 12.37 %, 22.5 % and 23.34 % respectively, while for experiments are 12.33 %, 23.1 %, and 23.37 %, respectively. The average settling time for simulations is about 4.58 s while for experiment results it is around 4.63 s. Otherwise, the average rise times at 100 % target value between the desired torques with simulation and experimental data are about 0.36 s and 0.57 s, respectively.

The deviations between simulation and the experimental data may be due to the load disturbance from the moving part in the hardware that lowers the speed of the system. For the simulation, the masses of the moving parts in a mechanical system, such as a pad and slider beam, were ignored but not in the actual model. Furthermore, the finishing of the hardware and the limitation of DC motor may also contribute to the slow response of the system. However, the study

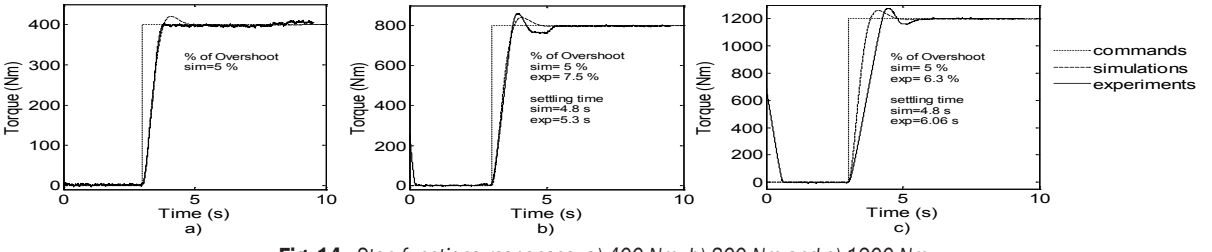


**Fig. 14.** *Step functions responses, a) 400 Nm, b) 800 Nm and c) 1200 Nm*

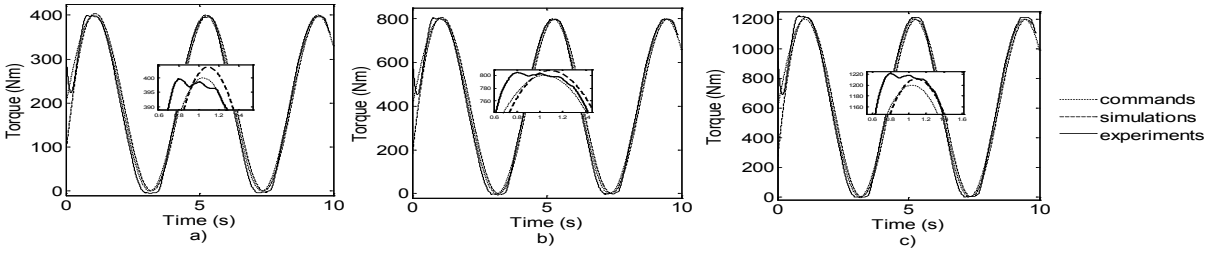


**Fig. 15.** *Sine functions responses, a) 400 Nm, b) 800 Nm and c) 1200 Nm*

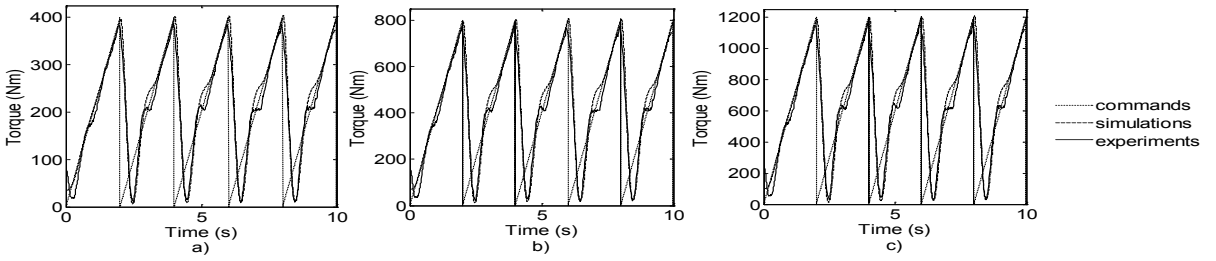


**Fig. 16.** *Saw tooth functions responses, a) 400 Nm, b) 800 Nm and c) 1200 Nm*

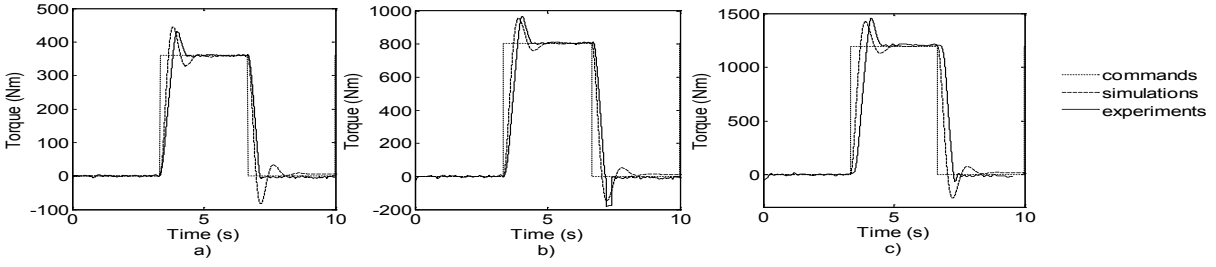


**Fig. 17.** *Square functions responses, a) 400 Nm, b) 800 Nm and c) 1200 Nm*

has shown the proposed transfer function is adequate to be used as a model of FIXEWB for simulation. The combination of mathematical modelling with an appropriate control strategy produced overall good responses of the system with good performance and acceptable stability. It is shown for torque tracking of step, sine wave, and square input functions; the ability of the simulation system to track the desired trajectory is promising and agreeable with the experimental result even though there is a slight deviation for saw tooth input function. It also indicates that the proposed system together with the control strategy performs well in a real system and shows the capability of the system applied to a real system.

## 4 CONCLUSION

In this study, a fixed calliper-based electronic wedge brake has been designed and fabricated. The FIXEWB system consisted of two sets of wedge mechanism, drive shaft, slider beam and an electric motor as the actuator. The transfer function model of the brake mechanism was identified to represent the dynamic behaviour of the proposed FIXEWB. Then, by combining the FIXEWB model with the brake torque model in contact interface, the brake torque produced by the FIXEWB system can also be estimated. The predicted responses of both clamping force output from the FIXEWB model and brake torque were compared with the measured responses of both clamping force and brake torque obtained using the FIXEWB test rig. The results showed that the responses of the model were in good agreement with the response of a real FIXEWB system. By using the validated FIXEWB model, a brake torque control-based PID controller was developed. The controller strategy consisted of three control loops (actuator position control loop, actuator speed control loop, and brake torque control loop) was designed. To verify the effectiveness of the controller strategy, a torque tracking control of the FIXEWB was performed in both simulation and experimental studies. Several tests were conducted such as brake torque demand of 400 Nm, 800 Nm and 1200 Nm for step, sine, sawtooth and square input functions, respectively. The results demonstrated that the proposed FIXEWB model along with a suitable control structure is able to produce good performance and closely follow the desired torque for step, sine, sawtooth, and square functions. The simulation behaviour was found to be agreeable with the experiment's data. This is due to the ability of the developed mathematical model to describe the behaviour of the FIXEWB adequately and the effectiveness of the controller strategy. Therefore, it is demonstrated that the torque control scheme is suitable to be applied in the inner loop part of the vehicle brake system as well as in the active braking particularly in ABS systems.

## 5 ACKNOWLEDGEMENTS

This work is part of a research project entitled "Robust stabilization of armoured vehicle firing dynamic using active front wheel steering system", funded by LRGS grant (No. LRGS/B-U/2013/UPNM/DEFENSE & SECURITY – P1).

## 6 REFERENCES

[1] Kim, J., Jo, C., Kwon, Y., Cheon, J.S., Park, S.J., Jeon, G.B., Shim, J. (2014). Electro-mechanical brake for front wheel with back-up braking. *SAE International Journal of Passenger Cars – Mechanical System*, vol. 7, no. 4, p. 1369-1373, **DOI:10.4271/2014-01-2538**.

[2] Haggag, S., Abidou, D. (2013). An approach to vehicle brake-by-wire optimal control tracking strategy. *SAE International Journal of Passenger Cars – Mechanical System*, vol. 6, no. 1, p. 154-162, **DOI:10.4271/2013-01-0686**.

[3] Karakoc, K. (2005). *Design of a Magnethorheological Brake System Based on Magnetic Circuit Optimization*. MSc Thesis. University of Victoria, Victoria, available at: *https://dspace. library. uvic. ca//handle/1828/197*, accessed on: 2016-22-01.

[4] Schwarz, R., Isermann, R., Böhm, J., Nell, J., Rieth, P. (1998). Modelling and control of an electromechanical disk brake. *SAE Technical Paper*, paper no: 980600, **DOI:10.4271/980600**.

[5] Day, A. (2014). Electronic braking systems. Braking of Road Vehicles. Chapt. 11, p. 385-428, Elsevier, London, **DOI:10.1016/B978-0-12-397314-6.00011-5**.

[6] Hartmann, H., Schautt, M., Pascucci, A. Gombert, B. (2002). eBrake® - The mechatronic wedge brake. *SAE Technical Paper*, paper no. 2002-01-2582, **DOI:10.4271/2002-01-2582**.

[7] Roberts, R., Schautt, M., Hartmann, H., Gombert, B. (2003). Modelling and validation of the mechatronic wedge brake. *SAE Technical Paper*, paper no. 2003-01-333, **DOI:10.4271/2003-01-3331**.

[8] Ho, L., Roberts, R., Hartmann, H., Gombert, B. (2006).The electronic wedge brake-EWB. *SAE Technical Paper*, paper no. 2006-01-3196, **DOI:10.4271/2006-01-3196**.

[9] Semsey, Á., Roberts, R. (2006). Simulation in the development of the electronic wedge brake. *SAE Technical Paper*, paper no. 2006-01-3196, **DOI:10.4271/2006-01-0298**.

[10] Emam, M.A.A., Emam, A.S., El-Demerdash, S.M., Shaban S.M., Mahmoud, M.A. (2012). Performance of automotive self-reinforcement brake system. *Journal of Mechanical Engineering*, vol. 1, no. 1, p. 4-10.

[11] Shin, D. H., An, J. N. (2012). Study of stiffness design of calliper for reducing the weight of an electronic wedge brake. *Applied Mechanics and Materials*, vol. 138-139, p. 159-162, **DOI:10.4028/ www.scientific.net/AMM.138-139.159**.

[12] Han, K., Kim, M., Huh, K. (2012). modelling and control of an electronic wedge brake. *Proceeding of the Institution of Mechanical Engineers, Part C: Journal of Mechanical Engineering Science*, vol. 226, no. 10, p. 2440-2455, **DOI:10.1177/ 0954406211435584**.

[13] Abd. Rahman, M. L. H., Hudha, K., Ahmad, F., Jamaluddin, H. (2013). Design and clamping force modelling of electronic wedge brake system for automotive application. *International Journal of Vehicle Modelling and Testing*, vol.8, no. 2, p. 145-156, **DOI:10.1504/IJVSMT.2013.054478**.

[14] Kim, J., Kim, M., Kim, J., Noh, K. (2009). Developing of electronic wedge brake with cross wedge. SAE Technical Paper, paper no. 2009-01-0856, **DOI:10.4271/2009-01-0856**.

[15] Kim, J. (2011). *Single Motor Electro Wedge Brake System Using Solenoid Mechanism for Implementing Additional Functions*. United States Patent & Trademark office, Washington, D.C., US 20080314695.

[16] Aparow, V. R., Hudha, K., Ahmad, F., Jamaluddin, H. (2015). Modeling and validation of electronic wedge brake mechanism for vehicle safety system. *Jurnal Teknologi (Science & Engineering)*, vol. 75, no. 1, p. 183-191, **DOI:10.11113/ jt.v75.2778**.

[17] Fox, J., Roberts, R. Baier-Welt, C., Ho, L. M., Lacraru, L. Gombert, B. (2007). Modelling and control of a single motor electronic wedge brake. *SAE Technical Paper*, paper no. 2007-01-0866, **DOI:10.4271/2007-01-0866**.

[18] Han, K., Huh, K., Hwang, W., Kim, M., Kim, D. (2012). EWB control based on the estimated clamping force. *SAE Technical Paper,* paper no. 2012-01-1797, **DOI:10.4271/2012-01-1797**.

[19] Roberts, R., Gombert, B., Hartmann, H., Lange, D., Schautt, M. (2004). Testing the mechatronic wedge brake. *SAE Technical Paper*, paper no. 2004-01-2766, **DOI:10.4271/2004-01-2766**.

[20] Cheon, J. (2010). Brake by wire system configuration and functions using front EWB (electric wedge brake) and rear EMB (electro-mechanical brake) actuators. *SAE Technical Paper*, paper no. 2010-01-1708, **DOI:10.4271/2010-01-1708**.

[21] Ghajari A., Kazemi, R. (2012). A New approach to the electronic wedge brake. *SAE Technical Paper*, paper no. 2012-01-1801, **DOI:10.4271/2012-01-1801**.

[22] SAE Standard J866 (2012). *Friction Coefficient Identification and Environmental Marking System for Brake Lining*. SAE International Vehicle Recommended Practice.

[23] Sayim, I., Zhang, D. (2016). Optimization of the Brake Factor for an S-Cam Foundation Brake using RSM. *Strojniški vestnik - Journal of Mechanical Engineering*, vol. 62, no. 9, p. 503-510, **DOI:10.5545/sv-jme.2016.3459.**

[24] Karabay, S., Baynal, K., Igdeli, C. (2013). Detecting Groan Sources in Drum Brakes of Commercial Vehicles by TVA-FMEA: A Case Study. *Strojniški vestnik - Journal of Mechanical Engineering*, vol. 59, no. 6, p. 375-386, **DOI:10.5545/sv-jme.2012.809**.

[25] Grkić, A., Mikluc, D., Muždeka, S., Arsenić, Ž., Duboka, Č. (2015). A model for the estimation of brake interface temperature. *Strojniški vestnik - Journal of Mechanical Engineering*, vol. 61, no. 6, p. 392-398, **DOI:10.5545/sv-jme.2014. 2364**.

## 7 APPENDIX

**Table A1.** *Friction coeffcient code SAE Standard,* **[22]**

| Code letter | Coefficient of friction |
|---|---|
| C | Not over 0.15 |
| D | Over 0.15 but not over 0.25 |
| E | Over 0.25 but not over 0.35 |
| F | Over 0.35 but not over 0.45 |
| G | Over 0.45 but not over 0.55 |
| H | Over 0.55 |
| Z | Unclassified |

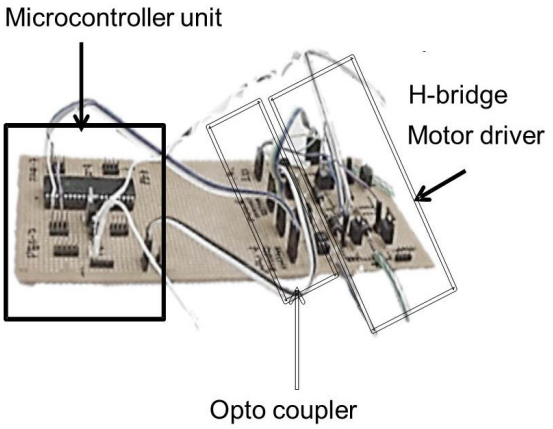


**Fig. A1.** *Electronic control unit*

Strojniški vestnik - Journal of Mechanical Engineering 63(2017)3, 191-200

DOI:10.5545/sv-jme.2016.4095 Original Scientific Paper
Received for review: 2016-10-04
Received revised form: 2016-12-14
Accepted for publication: 2017-01-17

# Vehicle Aerodynamic Stability Analysis under High Crosswinds

Aleksander Grm* – Milan Batista
University of Ljubljana, Faculty of Maritime Studies and Transport, Slovenia

*In a strong crosswind, wind direction change may result in vehicle stability loss. This paper presents a numerical study of vehicle aerodynamic stability in a high crosswind situation. We start with a model explanation and introduce the complete computational fluid dynamics (CFD) framework used in the study. Important CFD parameters such as mesh type, turbulence model, and boundary conditions are exposed and discussed in detail. We demonstrate and discuss the flow structure around a simplified truck model. Results of the CFD analysis are compared to experimental data, showing an almost perfect match. The final CFD outcomes are functions of aerodynamic coefficients that depend on the apparent wind angle. Then, CFD results are used in the application of an aerodynamic stability analysis for the truck model. Finally, the critical stability bounds are calculated, showing the marginal crosswind driving properties of the vehicles.*

**Keywords: aerodynamic stability/ instability, computational wind engineering, overturning moments, computational fluid dynamics, wind-structure interaction**

**Highlights**

- *A CFD vehicle aerodynamic stability analysis is presented in detail.*
- *Aspects of the effect of mesh type on the aerodynamics coefficients in CFD calculations are presented.*
- *A few highlights of the fit procedure for aerodynamic coefficients are emphasized.*
- *Rotation, rollover, and side-slip stability regions are shown in retrospect.*

## 0 INTRODUCTION

The flow around a heavy vehicle exhibits complex characteristics, such as a turbulent boundary layer, separation and reattachment on the vehicle surface, massive separation at the rear part of the vehicle, shear layer evolution, and large wakes. Furthermore, the Reynolds number (*Re*) is sufficiently high that turbulent flow develops almost everywhere, except during the early stages of its collision with the vehicle. Understanding the effects of these flow characteristics on vehicles aerodynamic properties has considerable practical importance. Numerous studies have been conducted both in academia and industry to understand and control the flow around the heavy vehicles [1].

The study of three-dimensional flow around a ground vehicle has become a subject of significant importance in many areas. For example, in the study of vehicle aerodynamic stability in a crosswind situation [2] and [3] when the aerodynamic coefficients depend on the apparent wind direction. One significant problem is the accuracy of the aerodynamic coefficients. The flow around ground vehicles, including the vehicle covered in this work, shares unsteady and three-dimensional features with that around other aerial or marine transportation vehicles. However, in contrast to the flow around a commercial airplane, ship, or submarine, a key phenomenon in the flow around a ground vehicle is massive flow separation, which significantly affects the aerodynamic forces and moments experienced by the vehicle. This phenomenon is more pronounced for heavy vehicles that have a boxy shape with many sharp edges, designed for carrying as much cargo and as many passengers as possible within regulated external dimensions.

Analysis of such complex flow can be performed through the experiments or numerical investigation. Currently, experiments with various vehicles are not always feasible due to the high costs of wind tunnel experiments, especially for a 1:1 model. The alternatives are computational fluid dynamics (CFD) tools. In the past, full 3D vehicle CFD analysis was significantly limited by the lack of computational resources and the high precision of CFD turbulent algorithms. Currently, however, this is no longer the case, and we can compute numerical calculations for almost any vehicle in reasonable time with affordable hardware. In this article, we used an ANSYS-CFX system to calculate the aerodynamic coefficients.

The article describes our model, including details on the geometry setup, computational domain, mesh generation, CFX setup, boundary conditions, and stop criteria. We have paid significant attention to the analysis of aerodynamic coefficients with respect to the mesh type. We focused on the difference in the boundary layer mesh algorithms. As described herein, the classical boundary layer meshing algorithm (first layer thickens (FLT)) approach did

*Corr. Author's Address: University of Ljubljana, Faculty of Maritime Studies and Transport, Pot pomorščakov 4, 6320 Portorož, Slovenia, aleksander.grm@fpp.uni-lj.si

not work as expected. Instead, an alternative meshing algorithm (first aspect ratio (FAR)) showed very good convergence results. After the model section, this article describes the definition of aerodynamic coefficients. The main idea behind is to obtain useful fitting models [4] to [7] that optimally represent the aerodynamic coefficients with respect to apparent wind direction and yaw angle $\psi$. A complex fit model does not always have better fitting properties. The ability to mimic a physical background in the fit model results in good fit model properties for real life data. As described in the results subsection, a linear combination of basic functions, fit model Eq. (3), shows most of the physical interpretation of the nature of aerodynamic coefficients with respect to the yaw angle $\psi$.

In the last section, the application of the fit model to vehicle aerodynamic stability is presented. Estimates are calculated for critical rollover, rotation, and side-slip parameters.

## 1 METHODS

The analysis of turbulent flow around a vehicle requires great care when building the CFD model. In order to obtain the necessary aerodynamic coefficients, a numerical model capable of producing a solution independent of time-step size, convergence limits, and other pertinent modeling conditions must be developed. In this study, a full three-dimensional CFD simulation model is used, because the vehicle is rotated around the center of gravity (CG), as shown in Fig. 1. The three-dimensional CFD model is developed using the ANSYS 16.0 workbench. CFX is used to solve the steady Reynolds-averaged Navier-Stokes equations, using the finite volume method with a two-equation turbulence model of the shear stress transport (SST) model [9], as is typically recommended for use in the calculation of aerodynamic coefficients [3]. We will not describe the details of the physical model of turbulent fluid flow, as it is completely described in the literature [10] to [12].

The modeled geometry is a truck model, described in [8] and shown in Fig. 1. The CAD model is identical to the model used in the wind tunnel experiments referenced in [5] and [8]. In this way, simulation data can be validated with experimental data. The top parts of Fig. 1 and Fig. 3 show the placement of the coordinate system and angle of rotation. The axis of rotation is parallel to the $z$ axis and passes through CG (Fig. 3). In external aerodynamics, proper mesh construction that embeds specific flow conditions plays a significant role. In real life, the flow conditions are turbulent and the Reynolds number ($Re$) [12] is very high ($Re \geq 10^6$).

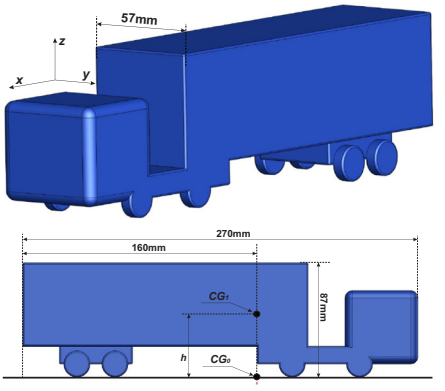


**Fig. 1.** *Truck geometry constructed in SolidWorks [8]; cabin edge fillet is 5 mm, rest edge fillet is 1 mm*

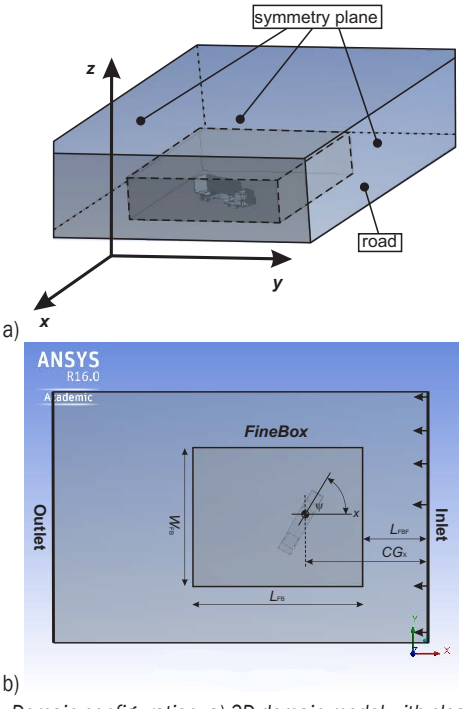


**Fig. 2.** *Domain configuration; a) 3D domain model with clear view of FineBox subdomain surrounding truck; b) z projection of the domain*

Turbulent flow develops almost everywhere, except in the zone where the flow first collides with the vehicle. To properly capture turbulent flow, the mesh must be constructed such that the mesh size detects the turbulent flow properties predicted by the turbulent SST model [9]. The mesh size will also define the computational time, and therefore, the mesh must be reasonably sized. External aerodynamics

must cope simultaneously with two flow regions. The first mesh-related characteristic flow region is the boundary layer region [13]. In the boundary layer region, the mesh must be constructed to account for turbulent model properties (wall functions [12]), according to the turbulent SST model. In the second region, which is referred to as the FineBox region and is positioned near the vehicle, the mesh must be fine enough to detect vortices that develop in the vicinity of the vehicle. The FineBox region forms a subdomain of the computational domain, and its placement can be seen in Fig. 2. The dimensions of the FineBox subdomain are related to the vehicle length (*L)*. In the simulation, we define the following set of dimensions for the FineBox subdomain: width (*WFB*), length (*LFB*), front length (*LFBF*), position of the center of gravity in the *x* direction ($CG_x$), and height (*HFB*). Most references for aerodynamics calculations suggest fixing the FineBox dimensions (labels are explained at Fig. 2) in vehicle length ranges *L* as:

$$W_{FB} \in [1,\ 1.5]L;\ \ L_{FB} \in [2,\ 2.5]L;\ \ F_{FBF} \in [1.5,\ 2]L;$$
$$(L_{FBF} - CG_x) \in [0.5,\ 1]L;\ \ \ H_{FB} \in [0.3,\ 0.5]L;$$

In the simulation, the fluid is air, under normal conditions. In Table 1, the set of simulation boundary conditions and values is presented. The mesh properties must satisfy certain flow constraints in order to model flow development correctly. Our simulation task began with setting up many mesh tests to determine the most convenient set of mesh parameters (Table 4). Tests were conducted to check for the convergence (value of residuals) of the method, as well as the convergence of drag and lift coefficients. Drag and lift coefficients behave in orthogonal way regarding the mesh setup. We can distinguish two types of mesh.*x*

**Table 1.** *Simulation boundary conditions*

| | |
|---|---|
| Inlet | posed on face $x > 0.15$ m/s, turbulence intensity 5 % |
| Outlet | posed on face $x < 0$ |
| Vehicle | wall type - no-Slip |
| Road | wall type - noShearStress,<br>posed on floor/road faces ($z = 0$) |
| Symmetry | posed on left, right and top face |

If a mesh is good for drag, it is not entirely true that is also acceptable for lift (and vice-versa). There is always interplay in a mesh setup to achieve good convergence properties in both directions (drag and lift). Comparison of a few mesh types showed that the convergence of a CFX numerical method is highly sensitive to the boundary layer mesh (BLM) type. Therefore, mesh construction for flow phenomena strongly depends on the BLM setup. One of the pillars in the setup of boundary layer parameters is the dimensionless wall distance $Y^+$, which controls the boundary mesh quality. A detailed explanation of this phenomenon can be found in [12]. In order to obtain the best mesh type, two inflation models/algorithms for boundary layer mesh generation were analyzed: FLT and FAR.

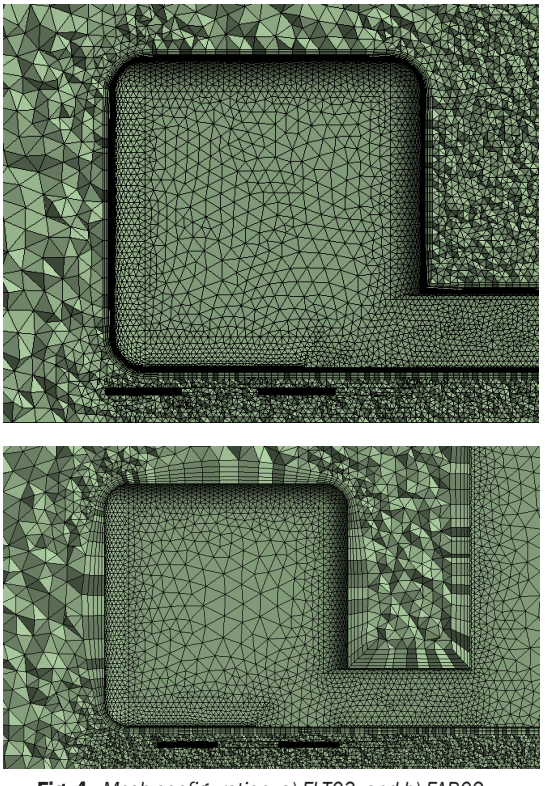


**Fig. 4.** *Mesh configuration; a) FLT03, and b) FAR02*

In Table 3, we present data that were constant within all mesh tests. Those parameters were constant for all simulation experiments and for all different mesh types. To find a reasonable mesh capable of sustaining convergence properties for drag and lift coefficients, seven mesh parameters were chosen to be varied. Table 3 presents different parameters used to create relatively different meshes.

The difference between the two inflation models, FLT and FAR, is clearly explained graphically in Fig. 4. The FLT algorithm (Fig. 4a) expands the boundary layer mesh parallel to the vehicle geometry, and the mesh uniformity is clearly visible. In contrast, the FAR algorithm (Fig. 4b) creates a boundary layer mesh in which cell height is dependent on the size of the face cell element attached to the vehicle surface.

The mesh is no longer uniform in the tangent direction of vehicle geometry.

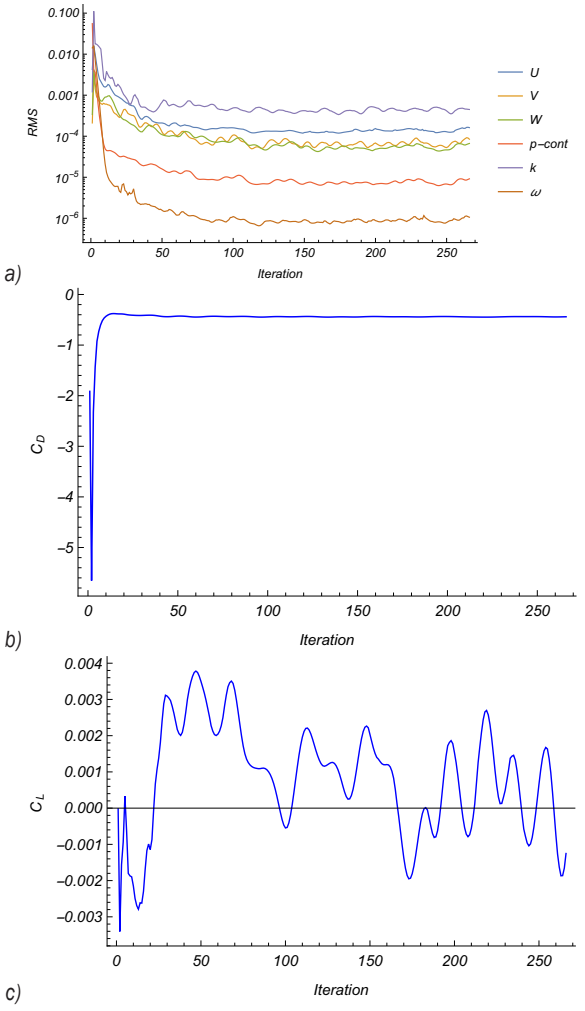


**Fig. 5.** *Convergence results for mesh FLT-03; a) residuals, b) drag coefficient and c) lift coefficient*

In Table 3, the results obtained with the FAR algorithm show that its inflation is considerably better than that of the FLT with respect to the SST turbulent model. This was unexpected in the simulation tests. We taught that nice uniform BLM should provide stable and more accurate results. Simulation tests for all meshes with a yaw angle of $\psi = 0°$ were stopped for the condition controlling residuals ($RMS \leq 10^{-5}$) or number of maximal iterations ($N_{max} \leq 450$). If a method did not converge (RMS condition) within $N_{max}$ iterations, it was considered not convergent. In Figs. 5 and 6, two different cases can be observed. Convergence results (RMS at Figs. 5a and 6a) show convergence of velocity components ($u$, $v$, $w$), pressure ($p$) and $k$-omega SST turbulence model variables ($k$, $\omega$).

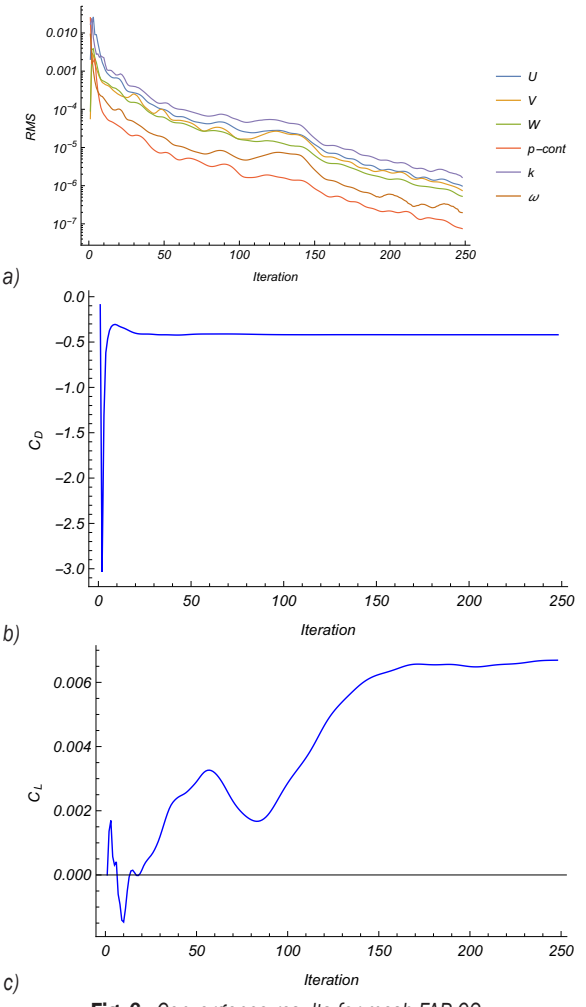


**Fig. 6.** *Convergence results for mesh FAR-02; a) residuals, b) drag coefficient, c) lift coefficient*

Convergence results (RMS) for the mesh type FLT-03 (Fig. 5a) clearly show that the method did not converge, and that the lift coefficient was highly unstable. The computed flow with an FLT mesh behaves in an unusual manner. In contrast, in Fig. 6, we show results for the mesh type FAR-02, with good method convergence and very good aerodynamic coefficient convergence. In Table 4 and Fig. 7, simulation results for drag and lift coefficients with respect to different mesh types are compared. They show clear evidence that the FAR mesh type has the desired characteristics. FAR mesh type results are spread in a narrow band, and show very small fluctuations with respect to different mesh parameters. The stability region of aerodynamic coefficients with respect to different mesh properties is, in the case of the FAR mesh, very confined. The stable properties of the FAR mesh type are even more evident, because the mesh parameters were varied over a wide interval.

The cause of such differences in FLT and FAR mesh types probably originates in the underlying turbulent model. Turbulent models are very sensitive to the type of boundary mesh.

The SST model performs much better with a FAR mesh type, because of the nature of its near-wall fluid turbulent motion filtering [9] and [12]. An FLT mesh type shows a completely different picture. Variations in the mesh properties result in vast fluctuations in the aerodynamic coefficients. It can be concluded that the FAR mesh type must be used to simulate external aerodynamics for the SST model.

Comparing all results (Table 4 and Fig. 7) for different mesh tests, it can be observed that mesh FAR-02 is a good candidate and has stable computational properties in simulations of the present external aerodynamic problem. The mesh is not too dense (i.e., it will not cause slow computations) and not too coarse (i.e., it will not produce the wrong coefficient results). Mesh FAR-02 was used in all computations in the analysis of aerodynamic coefficients. The aerodynamic coefficients are the non-dimensional representation of forces and moments of flow acting on a body (in our case, a vehicle).

**Table 2.** *Constant mesh data*

| Name | Sign | Unit | Value |
|---|---|---|---|
| far velocity | $U_\infty$ | m/s | 15 |
| inlet turbulent intensity | | % | 5 |
| boundary layer height | $H_{BL}$ | m | $3 \cdot 10^{-3}$ |

**Table 3.** *Mesh parameters; length/height dimensions are in millimeters*

| mesh type | domain | fine box | $H_1$ | $Y^+$ | inflation model | layers | GR |
|---|---|---|---|---|---|---|---|
| FLT-01 | 20 | 8 | 0.6 | 50 | FLT | 5 | 1.2 |
| FLT-02 | 20 | 6 | 0.1 | 10 | FLT | 10 | 1.2 |
| FLT-03 | 20 | 4 | 0.01 | 1 | FLT | 20 | 1.2 |
| FLT-04 | 20 | 4 | 0.001 | 0.085 | FLT | 35 | 1.2 |
| FLT-05 | 20 | 3.5 | 0.0005 | 0.04 | FLT | 35 | 1.2 |
| FAR-01 | 20 | 2 | - | - | FAR | 5 | 1.2 |
| FAR-02 | 15 | 5 | - | - | FAR | 5 | 1.2 |
| FAR-03 | 15 | 7 | - | - | FAR | 5 | 1.2 |

Domain cell size in basic domain
FineBox cell size in FineBox subdomain
$H_1$ height of first boundary layer cell (attached to the wall)
$Y^+$ calculated dimensionless wall distance with equations described in [12]
Inflation m. two inflation models were used FLT and FAR
Layers the number of layers in boundary layer mesh zone
GR the boundary layer mesh growth rate

Let us first define the aerodynamic force coefficient [6]:

$$C_F = \frac{F}{\frac{1}{2}\rho A U^2}, \tag{1}$$

where $F$ is the force magnitude in a specific direction, ρ is fluid density, $U$ is apparent wind velocity, and $A$ is the projected frontal vehicle area. When flow forces act on a vehicle, external moments also develop, due to the non-symmetry of vehicle geometry. As for the force aerodynamic coefficients, the aerodynamic coefficient for moment [6] can be defined, and is described by:

$$C_M = \frac{M}{\frac{1}{2}\rho A h U^2}, \tag{2}$$

where $M$ is the magnitude of the moment with respect to a specific axis and $h$ is a length scale parameter. Different authors choose different length scale parameters $h$ (for example vehicle height, vehicle length, or height of the center of gravity (CG)). We fix $h$ (Fig.s 1 and 8) to be the height of the CG ($H_{CG}$) in such a way that the pitch moment coefficient is 0 for yaw angle $\psi = 0°$.

In, Fig. 3 we show an illustration of the coordinate system orientation, vehicle rotation, and definition of force and moment coefficients in space. The coordinate system is always attached to the vehicle, and the apparent wind direction is described by yaw angle ψ. Simulation results were obtained from a fixed tunnel simulation experiment, with vehicle geometry being rotated around the $z$ axis passing through the CG. CFD simulation results of forces and moments were transformed from the tunnel coordinate system into the vehicle coordinate system (Fig. 3). The force aerodynamic coefficients are $C_D$ (drag – $x$ axis), $C_S$ (side – $y$ axis), and $C_L$ (lift – $z$ axis). The moment aerodynamic coefficients are $C_R$ (roll – over the $x$ axis), $C_P$ (pitch – over the $y$ axis), and $C_Y$ (yaw – over the $z$ axis). We must emphasize that the coefficients are not constant, and can change significantly depending on the apparent wind angle ψ. Data for the aerodynamic coefficients obtained from CFD calculation are discrete point set values. For the stability analysis, we must represent the aerodynamic coefficients in a functional form. How this can be achieved is explained in the next section.

Data fitting [14] is a science in its own right. In this section, a comparison of different fit models for the aerodynamic coefficients is presented. We introduce a new fit model to account for asymmetric

cases. The asymmetry in the results, shown in Fig. 9, motivated us in the search for a periodic but asymmetric function that can accurately fit the obtained computational data. The asymmetry can be incorporated into a combination of linear and cyclic functions. We propose the following piece-wise fit function:

$$g(x)=\begin{cases} y_L + k_L x + A_L \sin(\omega_L + \delta_L) \\ y_R + k_R x + A_R \sin(\omega_R + \delta_R) \end{cases}, \quad (3)$$

where index $L$ stands for $x \in [0, \pi/2]$ and index $R$ stands for $x \in [\pi/2, \pi]$. In Eq. (3), $x$ is the apparent wind angle $\psi$. Function $g(x)$ is continuous and must satisfy the continuity condition at point $x=\pi/2$. Function $g(x)$ must have an equal left and right limit at the mentioned point:

$$\lim_{x \uparrow \pi/2} g(x) = \lim_{x \downarrow \pi/2} g(x) .$$

Eq. (3) can account for asymmetry with respect to the point $x=\pi/2$. The coefficients can be expected to behave in a nonsymmetrical way due to the nonsymmetrical vehicle geometry. In most stability analysis cases, symmetrical relationships are used [4], [5] and [7], and we compare them with our simulation results. In order to complete the functional form of the aerodynamic coefficient, a CFD analysis must be performed for different apparent wind angles. In our case, this was accomplished for an angle interval from 0° to 180°, with constant angle increments of 10°. Smaller angle increments will probably not improve the accuracy of the chosen function form (Eq. (3)).

Computations were done in parallel (16 cores) and were completed within 10 d. For more complex vehicle geometries, computational time would probably multiple of 10 days. There is always interplay between computational time and computational accuracy. This dilemma was partially apparent in the mesh analysis section. Deeper mesh analysis for a variety of vehicle types is needed to be completely confident. In the calculation of aerodynamic coefficients (Eqs. (1) and (2)) we provide values for reference area $A$ (the projection of the frontal truck area onto the "$yz$" plane), free stream velocity $U$, fluid density ρ, and moment arm characteristic length $h$. The data used in the present simulations are shown in Table 1. CFD simulation results are obtained for pressure (index P) and viscous (index V) forces and moments ($\mathbf{F}_P$, $\mathbf{F}_V$, $\mathbf{M}_P$, $\mathbf{M}_V$) for different ψ. The present analysis does not focus on a separate analysis of pressure and viscous effects, but its magnitude and partial forces and moments must be summed:

$$\mathbf{F} = \mathbf{F}_P + \mathbf{F}_V = (F_x, F_y, F_z),$$
$$\mathbf{M} = \mathbf{M}_P + \mathbf{M}_V = (M_x, M_y, M_z).$$

Forces and moments are provided for all yaw angles. In Fig. 9, the results for aerodynamic coefficients are shown, and are compared for different fit models. Simulation data are compared with experimental data [8] and [15] obtained in a wind tunnel experiment. A comparison was performed for different inlet turbulent intensities and different measurements of the same object, as is investigated in the present study. The simulation data show very good agreement with the experimental data, except for pitch moment coefficient (CP). Experimental data from [8] and [15] show the same unusual CP behavior. The most probable cause of such unusual results lies in the sensitivity of the CP coefficient. Pitch moment can jump an order equal to its value for changes in the apparent window direction $\psi$, causing huge variations in CP. Given such fluctuations, it is almost impossible in a functional sense to correctly predict CP behavior. In Fig. 9, we show four fit functions: Fit-B1 are taken from [7], Fit-B2 are taken from [5], Fit-B3 are taken

**Table 4.** *Mesh test simulation parameters*

| i | mesh type | # Cells | # iter | Time/iter | CDrag | CLift | RMS | Converged |
|---|---|---|---|---|---|---|---|---|
| 1 | FLT-01 | 4,674,278 | 145 | 00:00:29 | –0.426 | –0.0337 | $10^{-5}$ | NO |
| 2 | FLT-02 | 6,308,164 | 765 | 00:00:42 | –0.430 | –0.0140 | $10^{-5}$ | NO |
| 3 | FLT-03 | 11,120,526 | 266 | 00:01:27 | –0.440 | –0.00204 | $10^{-5}$ | NO |
| 4 | FLT-04 | 11,898,277 | 177 | 00:01:49 | –0.464 | 0.0297 | $10^{-5}$ | NO |
| 5 | FLT-05 | 14,724,983 | 3126 | 00:01:04 | –0.446 | 0.0249 | $10^{-5}$ | NO |
| 6 | FAR-01 | 3,227,637 | 204 | 00:00:20 | –0.427 | –0.0227 | $10^{-5}$ | YES |
| 7 | FAR-02 | 8,621,470 | 1546 | 00:00:51 | –0.419 | –0.0214 | $10^{-5}$ | YES |
| 8 | FAR-03 | 16,081,773 | 1386 | 00:02:09 | –0.419 | –0.0218 | $10^{-5}$ | YES |
| 9 | FAR-01 | 3,227,637 | 536 | 00:00:20 | –0.427 | –0.0238 | $10^{-6}$ | YES |
| 10 | FAR-02 | 8,621,470 | 2486 | 00:00:50 | –0.419 | –0.0227 | $10^{-6}$ | YES |
| 11 | FAR-03 | 16,081,773 | 261 | 00:02:12 | –0.419 | –0.0237 | $10^{-6}$ | YES |

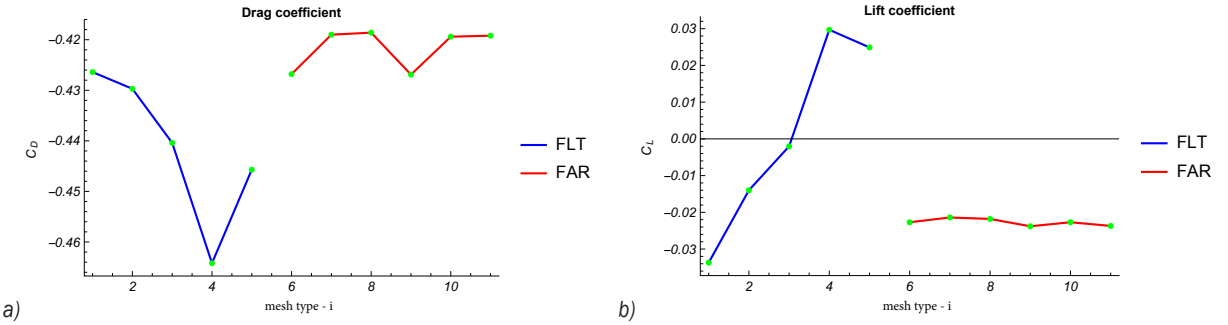


a) b)

**Fig. 7.** *Plot of a) drag and b) lift coefficients with respect to mesh type (Table 4)*

from [4] and $g(x)$ is the function in Eq. (3). With $S_1$, we show points obtained from the CFD simulations. The CFD results ($S_1$) fit almost perfectly and follow the same trends as experimental data, except for $C_P$.

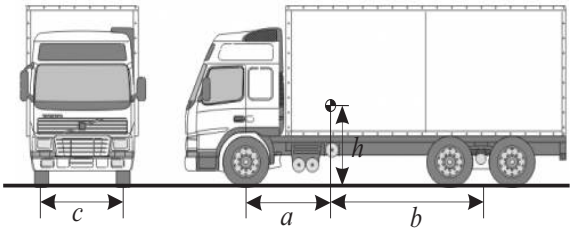


**Fig. 8.** *Vehicle dimensions*

As previously mentioned, the reason behind the large fluctuations and fit procedure for different fit functions produce evidently different behavior. In the present CFD analysis, simulations for angles greater than 90° were performed, and fill the gap in the data set compared to the experimental data in [8] and [15]. The CFD results show significant data shifting and asymmetry with respect to ψ. Reference fit functions *Fit-*$B_1$, *Fit-*$B_2$, and *Fit-*$B_3$ show very good fitting properties, although they have fewer degrees of freedom compared to the proposed function described in Eq. (3). Relationships similar to *Fit-*$B_1$ are mostly needed in analytic studies of crosswind effects, because of their simple but expressive form. In the case of coefficient $C_L$, the second minima (near 100°) can be observed, and was not predicted in the CFD analysis. Instead, it emerged as a fit result. One would expect that the force coefficients must reassemble symmetry around 90°; in the case of $C_L$, this occurred only with fitting result. Such evidence is not standard, and must be verified with additional CFD studies. As for the $C_P$, the oscillations are smeared, and the resulting fit function behaves very theoretically.

However, $C_L$ and $C_P$ are always somewhat "problematic" coefficients. The fit results in Fig. 9 are very informative, and show good agreement with the CFD results, except in the case of these "problematic" coefficients. We can conclude that the sets of fit functions presented in *Fit-*$B_1$, *Fit-*$B_2$ and *Fit-*$B_3$ have significant informative value, remembering that these are defined with only one or two coefficients.

We have compared four different sets of fit functions. The set of fit functions in Eq. (3) accommodates the results in a promising way. However, to be confident of the chosen fit function, it is highly desirable to test its form on a set of different types of vehicles, and verify its structure. This is reserved for future research.

## 2 AERODYNAMIC STABILITY ANALYSIS

This section covers the aerodynamic stability analysis of the vehicle studied in Sect. 1. An essential element of this method is the relationship between wind speed, truck speed, and aerodynamic forces for a particular vehicle and site.

**Table 5.** *Geometry and wind parameters*

| Name | Symbol | Unit | Value |
|---|---|---|---|
| air density | $\rho$ | kg/m$^3$ | 1.185 |
| front area | $A$ | m$^2$ | 0.00405 |
| velocity | $U$ | m/s | 15.0 |
| moment arm | $h$ | m | 0.068396 |
| mass | $m$ | kg | 10000 |

Traditionally, these aerodynamic characteristics have been studied with scaled-model wind tunnel tests [16] and [17]. In contrast, this study uses the CFD method described in Sect. 1 for these purposes. Experiments are costly and the required special equipment is not widely available, which poses a serious problem for wind tunnel experiments. Recent and similar works [1] and [18] to [20] performed a similar analysis under different circumstances in a

crosswind situation. In this study, we use the stability criteria relationship derived in [2] to analyze three crosswind accident types: rollover, side-slip or lateral-slip, and rotation.

### 2.1 Rollover

The first indication of possible vehicle rollover occurs when a wheel loses contact with the road.

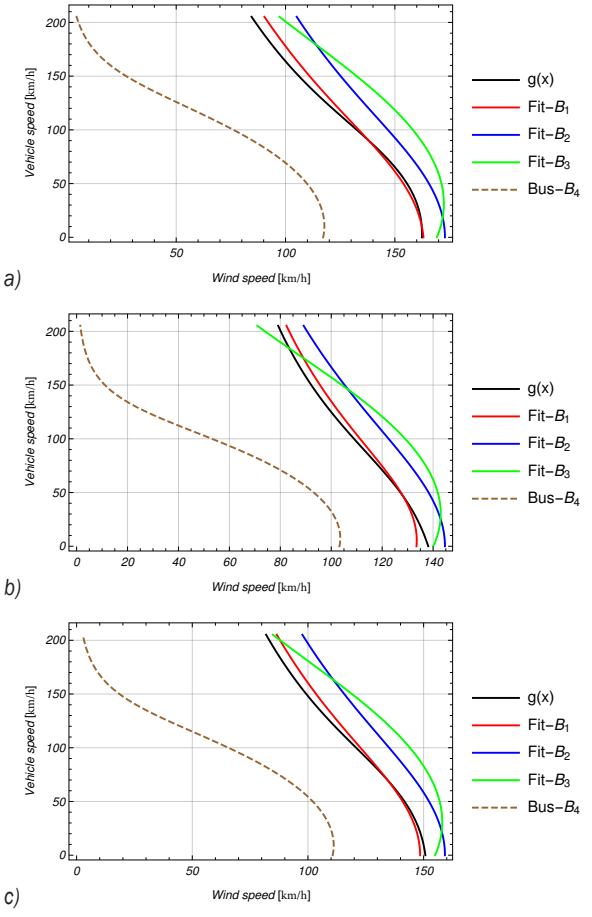


**Fig. 10.** *Solution of a) $V_{\text{loose1}}$, b) $V_{\text{loose2}}$, and c) $V_{\text{roolover}}$*

To determine which wheel will lose contact, we use Eqs. (4) and (5) (derived in [2]) to calculate the critical apparent wind speed magnitude for the front ($V_{\text{loose1}}$) and rear ($V_{\text{loose2}}$) wheels. If both wheels lose contact simultaneously, then we calculate critical velocity with Eq. (6). The rollover results are shown in Fig. 10. In addition to fit results, the comparison to the coefficients defined in [4] for the Leyland Atlantean bus are shown with the label Bus-$B_4$.

$$V_{\text{loose1}} = \sqrt{\frac{2mg}{\rho A}\frac{bc}{h(a+b)(C_S+C_R)+hc(C_D+C_P)+bcC_L}}, \quad (4)$$

$$V_{\text{loose2}} = \sqrt{\frac{2mg}{\rho A}\frac{ac}{h(a+b)(C_S+C_R)-hc(C_D+C_P)+acC_L}}, \quad (5)$$

$$V_{\text{rollover}} = \sqrt{\frac{2mg}{\rho A}\frac{c}{2h(C_S+C_R)+cC_L}}. \quad (6)$$

### 2.2 Rotation

The vehicle reaches a rotation condition if the side forces on one of its axles reach the friction limit. Eq. (7) ($V_{\text{slip1}}$), derived in [2], describes the magnitude of the critical apparent wind speed that will slip the front axle wheels. Eq. (8) ($V_{\text{slip2}}$), derived in [2], describes the magnitude of the critical apparent wind speed for which the back axle wheels lose contact. The critical condition rotation results are shown in Fig. 11.

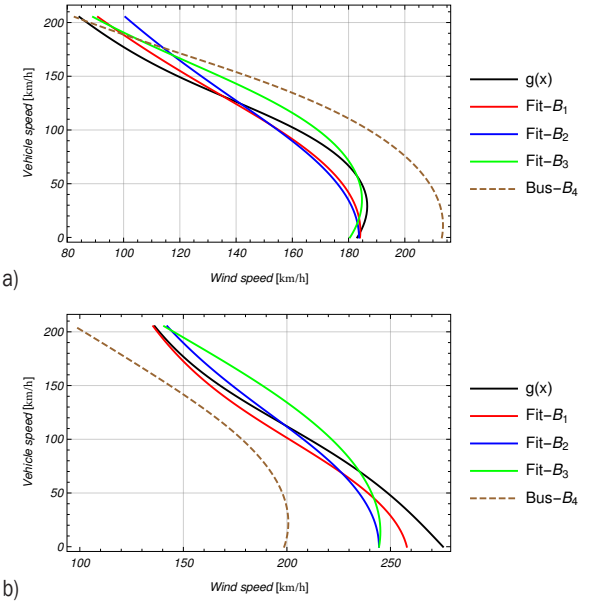


**Fig. 11.** *Solution of a) $V_{\text{slip1}}$ and b) $V_{\text{slip2}}$*

$$V_{\text{slip1}} = \sqrt{\frac{2mg}{\rho A}\frac{\mu_1 b}{bC_S+h\left[C_Y-q'(C_S+C_R)\right]+\mu_1\left[bC_L+h(C_D+C_P)\right]}}, \quad (7)$$

$$V_{\text{slip2}} = \sqrt{\frac{2mg}{\rho A}\frac{\mu_2 a}{aC_S-h\left[C_Y-q'(C_S+C_R)\right]+\mu_2\left[aC_L-h(C_D+C_P)\right]}}. \quad (8)$$

### 2.3 Side Slip or Lateral Slip

The side-slip or lateral-slip criterion is reached when all vehicle wheels simultaneously reach the friction limit from sideway force. Eq. (9), derived in [2], describes the relationship for the critical apparent

wind speed for side-slip and. The results of critical conditions can be seen in Fig. 12.

$$V_{\text{sideslip}} = \sqrt{\frac{2mg}{\rho A}\frac{a\mu_2 + b\mu_1}{(a+b)C_S + (a\mu_2 + b\mu_1)C_L + (\mu_1 - \mu_2)h(C_D + C_P)}}. \quad (9)$$

For all three mentioned cases, the relationship between vehicle and wind speed is implicit, and requires a numerical solution. The most severe and fatal situations occur for cases where the apparent wind blows perpendicularly to the vehicle.

## 3 CONCLUSIONS

In this study, a CFD analysis of vehicle external aerodynamics is compared with experimental data for a crosswind situation. The primary goal of the present numerical analysis is the analysis of vehicle stability under crosswind influence. A traditional analysis of vehicle stability under wind influence using a multi-body approach requires only aerodynamic coefficients to set up the external forces problem. The analysis of crosswind conditions under which a vehicle will roll over, side-slip, or rotate is highly sensitive to wind direction (external force direction). To derive accurate conditions, we must provide relationships for aerodynamic coefficients that are dependent on the direction of external force. Such information is almost never available to researchers, and this was the primary goal of the present study.

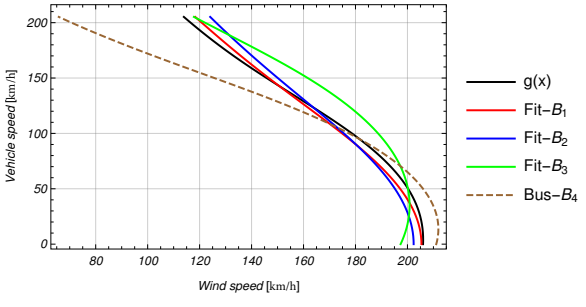


**Fig. 12.** *Solution of* $V_{\text{side-slip}}$

We describe a complete framework for the calculation of aerodynamic coefficients under high crosswinds. First, the mesh type is analyzed. Later, a CFD analysis is described, in order to provide accurate results. Finally, simulation results are compared to experimental data **[8]** and **[15]**. The results show good agreement between the experiments and simulations, except for critical cases in which the experimental data have no rational explanation. One important question is: which function should we use to accurately fit the simulation data? The simulation showed that there are significant discrepancies from symmetric geometrical situation. We proposed a piece-wise function $g(x)$ - Eq. (3) to account for data shifting and asymmetry. All simulation data were fit to $g(x)$, and the results are shown in Fig. 9. The results match the simulation data well. In particular, they reveal some hidden behavior with respect to lift and pitch coefficients. Reference fit functions *Fit-*$B_1$, *Fit-*$B_2$, and *Fit-*$B_3$ show very good agreement, although they incorporate significantly fewer degrees of freedom. In the application, the results obtained with fit models were used to estimate critical aerodynamic stability parameters. Rollover, rotation, and side-slip results were obtained. As expected, the results show some differences depending on the fit model. The most important data are the lower bound predictions for critical speeds. A general observation is that there is a lower bound path defined within the family of fit models. This marginal path can be taken as the worst-case scenario for critical wind-vehicle speeds, and can be used in the analysis of wind safety regulations.

## REFERENCES


**[1]** Choi, H., Lee, J., Park, H. (2014). Aerodynamics of Heavy Vehicles. Annual Review of Fluid Mechanics, vol.46, n. 1, p. 441-468, **DOI:10.1146/annurev-fluid-011212-140616**.

**[2]** Batista, M., Perkovič, M. (2014). A simple static analysis of moving road vehicle under crosswind. *Journal of Wind Engineering and Industrial Aerodynamics*, vol. 128, p. 105-113, **DOI:10.1016/j.jweia.2014.02.009**.

**[3]** Hucho, W.H. (2013). *Aerodynamics of road vehicles: from fluid mechanics to vehicle engineering*. Elsevier.

**[4]** Baker, C. (1986). A simplified analysis of various types of wind-induced road vehicle accidents. *Journal of Wind Engineering and Industrial Aerodynamics*, vol. 22, n. 1, p. 69-85, **DOI:10.1016/0167-6105(86)90012-7.**

**[5]** Baker, C. (1988). High sided articulated road vehicles in strong cross winds. *Journal of Wind Engineering and Industrial Aerodynamics*, vol. 31, n. 1, p. 67-85, **DOI:10.1016/0167-6105(88)90188-2.**

**[6]** Baker, C. (1991). Ground vehicles in high cross winds part I: steady aerodynamic forces. *Journal of Fluids and Structures*, vol. 5, n.1, p. 69-90, **DOI:10.1016/0889-9746(91)80012-3**.

**[7]** Snæbjörnsson, J.T., C. Baker, Sigbjörnsson, R. (2007). Probabilistic assessment of road vehicle safety in windy environments. *Journal of Wind Engineering and Industrial Aerodynamics*, vol. 95, no. 5, p. 1445-1462, **DOI:10.1016/j.jweia.2007.02.020**.

**[8]** Coleman, S., Baker C. (1994). An experimental study of the aerodynamic behaviour of high sided lorries in cross winds. *Journal of Wind Engineering and Industrial Aerodynamics*, vol. 53, no. 3, p. 401-429, **DOI:10.1016/0167-6105(94)90093-0**.

**[9]** Menter, F.R. (2009). Review of the shear-stress transport turbulence model experience from an industrial perspective.

*International Journal of Computational Fluid Dynamics*, vol. 23, n. 4, p. 305-316, **DOI:10.1080/10618560902773387**.

**[10]** Ferziger, J.H., Perić, M. (2012). *Computational Methods for Fluid Dynamics*. Springer Science & Business Media.

**[11]** Patankar, S. (1980). *Numerical Heat Transfer and Fluid Flow*. CRC press.

**[12]** Pope, S.B. (2001). Turbulent Flows. IOP Publishing, **DOI:10.1088/0957-0233/12/11/705**.

**[13]** Schlichting, H., Gersten, K. (2003). *Boundary-Layer Theory*. Springer Science & Business Media.

**[14]** Quarteroni, A., Sacco, R., Saleri, F. (2010). *Numerical Mathematics*. Springer Science & Business Media.

**[15]** Baker, C.J. (1987). Measures to Control Vehicle Movement at Exposed Sites during Windy Periods. *Journal of Wind Engineering and Industrial Aerodynamics*, vol. 25, n. 2, p. 151-161, **DOI:10.1016/0167-6105(87)90013-4**.

**[16]** Cheli, F., Corradi, R., Sabbioni, E., Tomasini, G., (2011). Wind tunnel tests on heavy road vehicles: Cross wind induced loads-Part 1. Journal of Wind Engineering and Industrial Aerodynamics, vol. 99, n. 10, p. 1000-1010, **DOI:10.1016/0167-6105(87)90013-4**.

**[17]** Cheli, F., Corradi, R., Sabbioni, E., Tomasini, G., (2011). Wind tunnel tests on heavy road vehicles: Cross wind induced loads-Part 2. *Journal of Wind Engineering and Industrial Aerodynamics*, vol. 99, n. 10, p. 1011-1024, **DOI:10.1016/j.jweia.2011.07.007**.

**[18]** Bettle, J., Holloway, A.G.L., Venart, J.E.S. (2003). A computational study of the aerodynamic forces acting on a tractor-trailer vehicle on a bridge in cross-wind. *Journal of Wind Engineering and Industrial Aerodynamics*, vol. 91, n. 5, p. 573-592, **DOI:10.1016/S0167-6105(02)00461-0**.

**[19]** Cai, C.S., Hu, J., Chen, S., Han, Y., Zhang, W. and Kong, X. (2015). A coupled wind-vehicle-bridge system and its applications: a review. *Wind and Structures*, vol. 20, n. 2, p. 117-142, **DOI:10.12989/was.2015.20.2.117**.

**[20]** Iljaž, J., Škerget, L., Štrakl, M., Marn, J. (2016). Optimization of SAE Formula Rear Wing. *Strojniški Vestnik-Journal of Mechanical Engineering*, vol. 62. n. 5, p. 263-272, **DOI:10.5545/sv-jme.2016.3240**.

Strojniški vestnik - Journal of Mechanical Engineering 63(2017)3, 201-211

DOI:10.5545/sv-jme.2016.3557 Original Scientific Paper
Received for review: 2016-03-05
Received revised form: 2016-12-12
Accepted for publication: 2017-01-31

# Determination of the Threshold for Extreme Load Extrapolation Based on Multi-Criteria Decision-Making Technology

Jixin Wang – Xinting Zhai* – Cheng Liu – Yingshuang Zhang
Jilin University, School of Mechanical Science and Engineering, China

*The peak over threshold (POT) model is commonly used in extreme load extrapolation. Due to the important role that the threshold plays in establishing a POT model, a method to select the suitable threshold is designed based on multi-criteria decision-making (MCDM) technology. The mean deviation in probability distribution function, Kolmogorov-Smirnov test, and Chi-Square test are employed as the test criteria. An entropy method is applied to obtain the weight values of these tests. The VIKOR method is adopted to obtain compromise solutions according to the corresponding criteria and weight values. The POT requirement is used to determine a suitable threshold. The effectiveness and feasibility of this method are validated by the load time history measured in experiment and generated by simulation. A comparative analysis between this method and two other common methods is also conducted. The proposed method based on MCDM shows better performance.*
**Keywords: peak over threshold (POT), extreme load extrapolation, threshold, multi-criteria decision-making (MCDM), entropy method, VIKOR**

**Highlights**
- *Multi-criteria decision-making technology is adopted.*
- *Simulation is used to show the good performance of the method.*
- *The result is closer to the true threshold value with more intervals.*
- *The superiority of the MCDM method is shown through comparative analysis.*

## 0 INTRODUCTION

Engineering vehicle components often suffer from random loads because they work in harsh environments and on bumpy roads [1]. Frequent fatigue failures often occurred [2]. The fatigue behaviour assessment for the mechanical components is traditionally conducted in time-domain [3]. The ultimate limit state analysis caused by the extreme working conditions is often considered [4]. Thompson estimated the return level associated with a particular return period to improve the coastal defence structure design.[5]. Wang determined that the extreme loads have significant impact on damage [6]. Because acquiring the actual load time history is time-consuming and costly, only limited time periods of load can be performed [7]. The extreme loads cannot be measured through limited time [8]. Therefore, in the above procedures, extrapolation is used to transfer limited periods load to longer periods load, especially to a design life [9]. During the process of extrapolation, extreme loads occurred more than before [10]. Through the extreme load extrapolation, the load amplitude and frequency can be properly estimated, which provides reasonable data for fatigue analysis.

The extreme value theory is applied to solve the problem of extreme load extrapolation. There are three models to determine the extreme values. The first model divides the load time history into blocks and picks the extreme value in each block for analysis; this is called block maximum method (BMM) [11]. The second is named peak over threshold (POT) [12], which is based on the exceedances over a threshold. The third is called the method of independent storm (MIS) [13], which is the combination of the former two methods. The data above the threshold are divided into blocks, and the extreme values of each block are extracted. The BMM and MIS both need large sample data. In this paper, the POT model is applied; the main idea of that model for extreme loads extrapolation is based on a random simulation of the high maxima and low minima. Only the maxima above a level umax, and the minima below a low load level umin are randomly regenerated. The level umax and umin are collectively called the threshold. In this paper, we propose a method based on multi-criteria decision-making (MCDM) technology to select a suitable threshold.

The concept of the POT model was first introduced by Pickands [14]. Set a sample of load data $X=(x_1,x_2,...,x_3)$. They are independent and identically distributed and belong to an unknown continuous distribution. Suppose u is the threshold, the extreme exceedances over the level u are modelled: $y_i = x_i\big|_{x_i>u} - u$ . The distribution function of the exceedances $F_u(y)$ is given by:

$$F_u(y)=\mathrm{P}(x-u<y\,|\,x>u)=\frac{F(u+y)-F(u)}{1-F(u)}. \quad (1)$$

*Corr. Author's Address: School of Mechanical Science and Engineering, Jilin University, Changchun, China, zxt00900@sina.com

When $u$ is set high enough, then under certain conditions, the distribution function of these exceedances $F_u(y)$ approximately follow the Generalized Pareto Distribution (GPD). The distribution is defined in Eq. (2). Where $\xi$ and $\sigma$ are the shape parameter and scale parameter, respectively.

$$G(x|u,\xi,\sigma)=\begin{cases}1-(1+\xi\dfrac{x-u}{\sigma})^{-\frac{1}{\xi}}, & \xi\neq 0\\ 1-\exp(-\dfrac{x-u}{\sigma}), & \xi=0\end{cases}. \quad (2)$$

The traditional threshold selection method uses graphical diagnostics to make an initial threshold choice. The mean residual life (MRL) [15] method chooses the lowest level as the threshold because the mean exceedance over a level $u$ is a linear function of the level $u$. The hill plot [16] method prefers the largest value of the hill estimator after it becomes stabilized, which means the lowest data would be chosen as the threshold. The advantage of these two approaches is that the results can be graphically inspected and assessed. The subjectivity and the rich experience are required in these methods.

In contrast to the above graphical methods, the numerical approaches are objective and automatic. Beirlant et al. [17] and Ferreira et al. [18] used the mean square error (MSE) method and set the value corresponding to the minimum MSE as the best threshold. Johannesson [10] proposed a load extrapolation method based on the POT model, and the threshold is determined by the exceedance number $\sqrt{N_0}$ and $N_0$ is the load cycles of the load time history. Thompson et al. [5] proposed an automatic threshold selection method, which builds a new parameter, and selects the appropriate threshold according to the distribution of the parameter. In order to obtain the extreme wave values, Mazas and Hamm [19] used the dual-threshold method to calculate wave heights. The first threshold is used to extract load peaks from the load time history, and the extracted data follow the GPD. The second threshold is determined when the corresponding shape parameter and the improved scale parameter maintain a constant.

The results (threshold) obtained through the above methods may be different. Many numerical test criteria are used to verify the fitting accuracy of the GPD with the corresponding selected threshold. Each of the methods may perform well under certain criteria and may be assumed as the best method. In order to select a threshold establishing a POT model, the joint influence of multi-criteria should be taken into consideration. MCDM works when the practical problems are characterized by several conflicting criteria.

In this paper, a method named MCDM is proposed to select a threshold. An entropy method is used to measure the weight value of each criterion for its objectivity [20] and [21]. The VIKOR [22] to [24] is an MCDM technology. It proposes compromise solutions from a series of candidates by ranking them based on several conflicting criteria. According to the POT requirement, the minimum value of the compromise solutions is set as the suitable result. The method using MCDM is presented in detail in Section 1. In Section 2, the validity of the MCDM method is illustrated by the load time history and simulated data. Finally, comparison analysis and conclusions are presented.

## 1 METHODOLOGY

For a load data set, once a value is set as the threshold, the corresponding mathematical expression of GPD can be obtained after parameter estimation. Test criteria are used, and test values show the fitting accuracy of the GPD. The entropy method is used to determine the weight value of each criterion. Based on the MCDM, the compromise solutions are obtained by integrating the criteria into a synthetic indicator. Through the POT requirement, the suitable threshold is determined. The process chart of obtaining a suitable threshold $u^*$ is shown in Fig. 1.

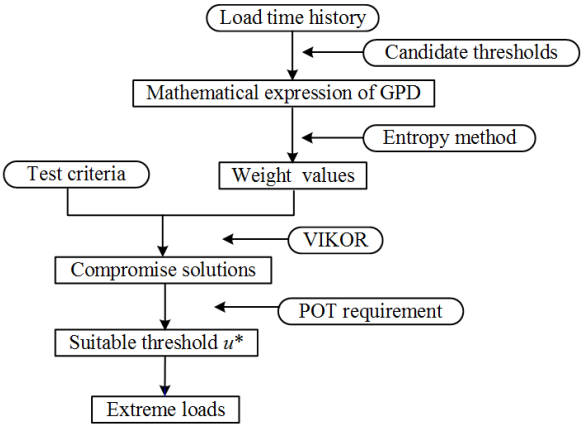


**Fig. 1.** *Process chart of the MCDM method*

### 1.1 Determination of the Initial Scope

The load time history can be viewed as a sequence of turning points [10]. According to the character of the load distribution and with the aim of improving the efficiency of calculation, candidate thresholds

$(u_1, ..., u_m)$ are set in ascending order. Set the load data value in an ascending order. $u_1$ is the value in the middle place of the data length, and $u_m$ is the 98 % quantile of the data. $m$ equally spaced candidate thresholds exist between $u_1$ and $u_m$. The corresponding $\xi_i$ $(i=1,\ldots,m)$ and $\sigma_i$ $(i=1,\ldots,m)$ are the parameters obtained by maximum likelihood estimation (MLE). Then the mathematical expressions of GPD are obtained for candidate thresholds.

### 1.2 Determination of the Criteria

The principles of test criteria are different and can be reflected by different results. Thus, three test criteria are used in the present study: mean deviation in probability distribution function (PDF), Kolmogorov-Smirnov (K-S) test and Chi-Square ($\chi^2$) test [25] and [26].

#### *1.2.1 Mean Deviation in PDF*

The mean deviation between the theoretical PDF and the empirical PDF are shown by $\delta_{\text{pdf}}$ in Eq. (3).

$$\delta_{\text{pdf}} = \frac{1}{l}\sum_{i=1}^{l}\left|f(x_i)-g(x_i)\right|. \tag{3}$$

#### *1.2.2 K-S test*

The test value is the greater deviation value of the theoretical cumulative distribution function (CDF) and empirical CDF, which is calculated in Eq. (4).

$$K_{max} = \max_{1\le j\le l-1}\left\{\left|F(x_i)-G(x_i)\right|,\left|F(x_{i+1})-G(x_i)\right|\right\}. \tag{4}$$

#### 1.2.3 $\chi^2$ test

Assume $O_i$ is the observed frequency and $E_i$ is the expected frequency. Then $\chi^2$ represents the deviation between them.

$$\chi^2 = \sum_{i=1}^{l}\frac{(O_i-E_i)^2}{E_i}. \tag{5}$$

### 1.3 Determination of the Weight Values of Criteria

For each candidate threshold, a test value will be obtained under a certain criterion. For a series of candidate thresholds and three test criteria, there will be many test values. Each of them has its role in evaluating fitting accuracy. To find a suitable threshold under three criteria, these criteria should be taken into consideration simultaneously. Taking account of the different principle of test criteria, the larger the weight value, the more important will the test criterion be. Thus, the weight values of criteria should be settled and the entropy method is used for its objectivity.

The number of candidate threshold is $m$, and $n$ shows the number of test criterion. Thus, the test values $r_{ij}$ of candidate threshold $i$ under the criterion $j$ form a decision matrix $RR$.

$$RR = \begin{bmatrix} r_{11} & r_{12} & \cdots & r_{1n} \\ r_{21} & r_{ij} & \cdots & r_{2n} \\ \vdots & \vdots & \ddots & \vdots \\ r_{m1} & r_{m2} & \cdots & r_{mn} \end{bmatrix}. \tag{6}$$

Then, the normalized matrix $RR$, $r_{ij}$ is transformed by the Eq. (7). And $H$ is obtained by keeping the effect of each criterion.

$$h_{ij} = r_{ij} / \sum_{i=1}^{m} r_{ij} \qquad i=1,2,...,m \qquad j=1,2,...,n, \tag{7}$$

$$H = \begin{bmatrix} h_{11} & h_{12} & \cdots & h_{1n} \\ h_{21} & h_{ij} & \cdots & h_{2n} \\ \vdots & \vdots & \ddots & \vdots \\ h_{m1} & h_{m2} & \cdots & h_{mn} \end{bmatrix}. \tag{8}$$

The relative importance of each criterion is expressed by $E_j$, which is the $j^{\text{th}}$ entropy value and can be obtained from the following formulas:

$$E_j = -\frac{1}{\ln m}\sum_{i=1}^{m} h_{ij}\ln h_{ij}. \tag{9}$$

Suppose $h_{ij}\ln h_{ij}=0$ when $h_{ij}=0$. Then the weight of entropy of $j^{\text{th}}$ criterion is defined as:

$$\omega_j = (1-E_j)/(n-\sum_{j=1}^{n} E_j), \tag{10}$$

where $0 \le \omega_j \le 1$ and $\sum_{j=1}^{n}\omega_j = 1$.

### 1.4 Determination of the Compromise Solutions by MCDM

Among the MCDM technologies, VIKOR is used. Another commonly used MCDM method, the technique for order preference by similarity to an ideal solution (TOPSIS), finds a solution that satisfies the constraints that the distance from the positive-ideal solution (PIS) is the nearest while from the negative-ideal solution (NIS) is the farthest. However, it does not take the relative importance of these distances into consideration [22] and [24]. In contrast, VIKOR redresses this shortage and introduces a multi-

criterion ranking index based on a measurement of "closeness" to the "ideal" solution. According to the VIKOR method, the best feasible solution is also called compromise solutions, which contains one or more values.

#### *1.4.1 Normalization*

Through the vector normalization, shown in Eq. (11), the matrix $T$ is obtained.

$$t_{ij} = r_{ij} / \sqrt{\sum_{i=1}^{m} r_{ij}^2} \quad i = 1,2,...,m \quad j = 1,2,...,n, \quad (11)$$

$$T = \begin{bmatrix} t_{11} & t_{12} & \cdots & t_{1n} \\ t_{21} & t_{ij} & \cdots & t_{2n} \\ \vdots & \vdots & \ddots & \vdots \\ t_{m1} & t_{m2} & \cdots & t_{mn} \end{bmatrix}. \quad (12)$$

#### 1.4.2 PIS $t_j^*$ and NIS $t_j^-$

Determine PIS $t_j^*$ and NIS $t_j^-$ of all criterion functions:

The PIS is the best value and the NIS is the worst value of all candidate thresholds on every criterion.

$$\text{Benefit index} \quad \begin{cases} t_j^* = \max\limits_{1\le i\le m} t_{ij} \\ t_j^- = \min\limits_{1\le i\le m} t_{ij} \end{cases}, j = 1,2,...,n, \quad (13)$$

$$\text{Cost index} \quad \begin{cases} t_j^* = \min\limits_{1\le i\le m} t_{ij} \\ t_j^- = \max\limits_{1\le i\le m} t_{ij} \end{cases}, j = 1,2,...,n. \quad (14)$$

#### *1.4.3 Group Utility $S$ and Individual Regret $R$*

Calculate the group utility $S$ and individual regret $R$ using Eqs. (15) and (16):

$$S_i = \sum_{j=1}^{n} [\omega_j (t_j^* - t_{ij}) / (t_j^* - t_j^-)] \quad i = 1,2,...,m, \quad (15)$$

$$R_i = \max_{1\le j\le n} [\omega_j (t_j^* - t_{ij}) / (t_j^* - t_j^-)] \quad i = 1,2,...,m, \quad (16)$$

where $\omega_j$ obtained by the entropy method in VIKOR is the weight of $j^{\text{th}}$ criteria.

#### *1.4.4 Interest Rate $Q$*

The interest rate $Q$ is calculated with the equation below:

$$Q_i = \frac{v(S_i - S^*)}{S^- - S^*} + \frac{(1-v)(R_i - R^*)}{R^- - R^*}, i = 1,2,...,m, \quad (17)$$

where $S^* = \min\limits_{1\le i\le m} S_i$ is the minimum of group utility, and $S^- = \max\limits_{1\le i\le m} S_i$ is the maximum group utility. The opponent of group utility is the individual regret. The minimum of individual regret is $R^* = \min\limits_{1\le i\le m} R_i$, and $R^- = \max\limits_{1\le i\le m} R_i$ the maximum individual regret. The value $v$ is the decision-making mechanism factor. In order to balance the relationship between group utility and individual regret, set $v = 0.5$.

#### *1.4.5 Conditions*

The $Q$ values are arranged in ascending order with the corresponding $S$ and $R$. The candidate $X_1$ corresponding to the minimum $Q$ is the best solution when the following two conditions are satisfied:

C1: Acceptable advantage: $Q_2 - Q_1 \ge 1/(m-1)$ where $Q_2$ is the corresponding $Q$ value of $X_2$, and $X_2$ is the alternative with second place in the ranking $Q$ and m is the number of candidates.

C2: Acceptable stability in decision making: the $S$ value or $R$ value of $X_1$ is the best ranked.

#### *1.4.6 Compromise Solutions*

Compromise solutions can be obtained if one of the conditions is not satisfied. If the results only conform to C1, both alternatives are suitable. If only C2 is satisfied, $X_1, X_2, ..., X_M$ are the compromise solutions. The subscript $M$ is the number of the solution, and $X_M$ is determined by Eq. $Q_M - Q_1 < 1/(m-1)$ for maximum $M$ value.

### 1.5 Determination of Suitable Threshold by POT Requirement

According to 1.4.6, the compromise solutions could be concluded as $X_1, X_2, ..., X_M$.

The compromise solutions include one or more values. If the maximum value is selected as the suitable threshold within the limited load sample, some information will be lost. According to the concept of the POT model, it is advantageous to select the minimum value on the premise of satisfying the fitting accuracy of GPD. Because preserving more data is conducive to the effective use of the data information, which is called the POT requirement in this paper. Thus, the suitable threshold $u^*$ is shown in Eq. (18):

$$u^* = \min_{1\le i\le M} (X_i). \quad (18)$$

## 2 CASE STUDY

### 2.1 Load Time History Analysis of Wheel Loader Axle Shaft

Fig. 2 is the torque data acquisition process of a wheel loader axle shaft. Fig. 2a is the operation mode. It can be seen as the letter "V". Six sections are known as V1, V2, V3, V4, V5 and V6. The spading section V2 is studied because of the obvious load fluctuation. Fig. 2b is the load-time data of wheel loader axle shaft of the V2 section. Assume that loads are independent and identically distributed.

There are 1049 turning points obtained by filtered rain flow, and the load value is from 71.33 Nm to 4123.63 Nm. The range of the initial threshold $[u_1, u_m]$ is $[1806.32, 3498.61]$. Set $m=50$ and pick every alternative as a candidate threshold, and the data points above the threshold are left to obtain mathematical expression of GPD with the help of MLE. The test values of mean deviation in PDF, K-S test, and $\chi^2$ test are shown in Fig. 3. The trends of curves for different test criteria are different.

According to the procedure in Section 1.3, the weight values of the corresponding test criterion obtained by entropy method are [0.001 0.358 0.641]. According to the procedure in Section 1.4. The weight value is obtained based on $Q_i$, $S_i$ and $R_i$ ($i$=1, 2,…, $m$) and they are obtained using the VIKOR method.

**Table 1.** *Rank order of $Q_i$, $S_i$ and $R_i$ (50×6)*

| $u$ | $Q_i$ | Rank | $S_i$ | Rank | $R_i$ | Rank |
|---|---|---|---|---|---|---|
| 2517.082 | 0.016147 | 1 | 0.147023 | 2 | 0.094584 | 1 |
| 2957.077 | 0.018547 | 2 | 0.130509 | 1 | 0.11486 | 8 |
| 2855.54 | 0.035569 | 3 | 0.166259 | 6 | 0.095254 | 2 |
| 2923.231 | 0.041232 | 4 | 0.161069 | 5 | 0.106992 | 5 |
| … | … | … | … | … | … | … |
| 3464.764 | 0.466029 | 48 | 0.359967 | 48 | 0.358786 | 48 |
| 1840.166 | 0.679164 | 49 | 0.472336 | 49 | 0.471677 | 49 |
| 1806.32 | 1 | 50 | 0.64187 | 50 | 0.641205 | 50 |

The rank number of each value of $Q$, $S$ and $R$ are marked, which can aid in obtaining the compromise solutions. The values in Table 1 are displayed in ascending order of $Q$. Next, the number of thresholds is 50, i.e. $m=50$. According to C1 and C2, the result of Eq. $1/(m-1)$ is 0.0204. Seen in Table 1, $Q_2-Q_1<0.0204$ and $Q_3-Q_1<0.0204$, while

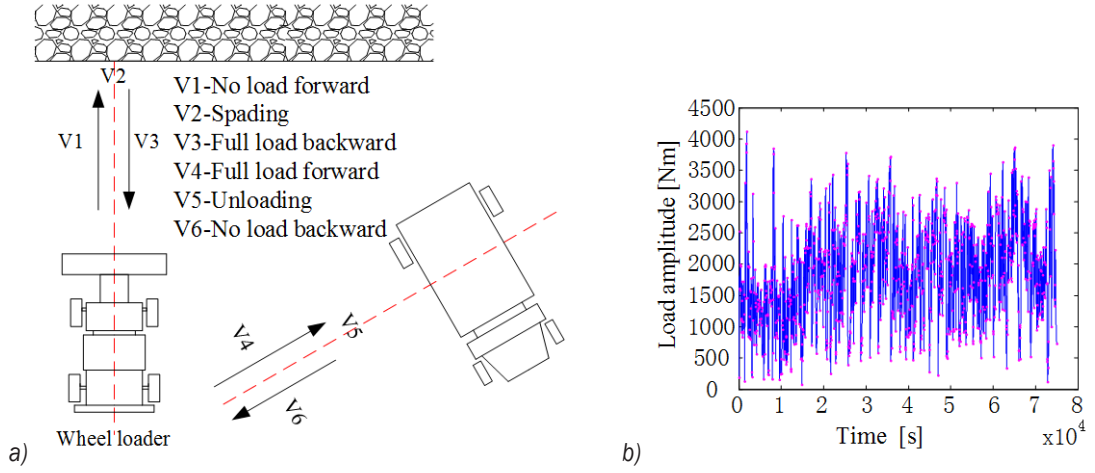


**Fig. 2.** *Data acquisition of wheel loader axle shaft; a) operation mode of wheel loader; b) load data of wheel loader axle shaft from spading section*

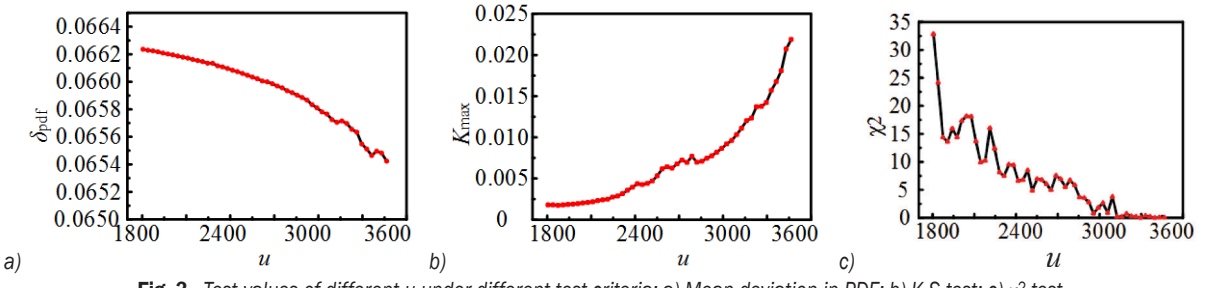


**Fig. 3.** *Test values of different u under different test criteria; a) Mean deviation in PDF; b) K-S test; c) $\chi^2$ test*

$Q_4 - Q_1 > 0.0204$. At the same time, both $R_2$ and $R_3$ are smaller than $R_1$. Thus, three candidates are finally picked as compromise solutions of the case. The results are shown in Table 2.

**Table 2.** *Compromise solutions of u*

| $u$ | $Q_i$ | Rank | $S_i$ | Rank | $R_i$ | Rank |
|---|---|---|---|---|---|---|
| 2517.082 | 0.016147 | 1 | 0.147023 | 2 | 0.094584 | 1 |
| 2957.077 | 0.018547 | 2 | 0.130509 | 1 | 0.11486 | 8 |
| 2855.54 | 0.035569 | 3 | 0.166259 | 6 | 0.095254 | 2 |

**Table 3.** *Suitable solution*

| $u$ | $Q_i$ | Rank | $S_i$ | Rank | $R_i$ | Rank |
|---|---|---|---|---|---|---|
| 2517.082 | 0.016147 | 1 | 0.147023 | 2 | 0.094584 | 1 |

According to the POT requirement, in order to have enough available data, the minimum value of 2517.082 of the compromise solutions is finally chosen as the suitable threshold.

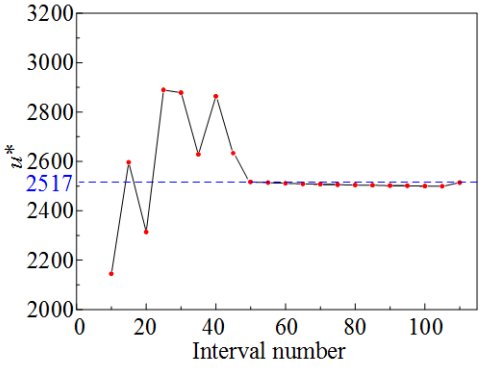


**Fig. 4.** *Compromise solutions in different intervals*

The interval number $m$ above is a fixed value 50. If the value of $m$ changed, the final result may be influenced. Now set the interval number $m = 10, 15, \ldots, 105, 110$. Compromise solutions of each interval are obtained at different intervals. Furthermore, the smallest value of each solution is connected with a line. The results are shown in Fig. 4. When the number of intervals is smaller than 50, the curve of minimal solution values fluctuates fiercely. And the result $u^*$ will near to the value 2517 when $m$ is bigger than 50.

### 2.2 Simulation Study

In this section, the performance of the MCDM method is investigated using simulated data. Firstly, a group of data with a known threshold is used to verify the feasibility of this method. After that, the process is repeated 500 times to verify the effectiveness statistically. The tail part of the mixture distribution is made up of GPD, and the threshold is 3.2816. The histogram of 500 simulated data groups is shown in Fig. 5, and the PDF (the solid line) is also shown together with the threshold $u^*$=3.2816 (the dotted line).

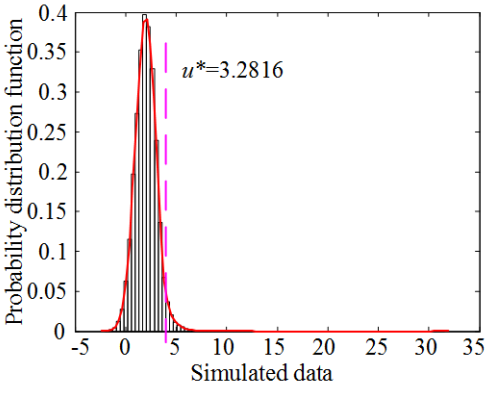


**Fig. 5.** *Histogram and PDF of 500 simulated data sets*

For mean deviation in PDF, K-S test and $\chi^2$test, each candidate threshold will obtain a test value under the corresponding test criteria. Firstly, the primary threshold range is divided into 100 sections. With the help of MLE, the test values with changing threshold values under different test criteria are shown in Fig. 6.

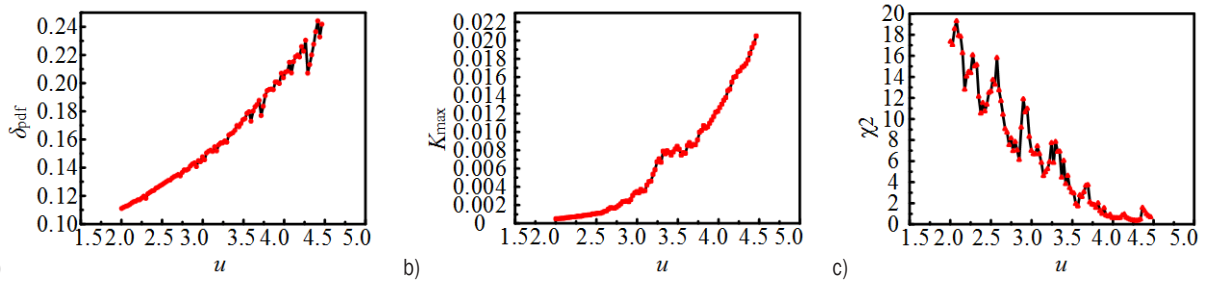


**Fig. 6.** *Test values of different u under different test criteria; a) Mean deviation in PDF; b) K-S test; c) $\chi^2$ test*

A decision matrix of 100×6 is formed. The value of $Q_i$, $S_i$ and $R_i$ ($i=1,2,\ldots,m$) are displayed in Table 4.

**Table 4.** *Rank of $Q_i$, $S_i$ and $R_i$(100×6)*

| $u$ | $Q_i$ | Rank | $S_i$ | Rank | $R_i$ | Rank |
|---|---|---|---|---|---|---|
| 3.14577 | 0.027952 | 1 | 0.21751 | 4 | 0.106447 | 1 |
| 2.84749 | 0.049371 | 2 | 0.198777 | 1 | 0.144548 | 6 |
| 3.170626 | 0.054168 | 3 | 0.227194 | 6 | 0.115527 | 2 |
| … | … | … | … | … | … | … |
| 4.438314 | 0.946539 | 99 | 0.514978 | 99 | 0.472797 | 98 |
| 4.46317 | 1 | 100 | 0.533865 | 100 | 0.492306 | 100 |

Here $m=100$, which means $1/(m-1)=1/(100-1)=0.0101$. According to Table 4 and the two conditions (C1, C2), the value of $Q_2-Q_1$ is larger than 0.0101. The candidate threshold $X_1$ =3.14577 is chosen as the compromise solution. Only one value is available, so 3.14577 is the suitable solution, which is about 4 % smaller than 3.2816.

The number of intervals selected above is 100. Set the interval number $m=10,20,\ldots,140,150$. The suitable solution $u^*$ for each interval can be seen in Fig. 7. The suitable solution changes when the interval number increases. When the interval number is no less than 60, the suitable solution is close to the known value of 3.2816.

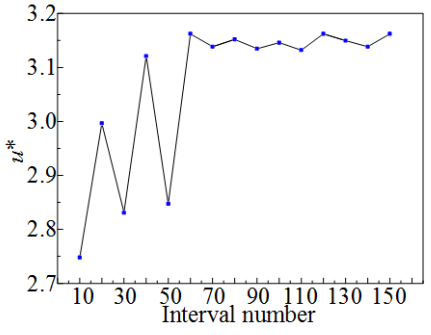


**Fig. 7.** *Suitable solution $u^*$ in different interval*

In order to further verify the feasibility of the method, 500 groups of simulated data are conducted through the calculation process. A histogram of these calculated thresholds is shown in Fig. 8, together with the quantiles (dotted line) of 2.5 % (2.5377) and 97.5 % (3.6501). The mean value of these thresholds is 2.9853.

As seen in Fig. 8, most of the calculated thresholds normally distributed around 3.2816 in the interval of [–22 %, 11 %]. By comparing the mean value of thresholds with the known threshold $u^*$, the difference is less than 10 %. Therefore, it shows that the MCDM method reaches a good fitting accuracy.

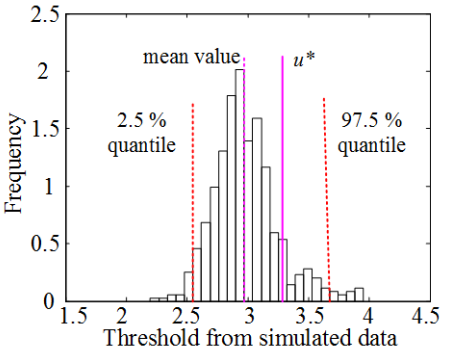


**Fig. 8.** *Histogram of thresholds obtained from 500 simulated data groups*

## 3 RESULTS AND DISCUSSIONS

As shown in Table 3 and Table 5, the suitable thresholds are selected under a certain interval number m and three test criteria. The performance of the proposed method using MCDM is compared with the MRL method and automatic method. The results of the two existing methods are shown as follows.

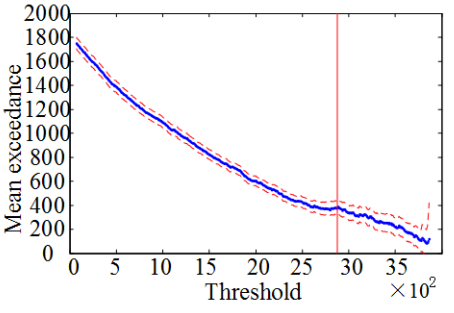


**Fig. 9.** *MRL plot in confidence interval of 95 %*

Fig. 9 is the MRL plot in the confidence interval of 95 %, which plots the mean exceedance as a function of $u$ to decide a proper threshold. The curve on the right side of the vertical line seems to approximate a linear relationship when $u \geq 2800$. The critical value 2800 is chosen as the threshold.

According to [5], $\xi_j$ and $\sigma_j$ are the shape parameter and scale parameter when the threshold is $u_j$, $j=1,\ldots,m$. The initial scope of the threshold is the same as Section 2.1. This scope is divided into 100 equal intervals. The load data of the wheel loader axle shaft is used and the relationship between $\tau_{u_j}-\tau_{u_{j-1}}$ and threshold $u_{j-1}$ is shown in Fig. 10. A new parameter $\tau_{u_j}$ is established, and $\tau_{u_j}=\sigma_{u_j}-\xi_{u_j}u_j$. Exclude unsuitable $u_1,u_2,\ldots,u_{j-1}$ until there is a suitable value $u_j$ to make the distribution of $(\tau_{u_j}-\tau_{u_{j-1}})$ follow the normal distribution. Fig. 11 shows the data

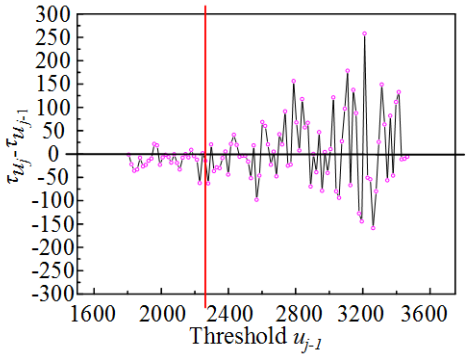


**Fig. 10.** Relationship between $\tau_{u_j} - \tau_{u_{j-1}}$ and $u_{j-1}$

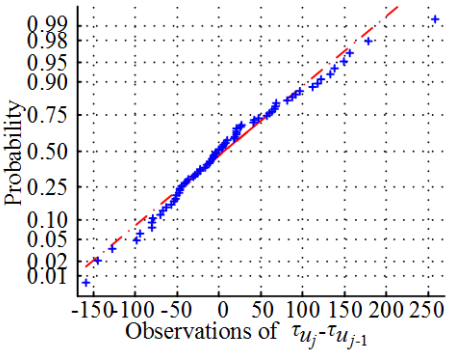


**Fig. 11.** *Normal fitting test of observations* $(\tau_{u_j} - \tau_{u_{j-1}})$

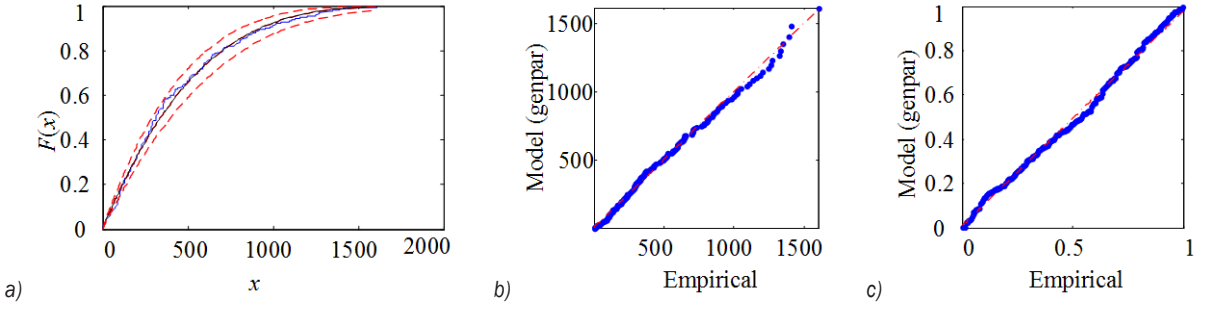


**Fig. 12.** *Threshold u = 2517.082 by the MCDM method, MLE; a) CDF plot; b) P-P plot; c) Q-Q plot*

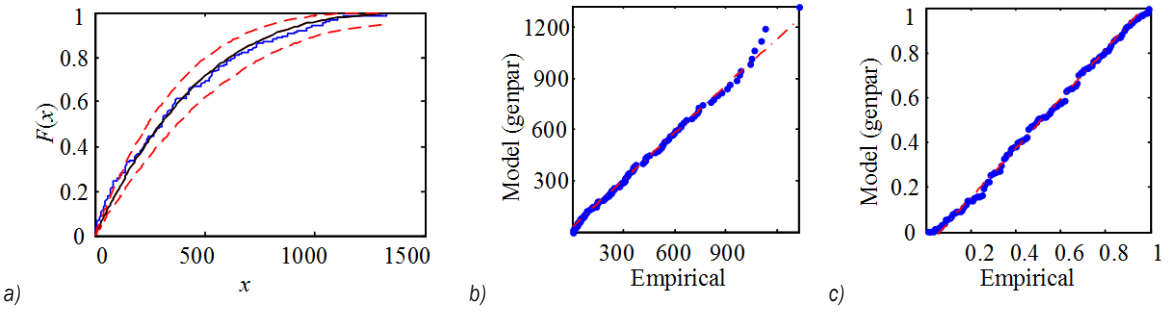


**Fig. 13.** *Threshold u = 2800 by the MRL method, MLE; a) CDF plot; b) P-P plot; c) Q-Q plot*

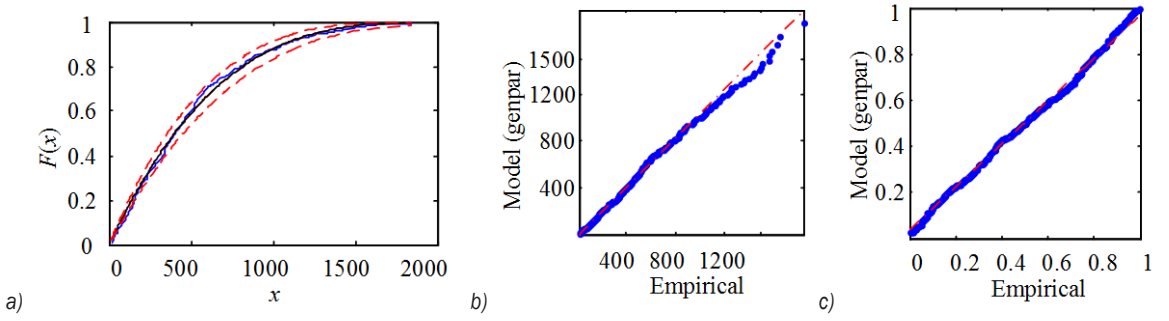


**Fig. 14.** *Threshold u = 2280.161 by the automatic method, MLE; a) CDF plot; b) P-P plot; c) Q-Q plot*

points almost form a nearly straight line which verifies they belong to a normal distribution. Thus, the corresponding value 2280.161 is the suitable threshold.

The graphic method is used as a method of qualitative analysis to show the fitting effect of the selected threshold. Figs. 12 to 14 are the results corresponding to the MCDM method, the MRL, and the automatic method, respectively. Fig. 15 is the return level curves from the above three methods.

Figs. 12 to 14 all show good agreement, since the CDF of the exceedances are located within the confidence interval (the dotted lines) in Figs. 12a, 13a and 14a and most of the data points are distributed in a straight line in the P-P and Q-Q plots. As seen from these figures, all of the results obtained by the three methods show good fitting effects except a few small differences, which could be seen clearly in graphics.

Fig. 15 is the return level curves from the three methods, which shows the extreme load value (return value) with the corresponding load cycles (return period). The return values obtained via the MCDM and the automatic method are almost the same. The difference value between the MRL curve and the other two curves is firstly decreasing and then starts increasing after a certain point as the return period increases. Details between the three curves can be seen in the local enlarged drawing. Suppose the extreme load value occurs when the return period is 10°. Three extreme load values can be obtained in Table 5. The extreme load obtained by the MRL is more conservative than the other two methods are. While the MCDM method is a little more conservative than the automatic method, the difference value is only 36.7.

Numerical test criteria are employed, and the results are shown in Table 5. For the same load data set, the number of exceedance is determined by the threshold value. The value of the MCDM method is 2517.082, which is between 2280.161 and 2800. As seen in Table 5, $a_i$, $b_i$, $c_i$ are the test values under the criteria of mean deviation in PDF, K-S test, and $\chi^2$ test, respectively. The 'min' means the corresponding minimum value of them. Seen from these numbers, every threshold selection method shows its advantage in a certain criterion. When comparing the three test values under mean deviation in PDF, the test value obtained by MRL method is the minimum. The three values are close to each other, but the MCDM method is better than the automatic method from the deviation of test values $a_i/a_{\min}$ and $(a_i/a_{\min})/a_{\min}$. While little difference has appeared under the K-S test, the difference between the minimum (0.0029) and the maximum value (0.0047) of the criterion is an astonishing 158.6 %, which is a factor of 2.59. The difference between the 0.0047 (by MCDM) and the minimum is about 62.1 %, a factor of 1.62, which shows the effect of MCDM method is little poorer than the automatic method under the criterion of K-S. When the test criterion is $\chi^2$ test, it is clear to see the value obtained from the MCDM is the smallest. The factors have also been analysed. The difference between the minimum (4.8446) and the maximum value (10.3993) of the criterion is about 114.65 %, which is a factor of 2.15. And the difference between the middle place value (8.1110) and the minimum (4.8446) is 67.4 % with a factor of 1.67.

It is a new trial to take account of the fitting effect into the process of threshold selection. In general, the MCDM method shows a better performance than the graphic method does. The results of comparisons

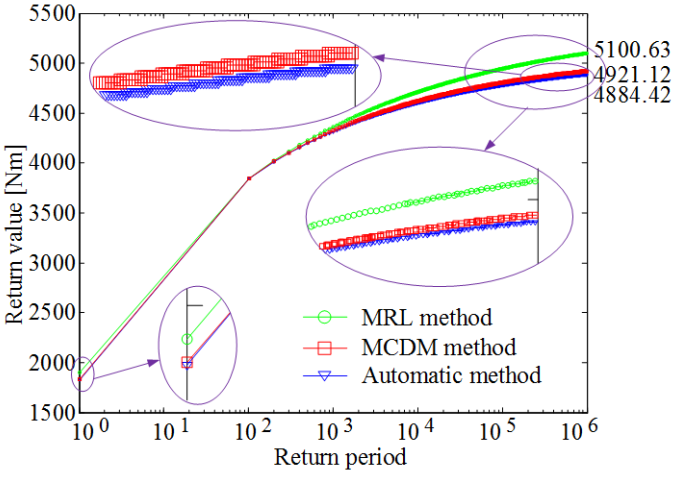


**Fig. 15.** *Return level curves from the MRL, the MCDM and the automatic method*

between the MCDM and the automatic method shows that the performance of the MCDM method is better.

Figs. 6 and 10 further illustrate the influence on the result when the interval number changes. It shows that more intervals will be helpful in obtaining a more precise result. In addition, only three test criteria, mean deviation in PDF, K-S test and $\chi^2$ test, are applied this proposed method. Presently there are no general rules that can be obeyed in selecting the major criteria in final decision-making. Therefore, some personal preference or even prejudice may exist in this process. Further research should be focused on the number and kinds of criteria to build a more realistic POT model.

**Table 5.** *Comparison results of the three methods*

| | MRL | MCDM | Automatic method |
|---|---|---|---|
| Threshold value | 2800 | 2517.082 | 2280.161 |
| Number of exceedance | 125 | 224 | 327 |
| Extreme load | 5100.63 | 4921.12 | 4884.42 |
| Mean deviation in PDF ($a_i$) | 0.0659 | 0.0660 | 0.0661 |
| $a_i/a_{\min}$ | / | 0.152 % | 0. 3 % |
| $(a_i/a_{\min})/a_{\min}$ | / | 1.0015 | 1.003 |
| K-S ($b_i$) | 0.0075 | 0.0047 | 0.0029 |
| $b_i/b_{\min}$ | 158.6 % | 62.1 % | / |
| $(b_i/b_{\min})/b_{\min}$ | 2.59 | 1.62 | / |
| $\chi^2$ ($c_i$) | 10.3993 | 4.8446 | 8.1110 |
| $c_i/c_{\min}$ | 114.65 % | / | 67.4 % |
| $(c_i/c_{\min})/c_{\min}$ | 2.15 | / | 1.67 |

## 4 CONCLUSIONS

The determination of threshold is a key point in establishing the POT model for extreme load extrapolation. At present, some methods are used to determine the threshold. The test criteria are used to verify the fitting accuracy of the distribution when the threshold is determined. Each method may perform well under certain criteria and may be assumed to be the best method. Therefore, it is a problem to select a suitable threshold, when several conflicting test criteria are considered together.

To solve this problem, a new method based on MCDM is proposed in this paper. It is a new trial using multiple criteria in threshold selection. The weight values are obtained using the entropy method. The MCDM integrated the test criteria into comprehensive indicators. According to the result of the compromise solutions, the POT requirement is used to determine the suitable threshold value. The actual load time history and simulated data analysis proved that the MCDM method can create a relatively accurate POT model with a suitable threshold. More intervals lead the results closer to the true threshold value. Finally, the proposed method is compared with two existing methods to show the superiority of the MCDM method. Furthermore, the MCDM method is considered to be a better method to select a proper threshold value. Moreover, the method can be computerized. Each step of the method can be easily modified. For example, test criteria can be added or reduced and the entropy method can also be replaced.

## 5 ACKNOWLEDGMENT

This work was supported by the National Natural Science Foundation of China (No. 51375202, No. 51265020) and the Graduate Innovation Fund (No. 2016074). Project 2016074 was supported by the Graduate Innovation Fund of Jilin University.

## 6 REFERENCES

[1] Moreno, B., Zapatero, J., Domínguez, J. (2003). An experimental analysis of fatigue crack growth under random loading. *International Journal of Fatigue*, vol. 25, no. 7, p. 597-608, **DOI:10.1016/S0142-1123(03)00018-5**.

[2] Wang, J., Zhang, J., Liang, Y., Yang. Y. (2012). A cyclic simulation approach for the generation of the non-stationary load histories of engineering vehicles. *Journal of Mechanical Science and Technology*, vol. 26, no. 5, p. 1547-1554, **DOI:10.1007/s12206-012-0315-9**.

[3] Braccesi, C., Cianetti, F., Lori, G., Pioli, D. (2014). Evaluation of mechanical component fatigue behavior under random loads: Indirect frequency domain method. *International Journal of Fatigue*, vol. 61, p. 141-150, **DOI:10.1016/j.ijfatigue.2013.11.017**.

[4] Hu, W., Han, I., Park, S.-C., Choi, D.-H. (2012). Multi-objective structural optimization of a HAWT composite blade based on ultimate limit state analysis. *Journal of Mechanical Science and Technology*, vol. 26, no. 1, p. 129-135, **DOI:10.1007/s12206-011-1018-3**.

[5] Thompson, P., Cai, Y., Reeve, D., Stander, J. (2009). Automated threshold selection methods for extreme wave analysis. *Coastal Engineering*, vol. 56, no. 10. p. 1013-1021, **DOI:10.1016/j.coastaleng.2009.06.003**.

[6] Wang, J., Chen, H., Li, Y., Wu, Y., Zhang, Y. (2016). A review of the extrapolation method in load spectrum compiling. *Strojniški vestnik - Journal of Mechanical Engineering*, vol. 62, no. 1, p. 60-75, **DOI:10.5545/sv-jme.2015.2905**.

[7] Bae, H.-R., Ando, H., Nam, S., Kim, S., Ha, C. (2015). Fatigue design load identification using engineering data analytics. *Journal of Mechanical Design*, vol. 137, no. 1, p. 011001, **DOI:10.1115/1.4027849**.

[8] Xiang, C.L. (2007). *Dynamics of Armored Vehicle Transmission System*. National defense industry press, Beijing.

[9] Johannesson, P., Thomas, J.-J. (2001). Extrapolation of rainflow matrices. *Extremes*, vol. 4, no. 3, p. 241-262, **DOI:10.1023/A:1015277305308**.

[10] Johannesson, P. (2006). Extrapolation of load histories and spectra. *Fatigue & Fracture of Engineering Materials & Structures*, vol. 29, no. 3, p. 209-217, **DOI:10.1111/j.1460-2695.2006.00982.x**.

[11] Marty, C., Blanchet, J. (2012). Long-term changes in annual maximum snow depth and snowfall in Switzerland based on extreme value statistics. *Climatic Change*, vol. 111, no. 3, p. 705-721, **DOI:10.1007/s10584-011-0159-9**.

[12] Pickands III, J. (1975). Statistical inference using extreme order statistics. *The Annals of Statistics*, vol. 3, no. 1, p. 119-131, **DOI:10.1214/aos/1176343003**.

[13] Harris, R.I. (1999). Improvements to the 'Method of independent storms'. *Journal of Wind Engineering and Industrial Aerodynamics*, vol. 80, no. 1-2, p. 1-30, **DOI:10.1016/S0167-6105(98)00123-8**.

[14] Scarrott, C., MacDonald, A. (2012). A review of extreme value threshold estimation and uncertainty quantification. REVSTAT – Statistical Journal, vol. 10, no. 1, p. 33-60.

[15] Beirlant, J., Goegebeur, Y., Segers, J., Teugels, J., De Waal, D., Ferro, C. (2006). *Statistics of Extremes: Theory and Applications*, John Wiley & Sons, Hoboken.

[16] Drees, H., Resnick, S., de Haan, D. (2000). How to make a Hill plot. *The Annals of Statistics*, vol. 28, no. 1, p. 254-274, **DOI:10.1214/aos/1016120372**.

[17] Beirlant, J., Dierckx, G., Goegebeur, Y., Matthys, G. (1999). Tail index estimation and an exponential regression model. *Extremes*, vol. 2, no. 2, p. 177-200, **DOI:10.1023/A:1009975020370**.

[18] Ferreira, A., de Haan, L., Peng, L. (2003). On optimising the estimation of high quantiles of a probability distribution. *Statistics*, vol. 37, no. 5, p. 401-434, **DOI:10.1080/0233188021000055345**.

[19] Mazas, F., Hamm, L. (2011). A multi-distribution approach to POT methods for determining extreme wave heights. *Coastal Engineering*, vol. 58, no. 5, p. 385-394, **DOI:10.1016/j.coastaleng.2010.12.003**.

[20] Wang, J., Wang, N., Wang, Z., Zhang, Y., Liu, L. (2012). Determination of the minimum sample size for the transmission load of a wheel loader based on multi-criteria decision-making technology. *Journal of Terramechanics*, vol. 49, no. 3-4, p. 147-160, **DOI:10.1016/j.jterra.2012.02.001**.

[21] Wang, J., Liu, Y., Zeng, X., Zhou, Z. Wang, N., Shen, W. (2013). Selection method for Kernel function in nonparametric extrapolation based on multicriteria decision-making technology. *Mathematical Problems in Engineering*, vol. 2013, art. ID. 391273, **DOI:10.1155/2013/391273**.

[22] Opricovic, S., Tzeng, G.-H. (2004). Compromise solution by MCDM methods: A comparative analysis of VIKOR and TOPSIS. *European Journal of Operational Research*, vol. 156, no. 2, p. 445-455, **DOI:10.1016/S0377-2217(03)00020-1**.

[23] Opricovic, S., and Tzeng, G. H. (2007). Extended VIKOR method in comparison with outranking methods. *European Journal of Operational Research*, vol. 178, no. 2, p. 514-529, **DOI:10.1016/S0377-2217(03)00020-1**.

[24] Yazdani, M., Payam, A.F. (2015). A comparative study on material selection of microelectromechanical systems electrostatic actuators using Ashby, VIKOR and TOPSIS. *Materials & Design*, vol. 65, p. 328-334, **DOI:10.1016/j.matdes.2014.09.004**.

[25] Wang, J., Wang, Z., Yang, C., Wang, N., Yu, X., (2012). Optimization of the number of components in the mixed model using multi-criteria decision-making. *Applied Mathematical Modelling*, vol. 36, no. 9, p. 4227-4240, **DOI:10.1016/j.apm.2011.11.053**.

[26] Wang, J., Hu, J., Wang, N., Yao, M., Wang, Z. (2011). Multi-criteria decision-making method-based approach to determine a proper level for extrapolation of Rainflow matrix. *Proceedings of the Institution of Mechanical Engineers, Part C: Journal of Mechanical Engineering Science,* vol. 226, no. 5, p. 1148-1161, **DOI:10.1177/0954406211420212**.

# Vsebina

**Strojniški vestnik - Journal of Mechanical Engineering**
letnik 63, (2017), številka 3
Ljubljana, marec 2017
ISSN 0039-2480

Izhaja mesečno

**Razširjeni povzetki** (extended abstracts)

Strojniški vestnik - Journal of Mechanical Engineering 63(2017)3, SI 23

Prejeto v recenzijo: 2016-08-01
Prejeto popravljeno: 2016-10-25
Odobreno za objavo: 2016-12-21

# Razvoj algoritma za prepoznavanje geometrije za hibridno izdelavo – tehnologijo odvzemanja in dodajanja materiala

David Homar* – Franci Pušavec
Univerza v Ljubljani, Fakulteta za strojništvo, Slovenija

V članku je predstavljen razvit algoritem, ki je namenjen prepoznavi geometrije CAD izdelka, za izdelavo po postopku hibridne izdelave. Hibridna izdelava v našem primeru pomeni združevanje tehnologij odvzemanja materiala in dodajanja materiala po plasteh, gre za postopka odrezovanja in selektivnega laserskega pretaljevanja kovinskih prahov. Pri tem se izkoristi prednosti posamezne tehnologije in s tem eliminira slabosti. En del izdelka se izdela s postopkom odrezovanja, drugi del pa se doda na ta prvi del s postopkom selektivnega laserskega sintranja.

Razvit je bil algoritem OMOS, ki prepozna geometrijo CAD modela predvidenega izdelka in na podlagi te geometrije določi, kateri del se bo izdeloval s katero tehnologijo. S tehnologijo dodajanja materiala po plasteh je možno narediti izdelke zelo kompleksnih oblik, vendar ta tehnologija spada med dražje. Med tem ko tehnologije odrezovanja ne dopuščajo izdelave izdelkov, ki imajo zelo kompleksne geometrijske oblike, saj takšne oblike preprečujejo dostop rezalnemu orodju do površine, katera mora biti obdelana. Je pa ta tehnologija bistveno cenejša od sodobne tehnologije dodajanja materiala. Zato je bila osnova za algoritem OMOS vzeta predpostavka, da se čim večji delež izdelka naredi s tehnologijo odrezovanja, kjer je to le mogoče potem pa se na ta del dogradi še preostali del izdelka s tehnologijo dodajanja materiala.

Algoritem analizira geometrijo CAD modela na osnovi vektorjev, ki gredo skozi CAD model predvidenega izdelka. Na podlagi presečišč se definira zmožnost izdelave izdelka z odrezovanjem. Algoritem OMOS je bil implementiran v komercialni CAD program SolidWorks.

Nato je sledila uporaba in verifikacija algoritma in progama OMOS na industrijskem primeru in sicer na CAD modelu orodnega vložka za brizganje polimernih ram tub. Orodni vložek je imel skonstruirane konformne hladilne kanale za katere je značilno, da so popolnoma prilagojeni površini orodja in so zato zelo kompleksnih oblik in neizvedljivi za izdelavo s tehnologijo odrezovanja. Analiza CAD modela z algoritmom OMOS je definirala, da je spodnji del orodnega vložka, kjer so hladilni kanali še ravni, možno izdelati s tehnologijo odrezovanja, zato je program OMOS izbral to tehnologijo za izdelavo spodnjega dela. Zgornji del pa je bil predviden za izdelavo s tehnologijami dodajanja materiala po plasteh. Nato je bil orodni vložek tudi izdelan po postopku hibridne izdelave.

Verifikacija algoritma OMOS je bila izvedena tudi z analizo proizvodnega časa in stroška izdelave orodnega vložka izdelanega po postopku hibridne izdelave in tudi izdelanega izključno s postopkom dodajanja materiala po plasteh. Analiza je pokazala, da se za izdelavo orodnega vložka po postopku hibridne izdelave porabi za približno 50 % manj časa, kot pri izdelavi izključno s tehnologijo dodajanja materiala po plasteh. In tudi pri stroških izdelave je podobno. Pri hibridni izdelavi so bili stroški za skoraj 50 % manjši, kot pri izdelavi izključno z dodajanjem materiala po plasteh.

Rezultati raziskovalnega dela kažejo na potrebo po združevanju sodobnih tehnologij dodajanja materiala po plasteh in konvencionalnih tehnologij odrezovanja, kar zagotovi izboljšano kakovost, zmanjšanje stroškov, kot tudi zmožnost za izdelavo geometrijsko zelo zahtevnih izdelkov in s tem izboljšanje serijske proizvodnje ter kakovosti končnega izdelka.

**Ključne besede: hibridna izdelava, tehnologije dodajanja materiala po plasteh, tehnologije odvzemanja materiala, odrezovanje, konformni hladilni kanali**

*Naslov avtorja za dopisovanje: Univerza v Ljubljani, Fakulteta za strojništvo, Aškerčeva 6, 1000 Ljubljana, Slovenija, david.homar@fs.uni-lj.si

Strojniški vestnik - Journal of Mechanical Engineering 63(2017)3, SI 24

Prejeto v recenzijo: 2016-07-06
Prejeto popravljeno: 2017-01-05
Odobreno za objavo: 2017-01-31

# Dinamični model in analiza nelinearnih vibracijskih lastnosti zobniškega gonila z valovito razdelno ploskvijo

Zhiqin Cai – Chao Lin*

[1] Državni laboratorij za mehanske prenose, Univerza v Chongqingu, Chongqing, Kitajska

Zobniki z valovito razdelno ploskvijo so nova vrsta zobnikov z lastnostmi, ki so značilne za nevaljaste zobnike, zobnike s poševnim ozobjem in krožnične zobnike, njihov razvoj pa gre v smeri visokih hitrosti in velikih obremenitev. Dinamične lastnosti zobnikov z valovito razdelno ploskvijo neposredno vplivajo na nemoteno in učinkovito delovanje opreme, zato ti zobniki vse bolj pridobivajo na pomenu. Raziskave nelinearnih vibracijskih lastnosti običajnih zobnikov se osredotočajo predvsem na vibracije, udarce in hrup, analitične raziskave pa se naslanjajo na metodo končnih elementov. Lagrangeova enačba s posplošenimi koordinatami v MKE za rotacijski sistem z ekscentričnimi masami vključuje samo kinetično in potencialno energijo sistema, proces simulacije pa je kompleksen.

Da bi se izognili pomanjkljivostim takšnega načina modeliranja, je predlagana nova metoda, ki združuje Lagrangeovo enačbo in grafe povezav. Novi proces modeliranja je ustreznejši in proces reševanja je učinkovitejši. Predstavljen je posplošen nelinearni dinamični model na podlagi Lagrangeove metode z grafi povezav za značilen ekscentričen rotacijski sistem zobnika z valovito razdelno ploskvijo. V model so vključeni osnovni parametri, kot so frekvenca ubiranja, ekscentričnost $k$ in red nevaljastega zobnika $n_1$. S simulacijskim modelom so bile analizirane vibracijske lastnosti zobnika. Vibracijski odziv je kompleksnejši kot pri krožničnem zobniku.

(1) Glavni dejavnik, ki vpliva nanj, je zunanje vzbujanje zaradi vrednosti $rb_1$ in $R$, ki sta odvisni od ekscentričnosti $k$ in reda $n_1$ nevaljastega zobnika. Dinamične lastnosti sistema je mogoče izboljšati z zmanjšanjem ekscentričnosti $k$ in s povečanjem reda $n_1$.

(2) Na vibracijski odziv zobnika vpliva tudi frekvenca ubiranja. Zaradi vpliva zunanjega vzbujanja, ki ojačuje vibracije, je omejena frekvenca ubiranja novega zobnika manjša kot pri krožničnem zobniku. Zobnik zato ni primeren za prenosnike, ki delujejo pri visokih hitrostih.

(3) Podan je predlog eksperimenta za validacijo numeričnega modela. Rezultati eksperimentov se dobro ujemajo s teoretično analizo modelov in sledi sklep, da je model primeren za učinkovito simulacijo vibracijskega odziva zobnikov.

V članku je predstavljen nelinearen dinamični model na osnovi Lagrangeove enačbe in grafa povezav. Metoda je primerna za dinamično analizo zobnikov z valovito razdelno ploskvijo in krožničnih zobnikov. Glavna dejavnika, ki vplivata na vibracijski odziv zobnika, sta $rb_1$ in $R$, njegove dinamične lastnosti pa je mogoče izboljšati z zmanjšanjem ekscentričnosti $k$ in s povečanjem reda $n_1$. Zaradi vpliva zunanjega vzbujanja, ki ojačuje vibracije, je omejena frekvenca ubiranja novega zobnika manjša kot pri krožničnem zobniku. Zobnik zato ni primeren za prenosnike, ki delujejo pri visokih hitrostih.

**Ključne besede: zobnik z valovito razdelno ploskvijo, vibracijski odziv, omejena hitrost, Lagrangeova metoda z grafi povezav, časovno odvisne lastnosti**



*Naslov avtorja za dopisovanje: Državni laboratorij za mehanske prenose, Univerza v Chongqingu, Chongqing, Kitajska linchao@cqu.edu.cn

Strojniški vestnik - Journal of Mechanical Engineering 63(2017)3, SI 25

Prejeto v recenzijo: 2016-08-19
Prejeto popravljeno: 2017-01-18
Odobreno za objavo: 2017-01-31

# Izboljšanje učinkovitosti kmetijskih vitelnih strojev

Martin Kodrič[1] – Jože Flašker[2] – Stanislav Pehan[2]
[1] Nuklearna elektrarna Krško, Slovenija
[2] Univerza v Mariboru, Fakulteta za strojništvo, Slovenija

Namen predstavljenega dela je najti in ovrednotiti možnosti za zmanjšanja porabe goriva in skrajšanje časa obdelave zelo strmih kmetijskih površin, ki se obdelujejo z vitelnimi stroji.

Nasad na strmem terenu je razporejen v vrstah, ki so orientirane po strmini navzgor. Nasad se obdeluje z delovnimi priključki, ki so nameščeni na vozičku. Voziček je opremljen z motorjem, ki poganja zgolj priključke. Premikanje vozička navzgor in spuščanje ob vrstah nasada navzdol se izvaja z vrvjo vitla, ki je nameščen na vrhu terena in ga poganja drug motor. Pri tej tehnologiji obdelave se pojavlja več problemov. Sistem ne omogoča izkoriščanja potencialne energije, ki se neprestano spreminja zaradi pomikanja vozička gor in dol. Posledica je velika poraba goriva, ki je lahko celo do dvakrat večja kot pri kmetijskih traktorjih, ki delajo na ravnem. Voziček, ki je lahko opremljen le z enim priključkom, se mora dvakrat pomikati po isti poti, kar podvaja čas obdelave. Vlečenje vrvi poškoduje rušo.

Razvit je bil hidravlični stroj, ki ima motor in transmisiji za samostojno premikanje in pogon priključkov. Vitel je nameščen na stroju, vrv pa je sidrana na vrhu terena. Motor na stroju je dimenzioniran tako, da zagotavlja le nujno potrebno energijo. To pomeni, da motor zadošča za premikanje navzgor, brez aktivnih delovnih priključkov. Med spuščanjem stroja pa delata dva delovna priključka. Preko hidravlične transmisije ju primarno poganja potencialna energija. Če pa to ne zadošča, ju poganja še motor z notranjim zgorevanjem.

Za prikaz učinkovitosti nove zasnove hidravličnega vitelnega stroja so narejene primerjalne tabele z zbranimi podatki rabe energije, porabljenega goriva, nastale emisije $CO_2$ in časa obdelave na letnem nivoju.

Za opisovanje uporov pri vožnji stroja so uporabljeni klasični analitični modeli iz področja vozil. Podatki za primerjavo učinkovitosti kmetijskih strojev so v tabelah spočetka podani za enakomerne strmine, v zadnjih tabelah pa so narejeni izračuni za realne konfiguracije kmetijskega terena. Pri tem je predpostavljeno, da je en hektar kmetijskega terena sestavljen iz petdesetih linij nasada, dolgih po 100 metrov, ki so med seboj oddaljene 2 metra. Nagib terena je teoretično konstanten po 10 metrskih segmentih. Postopek izračunavanja za realno konfiguracijo je avtomatiziran z namensko programsko opremo. Za lažjo primerjavo je upoštevano, da so lastnosti priključkov za voziček in hidravlični vitelni stroj povsem enake.

Za obdelovanje strmih kmetijskih terenov z vitelnimi stroji je predlagana hidravlična transmisija v kombinaciji z malim motorjem z notranjim zgorevanjem tisto, kar omogoča bistven dvig izkoristka procesa obdelave. V obravnavanih primerih realne kmetijske površine je poraba goriva zmanjšana za 36 %, če za primerjavo vzamemo obdelavo z vozičkom, ki je pripet na pogonski vitel. Čas obdelave na letnem nivoju je skrajšan za 41 %. In končno, ker se vrv ne vleče več po terenu, se izognemo poškodbi ruše.

Narejen in predstavljen je bil konkreten hidravlični stroj za obdelavo kmetijskih površin z nakloni do 100 %. Obravnavana je bila vzorčna realna kmetijska površina. Nekaj osnovnih primerjav glede izkoristka procesa obdelave je narejenih z običajnimi kmetijskimi stroji za obdelavo bolj ali manj ravnih kmetijskih površin, druge primerjave pa zajemajo vitelne vozičke.

Vpeljan je novi pojem, ki omogoča razlikovanje pristopov k obdelavi strmih kmetijskih površin z različnimi stroji. Ta pojem je poimenovan izkoristek procesa obdelave in predstavlja razmerje med koristno uporabljeno in skupno vloženo energijo v obliki kemične energije goriva. Nov hidravlični kmetijski stroj omogoča prihranek energije, torej goriva, in časa.

**Ključne besede: strm teren, obdelava trajnega nasada, hidravlični kmetijski stroj, izkoristek procesa obdelave**

*Naslov avtorja za dopisovanje: Univerza v Mariboru, Fakulteta za strojništvo, Smetanova ulica 17, 2000 Maribor, Slovenija, stanislav.pehan@um.si

Strojniški vestnik - Journal of Mechanical Engineering 63(2017)3, SI 26


Prejeto v recenzijo: 2016-03-01
Prejeto popravljeno: 2016-08-06
Odobreno za objavo: 2016-10-05

# Modeliranje in upravljanje elektronske bobnaste zavore z razpiralom in fiksnim sedlom

Fauzi Ahmad[1,2,*] – Khisbullah Hudha[3] – Saiful Amri Mazlan[1] – Hishamuddin Jamaluddin[4] – Hairi Zamzuri[1] – Zulkiffli Abd Kadir[1,3] – Vimal Rau Aparow[3]

1 Malezijska tehniška univerza, Malezijsko-japonski mednarodni inštitut za tehnologijo, Malezija
2 Tehniška univerza v Maleziji, Fakulteta za strojništvo, Malezija
3 Državna univeza Pertahanan, Tehniška fakulteta, Malezija
4 Južni univerzitetni kolidž, Fakulteta za tehniko in informacijsko tehnologijo, Malezija

Članek predstavlja novo zasnovo elektronske bobnaste zavore z razpiralom (EWB) v izvedbi s fiksnim sedlom (FIXEWB). Podaja tudi matematično izpeljavo modela dinamičnega vedenja zavore FIXEWB in upravljanje sistema s sledenjem momenta.

Motivacija za raziskave in razvoj zavore FIXEWB so bile težave pri obstoječih zasnovah EWB v smislu resnih omejitev pri snovanju, modeliranju in upravljanju zavor. Zavorni sistem EWB uporablja plavajoče sedlo, nerazrešen pa ostaja tudi problem zatikanja razpirala na stiku. Številne študije na tem področju so pripeljale do določenih izboljšav, mnoge med njimi pa so bile namenjene optimizaciji profilnega kota razpirala.

V okviru obsežnih raziskav EWB so bile razvite rešitve za matematično modeliranje in za upravljanje sistemov EWB, rezultati validacije modelov EWB pa kažejo več kot 10-odstotni razkorak med rezultati simulacije in rezultati eksperimentov. To neujemanje je posledica poenostavitev, idealizacije ter uporabljenih tehnik modeliranja zavornega sistema na podlagi metode ocenjevanja fizikalnih parametrov (PPEM). Tehnika PPEM se naslanja na več domnev, ki lahko vplivajo na primernost modela. Da bi se izognili slabostim sistema EWB, je bila razvita zavora FIXEWB z optimiziranim profilnim kotom razpirala. Ta zagotavlja manjšo silo za aktiviranje razpiralnega mehanizma in preprečuje njegovo zatikanje v okolici stika. FIXEWB v mehanizmu je sestavljen iz dveh setov razpiralnih blokov, pogonskega krogličnega vretena, drsnika in elektromotorja. Vrtenje osi elektromotorja se s pomočjo krogličnega vretena pretvarja v linearno gibanje drsnika. Drsnik aktivira razpiralni mehanizem in tangencialni premik zavorne ploščice proti zavornemu disku ter tako ustvarja pritezno silo in zavorni moment pri vrtenju kolesa. Karakterizacija EWB je zelo pomembna, saj je veljavnost modela ključnega pomena za model upravljanja in točno sledenje izhodne sile/momenta EWB.

V študiji je bil uporabljen matematični model za simulacijo dinamičnega vedenja FIXEWB po metodi identifikacije sistema (SIM). Na preizkuševališču je bil pridobljen nabor podatkov za učenje, vključno z vhodnim kotom pogonske osi in vpenjalno silo. Na podlagi teh podatkov je bila razvita prenosna funkcija drugega reda za modeliranje pritezne sile sistema FIXEWB. Za napovedovanje zavornega momenta, ki ga ustvarja FIXEWB, je bil uporabljen standardni izračun navora po tehniki PPEM.

Razviti matematični model je bil validiran z več testi, pri katerih se je spreminjal vhodni kot pogonske gredi po koračni, variabilni koračni in sinusni funkciji. Pri validaciji sta bila opazovana pritezna sila in zavorni moment, ki ga ustvarja zavorni sistem. Napovedani odziv po matematičnem modelu je bil primerjan z odzivi, izmerjenimi na preizkuševališču EWB. Iz rezultatov je mogoče sklepati, da predlagani matematični model zadovoljivo napoveduje vedenje sistema FIXEWB z odstopanji, manjšimi od 5 %. Točnost in veljavnost predlaganega modela je bila dodatno validirana v zaprtozančnem krmilnem sistemu za sledenje želenega zavornega momenta. Vrednotenje je pokazalo podobno vedenje pri eksperimentih in v simulacijah, s srednjo absolutno napako v višini približno 3 %. S tem je tudi dokazana primernost predlaganega matematičnega modela.

Prispevek predstavljene študije je v novi zasnovi elektronske zavore z razpiralom in fiksnim sedlom ter v razvoju modela FIXEWB po tehniki SIM.

**Ključne besede: elektronska bobnasta zavora z razpiralom, elektronska bobnasta zavora z razpiralom in fiksnim sedlom, modeliranje in validacija, tehnika identifikacije sistema, metoda ocenjevanja fizikalnih parametrov, optimizacija kota razpirala**



*Naslov avtorja za dopisovanje: Malezijska tehniška univerza, Malezijsko-japonski mednarodni inštitut za tehnologijo, 54100 Jalan Semarak Kuala Lumpur, Malezija, fauzi.ahmad@utem.edu.my

Strojniški vestnik - Journal of Mechanical Engineering 63(2017)3, SI 27

Prejeto v recenzijo: 2016-10-04
Prejeto popravljeno: 2016-12-14
Odobreno za objavo: 2017-01-17

# Aerodinamična stabilnost vozila v močnem spremenljivem vetru

Aleksander Grm* – Milan Batista
Univerza v Ljubljani, Fakulteta za pomorstvo in promet, Slovenija

Pričujoče delo obravnava aerodinamično stabilnost vozila v močno spremenljivem vetru. Močno spremenljiv veter predstavlja veliko nevarnost, ker lahko povzroči prevrnitev, zdrs ali zasuk vozila med vožnjo. Glede na različne vetrovne razmere, se pojavi vprašanje, ali lahko ocenimo, pri kateri vrednosti vetra (hitrost in smer) postane vožnja nevarna.

Ocena kritične hitrosti in smeri vetra za posamezno vozilo temelji na izračunu aerodinamičnih koeficientov vozila. Aerodinamični koeficienti vozila predstavljajo prispevke posameznih sil v različnih pravokotnih smereh na vozilo in navorov okoli koordinatnih osi napetih na sistem vozila. V primeru postavitve koordinatnega sistema, kjer je $x$ os postavljena v smeri vozila, $y$ os postavljena pravokotno na vzdolžnico vozila in $z$ os postavljena pravokotno na $xy$ ravnino, je koeficient sile upora ($C_D$ - drag) postavljen v smeri $x$ osi, koeficient stranske sile ($C_S$ - side) postavljen v smeri $y$ osi, koeficient sile dviga ($C_L$ - lift) postavljen v smeri $z$ osi. Koeficienti navorov si pa sledijo, okoli osi $x$ ($C_R$ - roll), okoli osi $y$ ($C_P$ - pitch) in okoli osi $z$ ($C_Y$ - yaw). S pomočjo koeficientov, ki so odvisni od smeri vetra, lahko določimo zunanje sile in navore na vozilo za različne smeri in hitrosti vetra.

Aerodinamične koeficiente smo določili s pomočjo numerične simulacije kapljevin, kjer smo izdelali 3D model, za katerega so bile znane eksperimentalne meritve. Naredili smo podrobno analizo vpliva konstrukcije mreže in SST-omega turbulentnega modela v izračunih aerodinamičnih koeficientov. Analiza je potrdila izbor najboljšega kandidata, ki je bil kasneje uporabljen za vse izračune. Izračuni so bili narejeni za različne vpadne kote vetra na vozilo, pri čemer smo vozilo vrteli v navideznem vetrovniku. Primerjava rezultatov simulacije in meritev iz literature so pokazale dobro ujemanje, kar je zagotovilo za uspešno uporabo v aerodinamični stabilnostni analizi.

Aerodinamični koeficienti, odvisni od smeri vetra, tako predstavljajo osnovo za izračun mejnih stabilnostnih vrednosti vetra, pri katerih je vožnja še vedno varna. Določili smo mejne vrednosti hitrosti vetra za prevrnitev, zdrs in zasuk vozila. Najvišje vrednosti se vedno nahajajo pri navidezni smeri vetra, ki je pravokotno na vozilo. V odvisnosti od mase, koeficienta trenja in dimenzij vozila se enako nato spreminja še vrednost mejne hitrosti, pri kateri določen aerodinamičen stabilnostni kriterij popusti in vozilo tako postane nestabilno.

V pričujočem delu predstavljajo nekateri koeficienti težavo pri določitvi njihove odvisnosti po kotu navidezne smeri vetra. Razlog je v njihovih velikih spremembah, katerim botrujejo izjemno nestabilni turbulentni pojavi v določenih smereh. Zelo pomembno bi bilo narediti podrobno analizo teh kritičnih koeficientov v postopku simulacij.

Prikazali smo enovit tehničen postopek za določitev aerodinamične stabilnosti vozila z uporabo numeričnih orodij. Dodatni poizkusi v vetrovnih tunelih so izjemno zaželeni, a je njihova izvedba zelo draga in velikokrat je tudi omejena z naborom merskih podatkov.

**Ključne besede: aerodinamična stabilnost/nestabilnost, vetrovna računska mehanika, sile in momenti prekuca, računska mehanika kapljevin, interakcija med strukturo in kapljevinami**

*Naslov avtorja za dopisovanje: Univerza v Ljubljani, Fakulteta za pomorstvo in promet, Pot pomorščakov 4, 6320 Portorož, Slovenija, aleksander.grm@fpp.uni-lj.si

Strojniški vestnik - Journal of Mechanical Engineering 63(2017)3, SI 28

Prejeto v recenzijo: 2016-03-05
Prejeto popravljeno: 2016-12-12
Odobreno za objavo: 2017-01-31

# Določitev praga za ekstrapolacijo izjemnih obremenitev na podlagi tehnologije večkriterijskega odločanja

Jixin Wang – Xinting Zhai* – Cheng Liu – Yingshuang Zhang
Jilin Univerza, Fakulteta za strojništvo, Kitajska

Pri ekstrapolaciji izjemnih obremenitev ima odločilno vlogo vrednost praga. Za izbiro vrednosti praga so na voljo grafične in numerične metode, kot testni kriterij pa se uporabljajo meritve, s katerimi se vrednoti primernost izbranega praga. Posamezne metode so lahko sicer optimalne za določene kriterije, toda za praktične probleme je značilno križanje različnih kriterijev in je težko določiti vrednost praga, ki bi izpolnjevala zahteve vseh kriterijev. Za razrešitev tega problema je predlagana metoda na podlagi tehnologije večkriterijskega odločanja (MCDM), ki upošteva skupen vpliv več kriterijev. Pri tej metodi so kot testni kriteriji uporabljeni povprečno odstopanje funkcije porazdelitve verjetnosti, test Kolmogorov-Smirnov in test hi-kvadrat. Vrednosti uteži za teste so določene po metodi entropije. Predstavljena je metoda VIKOR. Uporabljen je indeks za večkriterijsko razvrščanje na podlagi meritev ujemanja z »idealno« rešitvijo. Najboljša oz. kompromisna rešitev vključuje eno ali več primernih vrednosti ter je določena na podlagi ustreznih kriterijev in uteži. Primeren prag je končno določen s pomočjo zahtevane vrednosti nad pragom (POT).

Opravljena je analiza zgodovine časov obremenitve in simuliranih podatkov za vrednotenje zmogljivosti in uspešnosti predlagane metode. Predstavljena je primerjalna analiza predlagane metode s še dvema pogosto uporabljenima metodama – MRL in samodejno metodo. Za kvalitativno analizo učinka prileganja izbranega praga je uporabljena grafična metoda. Vsi rezultati, pridobljeni po treh metodah, kažejo dobro prileganje, z izjemo nekaj manjših odstopanj, ki so prikazana na slikah. Krivulje nivoja vračanja kažejo, da je izjemna obremenitev, ki je bila določena po metodi MRL, konzervativnejša kot pri ostalih dveh metodah. Predlagana metoda je primerljiva, saj znaša razlika samo 36,7. Glede na kriterij prileganja testa je metoda MCDM boljša od grafične metode. Tudi primerjava med MCDM in samodejno metodo daje prednost metodi MCDM.

Trenutno ni splošnih pravil glede izbire glavnih kriterijev za končno odločanje, zato je ta postopek nujno povezan z osebnimi preferencami ali celo s predsodki. Nadaljnje raziskave bi morale biti osredotočene na število in vrsto kriterijev za izgradnjo bolj realističnega modela POT.

Predlagana metoda lahko da razmeroma točen model POT s primernim pragom, rezultati pa so bližji resnični vrednosti praga zaradi večjega števila intervalov. Metoda, predlagana v tem članku, je bila primerjana z grafom MRL in s samodejno metodo. V primerjavi z metodo MRL je superiorna, nekoliko zmogljivejša pa je tudi od samodejne metode. Predlagana metoda je primernejša za določanje vrednosti pragov, omogoča pa tudi računalniško obdelavo. Vsak korak metode je mogoče enostavno spremeniti, npr. z dodajanjem ali odvzemanjem testnih kriterijev in s spremembo načina določanja uteži.

**Ključne besede: večkriterijsko odločanje (MCDM), prag, ekstrapolacija izjemnih obremenitev, vrednosti nad pragom (POT), metoda entropije, VIKOR**



*Naslov avtorja za dopisovanje: Jilin Univerza, Fakulteta za strojništvo, Changchun, Kitajska, zxt00900@sina.com

Na Fakulteti za strojništvo Univerze v Ljubljani sta obranila svojo doktorsko disertacijo:

- dne *14. februarja 2017* **Marko BEK** z naslovom: »Uporaba viskoelastičnih materialov za zmanjšanje vibracij in hrupa železniških tirov« (mentor: prof. dr. Igor Emri);

Kotalni hrup je glavni vir hrupa in vibracij v železniškem transportu. Polimerni dušilni elementi, ki so trenutno v uporabi za zmanjšanje hrupa železniških tirov, ne izkoriščajo celotnega potenciala viskoelastičnih materialov. V sklopu disertacije so predstavljeni patentirani granulirani dušilni elementi (GDE), ki so sestavljeni iz pletene cevi in napolnjeni z granuliranim polimernim materialom. Njihove lastnosti je mogoče prilagajati oz. spreminjati s hidrostatičnim tlakom, kateremu je granulirani material izpostavljen, kar omogoča poljubno spreminjanje dušilnih lastnosti.

Testiranje koncepta patentiranih GDE, narejenih iz odpadne gume, je pokazalo, da se disipirana energija takšnih elementov pri višjih tlakih poveča do 10 krat, togost pa do 20 krat. Za nadaljnjo izboljšanje dušilnih lastnosti je bila razvita naprava ‚Granular Friction Analyzer' (GFA), ki omogoča preučevanje inherentnega trenja granuliranih materialov, le ti pa so izpostavljeni tlaku in pogojem, pri katerih se bo material začel premikati. Poleg tega smo preučili tudi vpliv tlaka (izražen s položajem mehanskega spektra) in viskoelastičnih materialnih funkcij (izraženih s širino mehanskega spektra) na karakteristike dušilnih elementov. Tlak in viskoelastične materialne funkcije so bile analizirane s pomočjo prenosnosti.

V sklopu disertacije je bilo pokazano, da razvita GFA naprava lahko napove in izmeri vpliv velikosti in porazdelitve velikosti delcev, njihove oblike, itd., na trenje in pretočnost granuliranih materialov, kar je bistveno pri proizvodnji GDE, kakor tudi za ustvarjanje hidrostatičnega tlak znotraj GDE. Ugotovljeno je bilo tudi, da premik mehanskega spektra na logaritemski časovni skali v levo zaradi zmanjšanega tlaka, premakne resonančni vrh do nižjih frekvenc, hkrati pa se prenosnost znatno poveča. Po drugi strani pa, če so materiali izpostavljeni višjemu tlaku, ki premakne spekter na logaritemski časovni skali v desno, se bo resonančni vrh pomaknil k višjim frekvencam, prenosnost pa se bo zmanjševala proti T = 1;

- dne *15. februarja 2017* **mag. Blaž FLORJANIČ** z naslovom: »Model ocene obsega izdelovalnih časov v proizvodnji orodij za injekcijsko brizganje termoplastičnih polimerov« (mentor: prof. dr. Karl Kuzman, somentor: prof. dr. Edvard Govekar);

Obravnavana problematika je ocena obsega izdelovalnih časov v individualni proizvodnji orodij za injekcijsko brizganje termoplastov. Obseg izdelovalnih časov je seštevek vseh strojnih proizvodnih ur (časov obdelav), ki so potrebne za izdelavo orodja. Za postavitev ocenitvenega modela so ključna tri v delu podrobneje predstavljena področja: orodja za injekcijsko brizganje termoplastov, proizvodnja orodij in ocenitvene metode. Za oblikovanje ocene so na razpolago različne metode, pri čemer je delo osredotočeno na oblikovanju podpore ekspertnemu intuitivnemu pristopu z uporabo modela temelječega na nevronskih mrežah. Cilj raziskave je kvantifikacija vhodnih faktorjev (parametrov) za ustrezen popis kompleksnosti geometrije izdelka in modeliranje vpliva kompleksnosti geometrije na obseg izdelovalnih časov. Nevronske mreže služijo za modeliranje povezav med vhodnimi faktorji in obsegom izdelovalnih časov, kar za eksperta predstavlja kompleksnejši induktivni proces. Z raziskavo oblikovani model zagotavlja ocenitvenem procesu povečano natančnost, objektivnost in ponovljivost ob krajšem času za izvedbo postopka. Uporaba takšnega modela predstavlja zanesljiv temelj oceni proizvodnih stroškov.

# Information for Authors

All manuscripts must be in English. Pages should be numbered sequentially. The manuscript should be composed in accordance with the Article Template given above. The maximum length of contributions is 10 pages. Longer contributions will only be accepted if authors provide juastification in a cover letter. For full instructions see the Information for Authors section on the journal's website: http://en.sv-jme.eu .

**SUBMISSION:**

Submission to SV-JME is made with the implicit understanding that neither the manuscript nor the essence of its content has been published previously either in whole or in part and that it is not being considered for publication elsewhere. All the listed authors should have agreed on the content and the corresponding (submitting) author is responsible for having ensured that this agreement has been reached. The acceptance of an article is based entirely on its scientific merit, as judged by peer review. Scientific articles comprising simulations only will not be accepted for publication; simulations must be accompanied by experimental results carried out to confirm or deny the accuracy of the simulation. Every manuscript submitted to the SV-JME undergoes a peer-review process.

The authors are kindly invited to submit the paper through our web site: http://ojs.sv-jme.eu. The Author is able to track the submission through the editorial process - as well as participate in the copyediting and proofreading of submissions accepted for publication - by logging in, and using the username and password provided.

**SUBMISSION CONTENT:**

The typical submission material consists of:

- A **manuscript** (A PDF file, with title, all authors with affiliations, abstract, keywords, highlights, inserted figures and tables and references),
- Supplementary files:
  - a **manuscript** in a WORD file format
  - a **cover letter** (please see instructions for composing the cover letter)
  - a ZIP file containing **figures** in high resolution in one of the graphical formats (please see instructions for preparing the figure files)
  - possible **appendicies** (optional), cover materials, video materials, etc.

Incomplete or improperly prepared submissions will be rejected with explanatory comments provided. In this case we will kindly ask the authors to carefully read the Information for Authors and to resubmit their manuscripts taking into consideration our comments.

**COVER LETTER INSTRUCTIONS:**

Please add a **cover letter** stating the following information about the submitted paper:

1. Paper **title**, list of **authors** and their **affiliations**.
2. **Type of paper**: original scientific paper (1.01), review scientific paper (1.02) or short scientific paper (1.03).
3. A **declaration** that neither the manuscript nor the essence of its content has been published in whole or in part previously and that it is not being considered for publication elsewhere.
4. State the **value of the paper** or its practical, theoretical and scientific implications. What is new in the paper with respect to the state-of-the-art in the published papers? Do not repeat the content of your abstract for this purpose.
5. We kindly ask you to suggest at least two **reviewers** for your paper and give us their names, their full affiliation and contact information, and their scientific research interest. The suggested reviewers should have at least two relevant references (with an impact factor) to the scientific field concerned; they should not be from the same country as the authors and should have no close connection with the authors.

**FORMAT OF THE MANUSCRIPT:**

The manuscript should be composed in accordance with the Article Template. The manuscript should be written in the following format:

- A **Title** that adequately describes the content of the manuscript.
- A list of **Authors** and their **affiliations**.
- An **Abstract** that should not exceed 250 words. The Abstract should state the principal objectives and the scope of the investigation, as well as the methodology employed. It should summarize the results and state the principal conclusions.
- 4 to 6 significant **key words** should follow the abstract to aid indexing.
- 4 to 6 **highlights;** a short collection of bullet points that convey the core findings and provide readers with a quick textual overview of the article. These four to six bullet points should describe the essence of the research (e.g. results or conclusions) and highlight what is distinctive about it.
- An **Introduction** that should provide a review of recent literature and sufficient background information to allow the results of the article to be understood and evaluated.
- A **Methods** section detailing the theoretical or experimental methods used.
- An **Experimental section** that should provide details of the experimental set-up and the methods used to obtain the results.
- A **Results** section that should clearly and concisely present the data, using figures and tables where appropriate.
- A **Discussion** section that should describe the relationships and generalizations shown by the results and discuss the significance of the results, making comparisons with previously published work. (It may be appropriate to combine the Results and Discussion sections into a single section to improve clarity.)
- A **Conclusions** section that should present one or more conclusions drawn from the results and subsequent discussion and should not duplicate the Abstract.
- **Acknowledgement** (optional) of collaboration or preparation assistance may be included. Please note the source of funding for the research.
- **Nomenclature** (optional). Papers with many symbols should have a nomenclature that defines all symbols with units, inserted above the references. If one is used, it must contain all the symbols used in the manuscript and the definitions should not be repeated in the text. In all cases, identify the symbols used if they are not widely recognized in the profession. Define acronyms in the text, not in the nomenclature.
- **References** must be cited consecutively in the text using square brackets [1] and collected together in a reference list at the end of the manuscript.
- **Appendix(-icies)** if any.

**SPECIAL NOTES**

**Units**: The SI system of units for nomenclature, symbols and abbreviations should be followed closely. Symbols for physical quantities in the text should be written in italics (e.g. *v*, *T*, *n*, etc.). Symbols for units that consist of letters should be in plain text (e.g. $ms^{-1}$, K, min, mm, etc.). Please also see: http://physics.nist.gov/cuu/pdf/sp811.pdf .

**Abbreviations** should be spelt out in full on first appearance followed by the abbreviation in parentheses, e.g. variable time geometry (VTG). The meaning of symbols and units belonging to symbols should be explained in each case or cited in a **nomenclature** section at the end of the manuscript before the References.

**Figures** (figures, graphs, illustrations digital images, photographs) must be cited in consecutive numerical order in the text and referred to in both the text and the captions as Fig. 1, Fig. 2, etc. Figures should be prepared without borders and on white grounding and should be sent separately in their original formats. If a figure is composed of several parts, please mark each part with a), b), c), etc. and provide an explanation for each part in Figure caption. The caption should be self-explanatory. Letters and numbers should be readable (Arial or Times New Roman, min 6 pt with equal sizes and fonts in all figures). Graphics (submitted as supplementary files) may be exported in resolution good enough for printing (min. 300 dpi) in any common format, e.g. TIFF, BMP or JPG, PDF and should be named Fig1.jpg, Fig2.tif, etc. However, graphs and line drawings should be prepared as vector images, e.g. CDR, AI. Multi-curve graphs should have individual curves marked with a symbol or otherwise provide distinguishing differences using, for example, different thicknesses or dashing.

**Tables** should carry separate titles and must be numbered in consecutive numerical order in the text and referred to in both the text and the captions as Table 1, Table 2, etc. In addition to the physical quantities, such as *t* (in italics), the units [s] (normal text) should be added in square brackets. Tables should not duplicate data found elsewhere in the manuscript. Tables should be prepared using a table editor and not inserted as a graphic.

**REFERENCES:**

A reference list must be included using the following information as a guide. Only cited text references are to be included. Each reference is to be referred to in the text by a number enclosed in a square bracket (i.e. [3] or [2] to [4] for more references; do not combine more than 3 references, explain each). No reference to the author is necessary.

References must be numbered and ordered according to where they are first mentioned in the paper, not alphabetically. All references must be complete and accurate. Please add DOI code when available. Examples follow.

**Journal Papers:**

Surname 1, Initials, Surname 2, Initials (year). Title. Journal, volume, number, pages, DOI code.

[1] Hackenschmidt, R., Alber-Laukant, B., Rieg, F. (2010). Simulating nonlinear materials under centrifugal forces by using intelligent cross-linked simulations. *Strojniški vestnik - Journal of Mechanical Engineering,* vol. 57, no. 7-8, p. 531-538, DOI:10.5545/sv-jme.2011.013.

Journal titles should not be abbreviated. Note that journal title is set in italics.

**Books:**

Surname 1, Initials, Surname 2, Initials (year). Title. Publisher, place of publication.

[2] Groover, M.P. (2007). *Fundamentals of Modern Manufacturing*. John Wiley & Sons, Hoboken.

Note that the title of the book is italicized.

**Chapters in Books:**

Surname 1, Initials, Surname 2, Initials (year). Chapter title. Editor(s) of book, book title. Publisher, place of publication, pages.

[3] Carbone, G., Ceccarelli, M. (2005). Legged robotic systems. Kordić, V., Lazinica, A., Merdan, M. (Eds.), Cutting Edge Robotics. Pro literatur Verlag, Mammendorf, p. 553-576.

**Proceedings Papers:**

Surname 1, Initials, Surname 2, Initials (year). Paper title. Proceedings title, pages.

[4] Štefanić, N., Martinčević-Mikić, S., Tošanović, N. (2009). Applied lean system in process industry. *MOTSP Conference Proceedings*, p. 422-427.

**Standards:**

Standard-Code (year). Title. Organisation. Place.

[5] ISO/DIS 16000-6.2:2002. *Indoor Air – Part 6: Determination of Volatile Organic Compounds in Indoor and Chamber Air by Active Sampling on TENAX TA Sorbent, Thermal Desorption and Gas Chromatography using MSD/FID.* International Organization for Standardization. Geneva.

**WWW pages:**

Surname, Initials or Company name. Title, from http://address, date of access.

[6] Rockwell Automation. Arena, from *http://www.arenasimulation.com,* accessed on 2009-09-07.

**EXTENDED ABSTRACT:**

When the paper is accepted for publishing, the authors will be requested to send an **extended abstract** (approx. one A4 page or 3500 to 4000 characters). The instruction for composing the extended abstract are published on-line: http://www.sv-jme.eu/information-for-authors/ .

**COPYRIGHT:**

Authors submitting a manuscript do so on the understanding that the work has not been published before, is not being considered for publication elsewhere and has been read and approved by all authors. The submission of the manuscript by the authors means that the authors automatically agree to transfer copyright to SV-JME when the manuscript is accepted for publication. All accepted manuscripts must be accompanied by a Copyright Transfer Agreement, which should be sent to the editor. The work should be original work by the authors and not be published elsewhere in any language without the written consent of the publisher. The proof will be sent to the author showing the final layout of the article. Proof correction must be minimal and executed quickly. Thus it is essential that manuscripts are accurate when submitted. Authors can track the status of their accepted articles on http://en.sv-jme.eu/.

**PUBLICATION FEE:**

Authors will be asked to pay a publication fee for each article prior to the article appearing in the journal. However, this fee only needs to be paid after the article has been accepted for publishing. The fee is 240.00 EUR (for articles with maximum of 6 pages), 300.00 EUR (for articles with maximum of 10 pages), plus 30.00 EUR for each additional page. The additional cost for a color page is 90.00 EUR. These fees do not include tax.

Strojniški vestnik -Journal of Mechanical Engineering
Aškerčeva 6, 1000 Ljubljana, Slovenia,
e-mail: info@sv-jme.eu

9 770039 248001
ISSN 0039-2480

http://www.sv-jme.eu

# Contents

## Papers